



NTNU – Trondheim
Norwegian University of
Science and Technology

Sensorless Start-up and Control of Permanent Magnet Synchronous Motor with Long Tieback

Kristiansen Baricuatro

Master of Science in Electric Power Engineering

Submission date: June 2014

Supervisor: Trond Toftevaag, ELKRAFT

Norwegian University of Science and Technology
Department of Electric Power Engineering

Problem Description

With the increasing demand for oil and gas production, oil and gas companies start to step out into deeper waters with continuously increasing pump ratings. Due to these, start-up of subsea pump motors with long tieback distance and high breakaway torque becomes more and more relevant. Lack of sufficient expertise and right tools for analyses and calculations can easily lead to over dimensioned components; along with its unwanted consequences on component size, weight and cost. Moreover, if the system is under or improperly dimensioned, it will not be possible to start the pump motor in certain situations.

The master thesis is a further investigation of the start-up procedure of a permanent magnet synchronous motor operated by variable frequency drive without position feedback via a long cable and transformers; as proposed in the specialization project, fall of 2013. The challenge is how to avoid large saturation in the transformers and motor while achieving the maximum possible starting torque with high cable resistance. The converter is to operate without a rotor position feedback.

Three scalar Volts per Hertz control schemes without position feedback were defined and established in Simulink for motor start-up simulation purposes in the project work. The master thesis should investigate possible optimization of these control schemes.

A simple study case comprising of a permanent magnet synchronous motor operated by a variable frequency drive without position feedback via a long cable were defined, simulated and analysed via Simulink in the project work. It should be noted that the cable and load model used in the project work are simplified models. These models will be improved in the master thesis. This also applies to the parametrization (electrical and mechanical) of the permanent magnet synchronous motor. In addition, new study cases with complete transmission system components will be simulated and analysed.

The master thesis will also include further investigations of input parameter effects on the start-up of the permanent magnet motor. As a consequence of the enhanced cable model, possible resonance phenomena in the cable may be identified, if time allows.

Project start-up: January 2014

Supervisor: Trond Toftevaag, Department of Electric Power Engineering

Preface

This study is carried out at the Department of Electric Power Engineering at the Department of Electric Power Engineering, Norwegian University of Science and Technology (NTNU) during Spring 2014.

OneSubsea AS has proposed the subject for this study. It is a part of their step in dimensioning sub-sea electrical power system components with component optimization in mind.

I would like to thank my supervisor Associate Professor Trond Toftevaag at the Department of Electric Power Engineering, NTNU for his valuable guidance, support, motivation and insightful suggestions throughout this study.

Additional thanks to my supervisor from OneSubsea AS, Rabah Zaimedine for his support with regards to Simulink, providing the necessary data required to fulfil this study, and taking the time to proof read this thesis, his input was invaluable.

I also wish to thank Professor Tore Undeland, Professor Robert Nilssen, Professor Lars Norum and Santiago Sanchez for some useful and interesting technical discussions during this study.

I must also thank my friends for being there and supporting me with friendly advice, cups of tea and random conversations about what is wrong with the world. My dancing buddies at NTNUI Hip-hop as well as my fabulous dance teachers, who should be showered with praise for what they have done for my self-confidence. To my new-found friends Xiaoxia Yang, Umair Ashraf and Krishna Neupane for their support, laughs and home-made dinner along the way. And to Selie Galami, for getting me out of the house occasionally and making sure I ate properly.

Finally, I would like to express my deepest gratitude to my mother, Zenaida P. Hauge for her unceasing support, encouragement and patience.

Kristiansen P. Baricuatro
Trondheim, June 2014

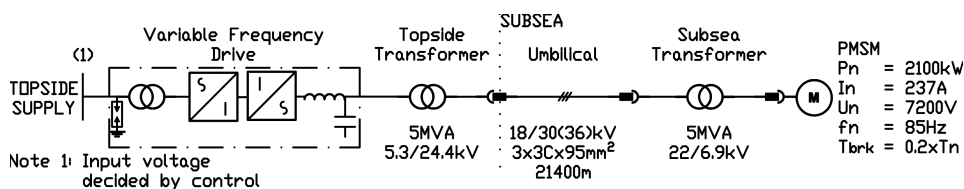
Abstract

The master thesis is a further investigation of the start-up procedure of a permanent magnet synchronous motor operated by variable frequency drive without position feedback via a long cable and transformers; as proposed in the specialization project, fall of 2013. The challenge is how to avoid large saturation in the transformers and motor while achieving the maximum possible starting torque with high cable resistance.

In order to model and simulate the electrical system, the simulation software Simulink is used.

A theoretical review is conducted in order to understand how to model system components, and how to start-up a permanent magnet synchronous motor while avoiding saturation in the transformers. Using the attained theoretical background, two permanent magnet synchronous motor models (with and without damper windings), an accurate pump load model, and three scalar control schemes which includes transmission system components for their control algorithms have been produced. In addition, a vector control scheme using field oriented control and extended Kalman filter for position estimation has been established and evaluated.

A study case comprising of a permanent magnet synchronous motor operated by a variable frequency drive without position feedback via a long cable and transformers has been defined as shown in the figure below.



As seen from the figure, the used permanent magnet synchronous motor in the study is a 2100 kW motor with a terminal voltage of 7200 V, a rated current of 237 A, and a rated frequency of 85 Hz. For the sake of comparison, the motor used in the preliminary project is a 66 kW motor with a terminal voltage of 350 V, a rated current of 115 A, and a rated frequency of 100 Hz. The motor is used to drive a pump load with a high breakaway torque, which is chosen to be 20% of the rated motor torque. The cable used in the base case of this study is 21.4 km long.

The purpose of the study case is to study the defined control schemes, the permanent magnet synchronous motor's start-up procedure, and the electrical system's steady state behaviour. This include investigation of input parameter effects on the start-up procedure.

The simulation results using the implemented pump load model shows that accurate load modelling affects the start-up procedure, as additional torque is required due to more

rotational friction components.

The simulation results of the study case show that the three proposed scalar control methods all are able to start-up the motor successfully, regardless of the initial rotor position. However, stability is not guaranteed at certain speed ranges due to the rise of small system disturbances. It has been shown that stability all throughout the entire applied frequency range can be guaranteed by adding damping to the system. This can be done by either adding transmission system components, motor damper windings, or a stabilization loop via frequency modulation.

It has been shown that cable length and applied frequency determines the accuracy of the transmission system voltage drop compensation algorithms of the proposed scalar control schemes. Increase in applied frequency and cable length increases the inaccuracy of the voltage drop compensation algorithms due to the ignored cable capacitance. Assuming that the maximum allowed voltage deviation from the required motor voltage during steady state is 0.1 pu, the longest cable length that can be used with the proposed scalar control schemes is 40 km. An exception is the open-loop scalar control scheme using constant voltage boosting, which can be used for cable lengths up to 20 km, due to its inaccurate calculation assumptions.

Additionally, it has been shown that the breakaway torque and the reference frequency ramp slope used by the controllers directly affect the torque oscillations during start-up. Additional torque oscillations can be experienced if the breakaway torque is too high or if the reference frequency ramp slope is too low due to the reduced torque build up, which consequently makes the start-up time higher.

The vector controller gave the best performance during load step tests due to its precise control of the rotor field. However, due to the requirement of rotor position feedback, position estimation is required. The investigated position estimation technique, extended Kalman filter is able to estimate speed and position with very little error. However, the initial rotor position is required by the extended Kalman filter algorithm in order to predict states properly.

Simulation results show that the vector control scheme offers the lowest possible start time due to its high performance. However, due to the requirement of initial rotor position of the sensorless vector controller, it can not be used during start-up, due to inaccuracies of predicting rotor position at zero speed. This leaves either the partial and delayed open-loop scalar control scheme or the closed-loop scalar control scheme to be the most viable start-up control schemes; as both control schemes offer comparably low start-up times, start-up currents and voltage boosting; which will consequently affect the dimensioning of the transformers. The vector controller can then be implemented after the start-up procedure using the selected scalar control scheme, in order to obtain the optimal controller performance.

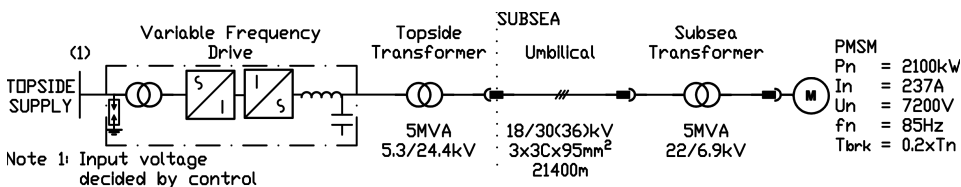
Sammendrag

Masteroppgaven er en videreføring av spesialiseringsprosjektet, høsten 2013 der oppstartsprosedyren av en permanent magnet synkronmotor som drives av en frekvensomformer uten rotor posisjonstilbakemelding, og som mates via en lang kabel og transformatorer. Utfordringen er hvordan man skal unngå magnetisk metning i transformatorer og motor, og samtidig oppnå størst mulig startmoment med høy kabelmotstand.

For å modellere og simulere det elektriske systemet, benyttes simuleringsprogrammet Simulink.

En teoretisk gjennomgang er gjennomført for å forstå hvordan man skal modellere systemkomponenter, og hvordan man starter opp en permanent magnet synkronmotor og samtidig unngå metning i transformatorene. På basis av dette, er det etablert to ulike permanent magnet synkronmotor modeller (med og uten dempeviklinger), en nøyaktig pumpe modell, og tre skalare kontrollsystemalgoritmer som inkluderer elementer i overføringssystemet. Et vektorkontrollsystem med feltorientert styring og Kalman filter for posisjonsestimering har også blitt etablert og evaluert.

En casestudie bestående av en permanent magnet synkronmotor som mates via en variabel frekvensomformer uten rotor posisjonstilbakemelding, via en lang kabel og transformatorer er definert som vist i figuren under.



Som det fremgår av figuren, inneholder modellen en permanent magnet synkronmotor på 2100 kW med en klemmespenning på 7200 V, en merkestrøm på 237 A, og en nominell frekvens på 85 Hz. For sammenligningens skyld, var motoren som ble brukt i forprosjektet en 66 kW motor med en klemmespenning på 350 V, en merkestrøm på 115 A, og en merkefrekvens på 100 Hz. Motoren blir brukt til å drive en pumpe med et høyt løsrivningsmoment som er valgt til å være 20 % av motorens nominelle dreiemoment. Kabelen som brukes i base case i denne studien er 21,4 km lang.

Hensikten med casestudien er å studere de etablerte kontrollsystemene, og oppstartsprosedyren for permanent magnet synkronmotoren. Dette inkluderer undersøkelse av hvordan inputparameterne påvirker oppstartsprosedyren.

Simuleringsresultatene for de case der den implementerte pumpe modellen er benyttet, viser at nøyaktig lastmodellering påvirker oppstartsprosedyren, siden ekstra moment er nødvendig som følge av høyere rotasjonsfriksjon.

Simuleringsresultatene av casestudien viser at de tre foreslåtte skalare kontrollsystemalgoritmene alle er i stand til å starte opp motoren på en vellykket måte, uavhengig av initiell rotorposisjon. Derimot er stabilitet ikke garantert for visse hastighetsområder ved små systemforstyrrelser. Det har vist seg at stabilitet gjennom hele det aktuelle frekvensområdet kan garanteres ved å legge til demping i systemet. Dette kan gjøres enten ved å legge til overføringssystem komponenter, motor dempeviklinger, eller en stabiliseringssløyfe via frekvensmodulering.

Det er vist at kabellengde og frekvens bestemmer nøyaktigheten av algoritmen som kompenserer spenningsfallet på grunn av overføringssystemet, for de foreslåtte skalare kontrollsystemene. Økning i frekvens og kabellengden øker unøyaktigheten av kompensasjonsalgoritmen på grunn av kabel kapasitans. Forutsatt at det maksimale tillatte spenningsavvik fra den nødvendige motorspenning under stabil tilstand er 0,1 pu, er den lengste kabellengde som kan brukes med de foreslåtte skalare kontrollsystemer 40 km. Et unntak er det åpen-sløyfe skalar kontrollsystemet som benytter konstant spenningboost; den kan kun brukes for kabellengder på opp til 20 km på grunn av uriktige beregningsforutsetninger.

I tillegg er det vist at løsrivningsmomentet og referansefrekvensen påvirker svingninger i dreiemomentet under oppstart. Mer dreiemomentsvingninger kan oppleves dersom løsrivningsmomentet er for høyt eller hvis stigningstallet for referansefrekvensrampe er for lavt. Dette er på grunn av den reduserte økning i dreiemomentet, noe som fører til høyere oppstartstid.

Vektorkontrolleren gir den beste ytelse under belastningssprang på grunn av den nøyaktige kontroll av rotor feltet. Men på grunn av kravet om rotorposisjonssignal, blir rotorposisjonsestimering nødvendig. Den undersøkte metode for rotorposisjonsestimering, Kalman filter er i stand til å estimere hastighet og posisjon med meget liten feil. I tillegg, er det vist at for å forutsi tilstander riktig, krever Kalman filter algoritmen initiell rotorposisjonen.

Simuleringsresultater viser at vektorkontrollsystemet gir lavest mulig oppstartstid på grunn av dens høye ytelse. Imidlertid, på grunn av Kalman filterets krav til initiell rotorposisjon, kan vektorkontrollsystemet ikke anvendes under oppstart. Dette er på grunn av unøyaktigheter ved å forutsi rotorensposisjon ved null hastighet. Dette etterlater enten det partielle og forsinket åpen-sløyfe skalar kontrollsystemet eller det lukket-sløyfe skalar kontrollsystemet som anbefalt løsning for oppstart. Dette er på grunn av deres lavere oppstartstider, oppstart strøm og spenningboost. Dette vil følgelig påvirke dimensjoneringen av transformatorene. Vektorkontrolleren kan da implementeres etter at oppstartsforløpet er over, for å oppnå optimal regulatorytelse.

Contents

Problem Description	i
Preface	iii
Abstract	v
Sammendrag	vii
Table of Contents	ix
List of Tables	xiii
List of Figures	xv
Nomenclature	xix
1 Introduction	1
1.1 Background	1
1.2 Summary of Fall Project 2013	2
1.3 Objectives	3
1.4 Scope of work	4
1.5 Limitations	4
1.6 Report structure	4
2 Theoretical background and mathematical models	7
2.1 PMSMs for subsea applications	7
2.2 Subsea power systems	8
2.3 Simulink, Simscape and SimPowerSystems	9
2.4 PMSM modelling	10
2.4.1 Damping and PMSM modelling	10
2.4.2 Mathematical model of a PMSM without damper windings	11
2.4.3 Mathematical model of a PMSM with damper windings	20
2.5 Control of PMSMs	22
2.5.1 Scalar control	22
2.5.2 Vector control	24
2.5.3 Control during start-up	25
2.6 PMSM start-up by reducing electrical frequency	25
2.7 Estimation of rotor position	26

2.7.1	Position information based on the measurement of voltages and currents	27
2.7.2	Position information based on the hypothetical rotor position . . .	27
2.7.3	Sensorless operation based on Kalman filtering	27
2.7.4	Position estimation based on state observers	28
2.7.5	Position information based on the inductance variation of the machine	28
2.8	Load modelling	29
2.8.1	Torque requirement	29
2.8.2	Rotational friction	29
2.9	Transformer modelling	31
2.10	Transformer saturation	32
2.11	Cable modelling	36
3	Study case and simulation description	39
3.1	General	39
3.1.1	Study case description	40
3.1.2	Simulation description	40
3.2	Supply system and VFD	41
3.3	PMSM	41
3.4	Transmission system	44
3.4.1	Transformers	44
3.4.2	Cable	45
4	Scalar controller	47
4.1	Control description	47
4.2	General controller components	48
4.2.1	Reference frequency	48
4.2.2	Voltage amplitude calculation	48
4.2.3	Controllable voltage source	49
4.3	Constant voltage boosting through rated stator current	50
4.3.1	Control scheme	50
4.3.2	Simulation model	51
4.4	Partial and delayed voltage boosting through rated stator current	52
4.4.1	Control scheme	52
4.4.2	Simulation model	53
4.5	Voltage boosting through measured stator current	54
4.5.1	Control scheme	54
4.5.2	Simulation model	59
4.6	Stabilization loop for PMSMs without damper windings	59
4.6.1	Implementation	59
4.6.2	Simulation model	61

5	Vector controller	63
5.1	Control description	63
5.2	Controller components	64
5.2.1	Current controller	64
5.2.2	Speed controller	67
5.2.3	Controllable voltage source and transformation matrices	69
5.3	Simulation model	70
5.4	Estimation of rotor position using Extended Kalman Filter	70
5.4.1	Speed and position estimation using EKF	70
5.4.2	Design of the covariance matrices	73
5.4.3	Simulation model	75
6	Simulations	77
6.1	General	77
6.1.1	Study case review	77
6.2	Open-loop scalar controller using constant voltage boosting	80
6.2.1	Testing the control scheme	80
6.2.2	Parameter variations	84
6.3	Open-loop scalar controller using partial and delayed voltage boosting	90
6.3.1	Testing the control scheme	90
6.3.2	Parameter variations	94
6.4	Closed-loop scalar controller	98
6.4.1	Testing the control scheme	98
6.4.2	Parameter variations	102
6.4.3	Response to load change	106
6.5	Vector controller	107
6.5.1	Testing the sensed vector controller	107
6.5.2	Testing the position estimator	108
7	Discussion	111
8	Conclusion	115
9	Recommendation for further work	119
	Bibliography	121
	Appendix	127
A	Simulink model	127
A.1	PMSM	128
A.2	Mechanical characteristics	134
A.3	Transmission system	139
A.4	Measurements	140
A.5	Controller	141
A.5.1	Open-loop scalar controller	141

CONTENTS

A.5.2	Closed-loop scalar controller	146
A.5.3	Closed-loop scalar controller with stabilization loop	149
A.5.4	Vector controller	151
A.5.5	Vector controller with EKF	153
B	Matlab simulation script	159
C	Attached files	163

List of Tables

3.1	PMSM parameters	41
3.2	Topside step-up transformer parameters	44
3.3	Subsea step-down transformer parameters	45
3.4	Cable parameters	45
5.1	Fuzzy logic controller - Rules of ΔQ	74
5.2	Fuzzy logic controller - Rules of ΔR	74
6.1	Per-unit representation - Rated and peak values	78
6.2	Per-unit representation - Primary base values	79
6.3	Per-unit representation - Secondary base values	79

LIST OF TABLES

List of Figures

1.1	Electrical system topology - Preliminary project's study case	2
2.1	Comparison between system efficiency of a PMSM and an IM system . . .	8
2.2	Typical subsea electrical system topologies	8
2.3	Circuit representation of a PMSM without damper windings showing the dq axes in arbitrary rotating reference frame	11
2.4	Equivalent circuit of a PMSM in the rotor's $qd0$ reference frame	19
2.5	Circuit representation of a PMSM with damper windings showing the dq axes in arbitrary rotating reference frame	20
2.6	Equivalent circuit of a PMSM in the rotor's $qd0$ reference frame	21
2.7	Self synchronization concept for PMSM	22
2.8	Open-loop V/Hz control of PMSM	23
2.9	Closed loop V/Hz control of PMSM	23
2.10	Field oriented control of PMSM	24
2.11	Direct torque control of PMSM	25
2.12	Diagram of a PMSM showing the components of the magnetic flux density	25
2.13	PMSM start-up failure	26
2.14	Pump torque requirement	29
2.15	Rotational friction torque	30
2.16	Equivalent circuit of a one-phase two-winding transformer	31
2.17	B-H curve of a ferromagnetic material showing saturation	32
2.18	Relationship between excitation current, voltage, flux and B-H curve . . .	34
2.19	Relationship between excitation current, voltage, flux and B-H curve during saturation	35
2.20	Long line with distributed parameters	36
2.21	Equivalent π model for long length line	38
3.1	Electrical system topology - Base case	40
3.2	Electrical system topology - Test case	40
3.3	Simulation subsystems	41
3.4	User-made PMSM blocks	42
3.5	Mechanical connection between the PMSM and the mechanical characteristics block	42
3.6	Inside the mechanical characteristics block, showing the user-made rotational friction and load torque blocks	43
3.7	Rotational friction torque	43

LIST OF FIGURES

4.1	Scalar controller subsystem	48
4.2	Constant voltage boosting through rated stator current	50
4.3	Overview of the transmission system components	50
4.4	Equivalent circuit of the transmission system	51
4.5	Open-loop scalar controller overview	51
4.6	Partial and delayed voltage boosting through rated stator current	52
4.7	Steady-state vector diagram of a PMSM in rotor dq reference frame	54
4.8	Overview of the transmission system components	55
4.9	Short line model	55
4.10	Equivalent circuit of the transmission system	56
4.11	Steady-state vector diagram of the electrical system	57
4.12	Low pass filter response ($w_n = 50 \text{ Hz}, \zeta = 0.707$)	58
4.13	Closed-loop scalar controller overview	59
4.14	Frequency modulation signal calculation	60
4.15	High pass filter response ($w_n = 50 \text{ Hz}, \zeta = 10$)	61
4.16	Closed-loop scalar controller with stabilization loop overview	61
5.1	Field oriented controller overview	63
5.2	Vector control with applied voltages	65
5.3	Current control loop	66
5.4	Speed control loop	68
5.5	Sensorless field oriented controller using EKF overview	70
5.6	Sensorless field oriented controller using EKF and FL overview	75
6.3	Constant voltage boosting simulation measurements - All waveforms - Test case, 3 sec simulation time	80
6.4	Constant voltage boosting simulation measurements - Torque waveforms - Test case, 1.5 sec simulation time	81
6.5	Constant voltage boosting simulation measurements - Torque and speed waveforms - Test case, 100 sec simulation time	82
6.6	Constant voltage boosting simulation measurements - All waveforms - Base case, 3 sec simulation time	83
6.7	Constant voltage boosting simulation measurements - Torque and speed waveforms - Base case, 100 sec simulation time	83
6.8	Constant voltage boosting simulation measurements - Voltage waveforms - Base case, 100 sec simulation time	84
6.9	Constant voltage boosting simulation measurements - Start-up currents and times as a function of reference frequency slope - Base case	85
6.10	Constant voltage boosting simulation measurements - Torque waveforms - Base case, 0.001 and 0.075 pu/sec reference frequency slope	85
6.11	Constant voltage boosting simulation measurements - Deviation from actual required motor voltage as a function of speed - Base case	86
6.12	Constant voltage boosting simulation measurements - Torque and position waveforms - Base case, different initial rotor positions, 2 sec simulation time	87

6.13	Constant voltage boosting simulation measurements - Torque waveforms - Base case, 0.075 pu/sec reference frequency slope, Motor model 1.0 and 2.1, 10 sec simulation time	88
6.14	Constant voltage boosting simulation measurements - Torque waveforms - Base case, $T_{brk} = 0.1 T_{rated}$ and $T_{brk} = 0.4 T_{rated}$, 1.5 sec simulation time	89
6.15	Partial and delayed voltage boosting simulation measurements - All waveforms - Test case, 3 sec simulation time	90
6.16	Partial and delayed voltage boosting simulation measurements - All waveforms - Base case, 3 sec simulation time	92
6.17	Partial and delayed voltage boosting simulation measurements - Torque and speed waveforms - Base case, 100 sec simulation time	93
6.18	Partial and delayed voltage boosting simulation measurements - Voltage waveforms - Base case, 5 sec simulation time	94
6.19	Partial and delayed voltage boosting simulation measurements - Start-up currents and times as a function of reference frequency slope - Base case .	95
6.20	Partial and delayed voltage boosting simulation measurements - Deviation from actual required motor voltage as a function of speed - Base case . . .	95
6.21	Partial and delayed voltage boosting simulation measurements - Torque and position waveforms - Base case, different initial rotor positions, 2 sec simulation time	96
6.22	Partial and delayed voltage boosting simulation measurements - Torque waveform - Base case, 14 Hz border frequency, 100 sec simulation time .	97
6.23	Partial and delayed voltage boosting simulation measurements - Torque waveform - Base case, 5 Hz border frequency, 2 sec simulation time . . .	97
6.24	Closed-loop scalar control simulation measurements - All waveforms - Test case, 3 sec simulation time	98
6.25	Closed-loop scalar control simulation measurements - All waveforms - Base case, 3 sec simulation time	100
6.26	Closed-loop scalar control simulation measurements - Torque waveform - Base case, 100 sec simulation time	101
6.27	Closed-loop scalar control simulation measurements - Torque waveform - Base case with stabilization loop, 100 sec simulation time	102
6.28	Closed-loop scalar control simulation measurements - Start-up currents and times as a function of reference frequency slope - Base case with stabilization loop	103
6.29	Closed-loop scalar control simulation measurements - Deviation from actual required motor voltage as a function of speed - Base case with stabilization loop	103
6.30	Closed-loop scalar control simulation measurements - Required stabilization loop gain as a function of cable length - Base case with stabilization loop	104
6.31	Closed-loop scalar control simulation measurements - Torque and position waveforms - Base case with stabilization loop, different initial rotor positions, 2.5 sec simulation time	105

LIST OF FIGURES

6.32	Closed-loop scalar control simulation measurements - Speed waveform - Base case with stabilization loop, 100 sec simulation time	106
6.33	Vector control simulation measurements - Torque and speed waveform - Test case, 100 sec simulation time	107
6.34	Vector control simulation measurements - Speed demand and estimated speed and position errors - Test case, 20 sec simulation time	108
6.35	Vector control simulation measurements - Speed demand and estimated speed and position errors - Test case, 20 sec simulation time	109
6.36	Vector control simulation measurements - Speed demand and estimated speed and position errors - Test case, 90 degrees initial rotor position, 20 sec simulation time	110

Nomenclature

Abbreviations

AC	Alternating Current	MTPA	Maximum Torque Per Amperes
DC	Direct Current	NTNU	Norwegian University of Science and Technology
DTC	Direct Torque Control	PI	Proportional Integral
EFL	Electrical Flying Leads	PMSM	Permanent Magnet Synchronous Motor
EKF	Extended Kalman Filter	PWM	Pulse Width Modulation
FL	Fuzzy Logic	rms	root-mean-square
FOC	Field Oriented Control	V/Hz	Volts per Hertz
HV	High Voltage	VFD	Variable Frequency Drive
IM	Induction Motor		
mmf	magnetomotive force		

Subscripts

<i>abc</i>	Three phase stator variables	<i>m</i>	Magnetizing (Current), Mutual (Inductance), Permanent Magnet (Flux Linkage), Mechanical (speed, position and Torque)
<i>brk</i>	Breakaway friction	<i>max</i>	Maximum
<i>c</i>	Core (Transformer), Coulomb (Friction)	<i>min</i>	Minimum
<i>comp</i>	Compensation	<i>o</i>	Output
<i>dem</i>	Demand (Torque)	<i>qd0</i>	Park qd0 variables
<i>e</i>	Excitation	<i>r</i>	Rotor, Electrical (speed and position), Receiving end (Transmission line)
<i>em</i>	Electromechanical	<i>s</i>	Stator, Sending end (Transmission line), Subsea (Transformer)
<i>fric</i>	Rotational friction	<i>sat</i>	Saturation
<i>g</i>	Air gap	<i>t</i>	Topside (Transformer)
<i>k</i>	Damper winding	<i>tot</i>	Total
<i>ls</i>	Leakage (Inductance)		

Superscripts

'	Peak, Referred to stator/primary side (Rotor/Transformer variables)	*	Conjugate, Reference (Control)
---	--	---	--------------------------------

Symbols

γ	Propagation constant	i	Instantaneous current
λ	Flux linkage	J	Inertia
μ	Permeability	L	Inductance
μ_0	Vacuum permeability	M	Magnetization
ω	Angular speed	N, n	Number of turns
ϕ	Flux	P	Power loss, Average power
ψ	Flux linkage per second	p	Number of poles, instantaneous power
σ	Electrical conductivity	r	Resistance
θ	Angular position	T	Torque
ζ	Damping ratio	V	Average voltage
B	Magnetic induction	v	Instantaneous voltage
E	Induced voltage	W	Energy loss
f	Frequency	X	Reactance
f_b	Border frequency	Y	Admittance
H	Magnetic field strength	Z	Impedance
H_c	Coercivity	Z_c	Characteristic impedance
I	Average current		

Introduction

This chapter introduces the problem that is addressed in this project and the motivations for solving it; and consequently state the project objectives, scopes and limitations.

1.1 Background

With the increasing demand for oil and gas production, oil and gas companies start to step out into deeper waters with continuously increasing differential pressure requirements. These requirements are easily met by Permanent Magnet Synchronous Motors (PMSM), in contrast with conventional induction motors.

The subsea motors are typically operated by dedicated topside Variable Frequency Drive (VFD) and fed via a long cable. Due to the combination of long umbilical cable length and the required voltage of the motors, the transmission voltage is elevated through the topside step-up transformer and if required, reduced to the appropriate motor voltage through a subsea transformer.

Usage of topside VFD to start and operate subsea motor with long tieback for increased process efficiency and process optimization is now common [1], notably for systems using asynchronous machines [2, 3]. The same cannot be said for synchronous machines due to its huge control dependencies.

Control of PMSM is usually done by closed-loop vector control with position feedback due to its fast response and good performance characteristics. However due to harsh operating conditions found subsea, usage of resolver or encoder to provide position feedback to the control system is not preferable. This necessitates sensor-less vector control schemes [4, 5, 6, 7], which are usually problematic during PMSM start-up procedure. Due to this, start-up of PMSM is typically done through scalar control; by controlling both applied voltage and frequency.

Subsea pump motors have typically high breakaway torque, which requires high voltage boost during start-up. This in combination with long umbilical cable length requires even higher voltage boost applied on the step-up transformers, which may saturate the transformer's core.

Finally, due to its higher power density and torque ratio, use of PMSM for subsea applications with long tieback distance and high breakaway torque becomes more and more relevant. Limited expertise and right tools for analyses and calculations can easily lead to over dimensioned components; along with its unwanted consequences on component size, weight and cost. Moreover, if the system is under or improperly dimensioned, it will not be possible to start the motor if the transformer saturates.

1.2 Summary of Fall Project 2013

A project with title "Sensorless Start-up of Permanent Magnet Synchronous Motor with Long Tie-back" [8] was done in the fall semester 2013, as a preliminary project for this thesis.

The purpose of this preliminary project is to analyse and optimize the start-up procedure of a PMSM operated by a variable frequency drive without position feedback via a long cable and transformers. The challenge is how to avoid saturation in the transformer while achieving the maximum possible starting torque with high cable resistance.

A theoretical review is conducted in order to understand how to model, and start-up a PMSM without damper windings while avoiding saturation in the transformer. Using the attained theoretical background, three scalar Volts per Hertz (V/Hz) control schemes without position feedback had been defined and established in Simulink for motor start-up simulation purposes. These Simulink models are used to model the variable frequency drive. The proposed control algorithms only take into account the resistance of the cable when calculating the required voltage reference.

As an initial step to solving the problem, a simple study case comprising of a permanent magnet synchronous motor operated by a variable frequency drive without position feedback via a long cable has been defined. The purpose of this study case is to study the PMSM's start-up procedure.

The electrical system topology for the study case is shown in the figure below; along with key component parameters.

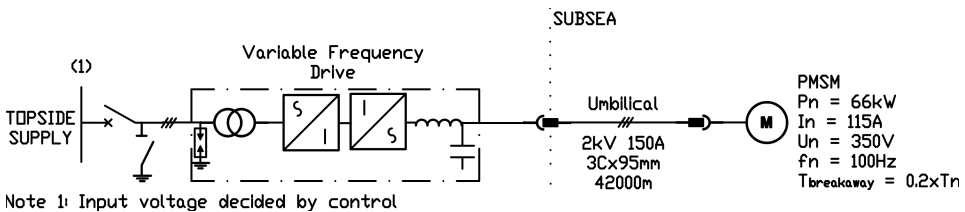


Figure 1.1: Electrical system topology - Preliminary project's study case

As seen from the figure, the used PMSM in the study is a 66 kW motor with a terminal voltage of 350 V, a rated current of 115 A, and a rated frequency of 100 Hz. [9] The PMSM

is used to drive a pump load with a high breakaway torque, which is chosen to be 20% of the rated motor torque.

The cable used in the study is 42 km long, based on the Åsgard subsea gas compression project's cable [10], which is the longest planned step-out distance to date.

The start-up simulation results of the study case show that the three established control methods all are able to start-up the motor with varying resulting start-up behaviours. Moreover, synchronization is still obtained despite varying the initial rotor position for all control methods.

It was concluded that the control scheme using stator current measurements as feedback allows the lowest possible voltage boosting while achieving the maximum possible starting torque, which will consequently affect the dimensioning of the transformer.

Moreover, PMSMs without damper windings requires a stabilizing loop which uses rotor position feedback in order to guarantee stable operation. Thus, in order to operate without rotor position feedback, rotor position estimation is required.

1.3 Objectives

The master thesis is a further investigation of the start-up procedure of a PMSM operated by variable frequency drive without position feedback via a long cable and transformers; as proposed in the specialization project, fall of 2013 [8]. The challenge is how to avoid large saturation in the transformers and motor while achieving the maximum possible starting torque with high cable resistance.

As described in section 1.2, three scalar V/Hz control schemes without position feedback were defined and established in Simulink for motor start-up simulation purposes in the project work. The master thesis should investigate possible optimization of these control schemes.

A study case comprising of a permanent magnet synchronous motor operated by a variable frequency drive without position feedback via a long cable and transformers is to be defined, simulated and analysed via a pre-defined simulation software. The existing simulation models are to be improved if required.

The master thesis will also include further investigations of input parameter effects on the start-up of the PMSM. As a consequence of the enhanced cable model, possible resonance phenomena in the cable may be identified.

See also the problem description for further details.

1.4 Scope of work

The following scope of work is based on the objectives described:

- Establish and describe the electrical system topology of the study case. Moreover, describe the system components used and how they are modelled.
- Improve Simulink PMSM model to suit transient power system analyses.
- Improve the V/Hz controllers established during the project work.
- Investigate viable position estimators and implement at least one of them.
- Improve load model in order to incorporate stribek friction.
- Establish, simulate and analyse a dynamic simulation model of the study case in Simulink using the improved models.
- Investigate input parameter effects on the start-up of the permanent magnet motor.

The following tasks can be done if time permits:

- Discussion around transformer sizing approximation.
- Identify possible resonance phenomena in the cable.
- Implement vector control scheme.
- Use multilevel drive instead of an ideal voltage source for harmonics study.

1.5 Limitations

The following limitations are applied:

- The converter is to operate without a rotor position feedback; and may be modelled as a voltage source with a variable V/Hz profile during start-up.
- Cost consideration will not been included in the study.
- Transformer structural design will not be included in the study.

1.6 Report structure

In order to ease readability of the master thesis, some aspects of the project work [8] has been included in the report. These consist of the required theoretical background the reader should know in order to understand the models and scripts implemented in the study.

After this introductory chapter, all the theoretical background and the mathematical models required by the study is given in chapter 2.

Chapter 3 describes the electrical system of the study case, the simulation, and the corresponding Simulink model of the system components.

Chapter 4 describes the mathematical equations used to model the V/Hz controller in order to accelerate the PMSM from stand-still to synchronous speed, and the simulation model that is used in Simulink.

Chapter 5 describes the mathematical equations used to model the vector controller, and the simulation model that is used in Simulink.

The simulation results of the study are presented in chapter 6.

Chapter 7 discusses the simulation results-and chapter 8 presents the conclusions. Recommendations for further work are presented in chapter 9.

Matlab codes used for the simulations, the Simulink model of the study case as well as Simulink blocks of custom-made subsystems are presented in the appendices.

The figures given throughout the report have been created using Adobe Illustrator, Photoshop and AutoCad Electrical 2014. The simulations were executed in Matlab Simulink with the Simscape and SimPowerSystems libraries. The report was written in the typesetting program \LaTeX .

Chapter 1. Introduction

Theoretical background and mathematical models

This chapter presents the necessary theoretical background and mathematical models required by this project.

2.1 PMSMs for subsea applications

Conservative projections show that the world energy consumption will grow by 56 percent between 2010 and 2040. Throughout this period, fossil fuels are still expected to continue supplying most of the energy used worldwide. In order to satisfy the projected energy consumption by 2040, liquids production needs to increase by 28.3 million barrels per day while natural gas production needs to increase by more than 70 trillion cubic feet [11].

In order to satisfy the increasing demand for oil and gas production, undeveloped ultra-deep water fields need to be exploited while production on maturing fields need to be maintained. Both of these are attained by using subsea-based booster and compression systems, which requires establishing subsea power stations with long tiebacks¹ from a stand-alone facility or the shore. These subsea boosters and compressors are basically pumps driven by a motor.

Because of the increasing distance between the wells and stand-alone facilities, higher differential pressure pump are required. In order for conventional centrifugal and helicoaxial subsea pumps to deliver higher pressures, either more stages have to be added to the pumps or existing pumps need to operate at higher speeds.

¹Tieback is a subsea term which refers to the connection between the oil well and the stand-alone facility or the shore. 7

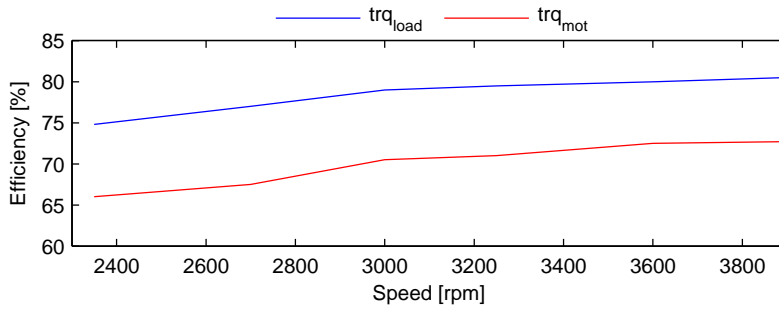


Figure 2.1: Comparison between system efficiency of a PMSM and an IM system [12]

A recent study shows a significant improvement in PMSM efficiency over conventional Induction Motor (IM) used to drive subsea pumps for same diameter size motors, due to its higher power density and torque ratio. This can be clearly seen in **Figure 2.1**. Field tests performed to relate these efficiency improvements to production operating costs show that the PMSM is able to use 20 % less power for the same production. [12]

2.2 Subsea power systems

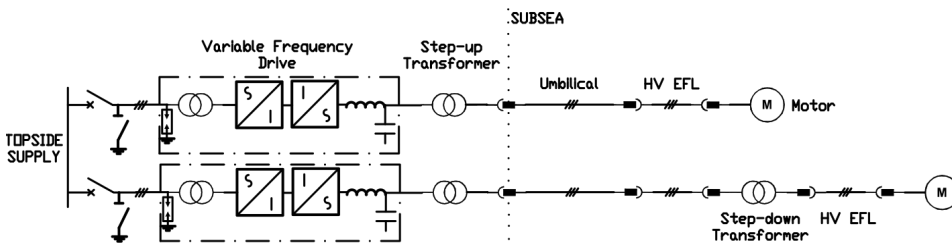


Figure 2.2: Typical subsea electrical system topologies

Figure 2.2 shows the typical three-phase electrical system topologies used to supply subsea motors. This section will provide a brief description of the power system components shown in the figure.

Supply system and VFD

All topside equipments for the pump system are typically installed in local equipment rooms onboard the stand-alone facility or the shore. This includes the supply system and VFD.

The dedicated VFD can also be placed subsea, however this poses a significant technological gap since subsea VFD technology is presently not fully mature. Power electronics

components still can not withstand high pressure and needs to be placed in a low pressure environment. This necessitates an enclosure with thick and heavy walls which increases drive size and cost, and lowers thermal conductivity. Consequently, topside VFD is more preferable.

The PMSM's speed is given by the topside VFD's output frequency. The method used to control the motor's speed can be either scalar or vector control, depending on the requirement of the application.

Transformers

Transformers are typically used in subsea applications due to the combination of long umbilical cable length and the required voltage of the subsea motors, as shown in **Figure 2.2**. Topside step-up transformers are used to elevate the transmission voltage in order to reduce the power loss along the transmission lines. Subsea step-down transformers are used to supply the correct subsea motor voltage; if required.

Saturation of the transformer's core must be avoided as this may cause severe damage to the transformer. The saturation phenomena of the transformer's ferromagnetic core is discussed in section 2.10.

Cable

The transmission cables represents a crucial part of the electrical power system as it comprises the topside to subsea motor transmission of power.

PMSM

The PMSM drives the subsea mechanical load which is typically a booster or compression system, as discussed earlier. This corresponds to a load characteristics with a high breakaway torque and a load torque which is a quadratic function of speed.

2.3 Simulink, Simscape and SimPowerSystems

The simulations are to be performed using Simulink, Simscape and SimPowerSystems softwares.

Simulink

Simulink, developed by MathWorks, is a block diagram environment for multidomain simulation and Model-Based Design. It supports system-level design, simulation, automatic code generation, and continuous test and verification of embedded systems. [13]

Simulink provides a graphical editor, customizable block libraries, and solvers for modeling and simulating dynamic systems. It is integrated with Matlab, enabling users to incorporate Matlab algorithms into models and export simulation results to Matlab for further analysis. [13] These factors make Simulink a powerful engineering tool.

Simscape

Simscape extends Simulink by providing a single environment for modeling and simulating physical systems spanning mechanical, electrical, and other physical domains. It provides fundamental building blocks from these domains that users can assemble into models of physical components, such as electric motors, hydraulic valves, and ratchet mechanisms. [14]

Simscape models can be used to develop control systems and system-level performance. Users can extend the libraries using the Matlab based Simscape language, which enables text-based authoring of physical modeling components, domains, and libraries. [14] Using the Simscape language, users can control exactly which effects are captured in their models.

With Simscape, users build a model of a system just as they would assemble a physical system. Simscape employs a physical network approach, also referred to as acausal modeling, to model building: Components (blocks) corresponding to physical elements, such as pumps, motors, and op-amps, are joined by lines corresponding to the physical connections that transmit power. This approach lets users describe the physical structure of a system rather than the underlying mathematics. From the model, which closely resembles a schematic, Simscape automatically constructs the differential algebraic equations that characterize the system's behavior. These equations are integrated with the rest of the Simulink model, and the differential equations are solved directly. The variables for the components in the different physical domains are solved simultaneously, avoiding problems with algebraic loops. [14] This is the main advantage of using Simscape's physical system modeling.

SimPowerSystems

Moreover, SimPowerSystems extends Simulink with component libraries and analysis tools for modeling and simulating electrical power systems. The libraries offer models of electrical power components, including three-phase machines, electric drives, and power electronics components. Harmonic analysis, calculation of total harmonic distortion, load flow, and other key electrical power system analyses are automated. [15]

2.4 PMSM modelling

2.4.1 Damping and PMSM modelling

Electrical system small disturbances may cause rotor angle instability in a PMSM, which risks it to lose synchronism. This problem is solved typically by using damper windings and rotor cage, which generates opposing fields during periods of disturbances, thus improving machine stability. However, the usage of damper windings and rotor cage increases machine cost, weight and volume, and at the same time reduces machine reliability, thus making their usage along with the PMSM not preferable.

The lack of physical damper windings in a PMSM does not mean that there are no other

factors that cause damping in the machine. Solid pole shoes for instance introduces a slight damping effect. The resistivity of the magnets themselves is so high that their effect on the damping can be neglected. If the rotor frame is solid, it introduces a slight damping effect. A laminated rotor frame provides so few paths for the eddy currents that there seems in practice to be no damping either. These damper elements can be modelled through equivalent damper windings as well.

All the other factors causing damping, the damper winding itself excluded, are difficult to estimate by any other means than measuring. As a consequence, a simplified model without damper windings is typically used if motor data is scarce. This simplified model is often justifiable due to the large air gap typically found in PMSMs. The large air gap suppresses armature reaction, which in turn reduces the consequences of electrical disturbances. However, in order to accurately simulate the motor start-up, eventual damper elements still needs to be taken into account.

Due to these, two mathematical models of a PMSM are presented. One model without damper windings which is intended to be used for cases when motor data is scarce. And another model with damper windings which is intended to be used for cases when the complete motor data is available, or for cases when the effects of damping elements are studied.

2.4.2 Mathematical model of a PMSM without damper windings

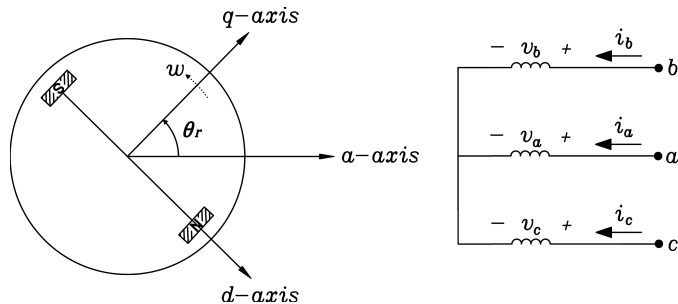


Figure 2.3: Circuit representation of a PMSM without damper windings showing the dq axes in arbitrary rotating reference frame

Figure 2.3 illustrates the stationary a-axis which corresponds to the stator phase's magnetic axis. Additionally, the dq-axes with the frame of reference fixed on the stationary a-axis are shown, in which angle θ_r corresponds to the angle between the a-axis and the q-axis. The d-axis is chosen to be aligned with the magnetic north pole of the rotor magnet, while the q-axis is in 90 electrical degrees ahead of the direct axis.

Equations in phase quantities

For a PMSM without damper windings, the applied voltage to each of the stator phase windings shown in **Figure 2.3** is balanced by a resistive drop and a $d\lambda/dt$ term, and can be expressed by the following matrix equation: [16]

$$\begin{aligned} \mathbf{v}_{abc} &= r_s \mathbf{i}_{abc} + \frac{d}{dt} \boldsymbol{\lambda}_{abc} \\ \begin{bmatrix} v_a \\ v_b \\ v_c \end{bmatrix} &= r_s \begin{bmatrix} i_a \\ i_b \\ i_c \end{bmatrix} + \frac{d}{dt} \begin{bmatrix} \lambda_a \\ \lambda_b \\ \lambda_c \end{bmatrix} \end{aligned} \quad (2.1)$$

In the above, r_s is the stator resistance per phase while \mathbf{v}_{abc} , \mathbf{i}_{abc} and $\boldsymbol{\lambda}_{abc}$ are the stator phase voltage, current and flux linkage matrix respectively.

The stator winding flux linkage ($\boldsymbol{\lambda}_{abc}$) of each phase is the sum of flux linkages related to the stator current ($\boldsymbol{\lambda}_{abc(s)}$) and the mutual flux linkage resulting from the permanent magnet ($\boldsymbol{\lambda}_{abc(r)}$), which are expressed by the following matrix equations:

$$\boldsymbol{\lambda}_{abc} = \boldsymbol{\lambda}_{abc(s)} + \boldsymbol{\lambda}_{abc(r)} \quad (2.2)$$

$$\boldsymbol{\lambda}_{abc(s)} = \mathbf{L} \mathbf{i}_{abc} = \begin{bmatrix} L_{aa} & L_{ab} & L_{ac} \\ L_{ba} & L_{bb} & L_{bc} \\ L_{ca} & L_{cb} & L_{cc} \end{bmatrix} \mathbf{i}_{abc} \quad (2.3)$$

$$\boldsymbol{\lambda}_{abc(r)} = \lambda'_m \begin{bmatrix} \sin \theta_r \\ \sin (\theta_r - 2\pi/3) \\ \sin (\theta_r + 2\pi/3) \end{bmatrix} \quad (2.4)$$

Here, λ'_m is the amplitude of the mutual flux linkages resulting from the permanent magnet as seen from the reference. The diagonal and off-diagonal elements of the inductance matrix \mathbf{L} are the stator self and mutual inductances respectively.

The total stator self inductance of each phases are given as: [17]

$$L_{aa} = L_{ls} + L_{m1} - L_{m2} \cos 2\theta_r \quad (2.5)$$

$$L_{bb} = L_{ls} + L_{m1} - L_{m2} \cos 2(\theta_r + 2\pi/3) \quad (2.6)$$

$$L_{cc} = L_{ls} + L_{m1} - L_{m2} \cos 2(\theta_r - 2\pi/3) \quad (2.7)$$

where L_{ls} is the leakage inductance, L_{m1} is the average single phase magnetizing inductance and L_{m2} is half the amplitude of the varying magnetizing inductance due to saliency. L_{m1} and L_{m2} are given by:

$$L_{m1} = \frac{\pi \mu_0 r l}{2(l_{g,min} + l_{g,max})} \left(\frac{N_s}{p} \right)^2 \quad (2.8)$$

$$L_{m2} = \frac{\pi \mu_0 r l}{4(l_{g,min} - l_{g,max})} \left(\frac{N_s}{p} \right)^2 \quad (2.9)$$

On the above, μ_0 is the air's permeability, r is the radius, l is the axial length of the air gap, N_s is the number of turns per phase, p is the number of poles, $l_{g,min}$ is the minimum air gap length and $l_{g,max}$ is the maximum air gap length.

The stator mutual inductances are given as: [17]

$$L_{ab} = L_{ba} = -\frac{L_{m1}}{2} - L_{m2} \cos\left(2\theta_r - \frac{2\pi}{3}\right) \quad (2.10)$$

$$L_{bc} = L_{cb} = -\frac{L_{m1}}{2} - L_{m2} \cos\left(2\theta_r + \frac{2\pi}{3}\right) \quad (2.11)$$

$$L_{ca} = L_{ac} = -\frac{L_{m1}}{2} - L_{m2} \cos 2\theta_r \quad (2.12)$$

Using the equations (2.3) - (2.12), the stator winding flux linkage (2.2) may be expanded as:

$$\begin{aligned} \lambda_a = & [L_{ls} + L_{m1} - L_{m2} \cos 2\theta_r]i_a - \left[\frac{L_{m1}}{2} + L_{m2} \cos\left(2\theta_r - \frac{2\pi}{3}\right)\right]i_b \\ & - \left[\frac{L_{m1}}{2} + L_{m2} \cos 2\theta_r\right]i_c + \lambda_m \sin \theta_r \end{aligned} \quad (2.13)$$

$$\begin{aligned} \lambda_b = & -\left[\frac{L_{m1}}{2} + L_{m2} \cos\left(2\theta_r - \frac{2\pi}{3}\right)\right]i_a + [L_{ls} + L_{m1} - L_{m2} \cos 2(\theta_r \\ & + \frac{2\pi}{3})]i_b - \left[\frac{L_{m1}}{2} + L_{m2} \cos\left(2\theta_r + \frac{2\pi}{3}\right)\right]i_c + \lambda_m \sin\left(\theta_r - \frac{2\pi}{3}\right) \end{aligned} \quad (2.14)$$

$$\begin{aligned} \lambda_c = & -\left[\frac{L_{m1}}{2} + L_{m2} \cos 2\theta_r\right]i_a - \left[\frac{L_{m1}}{2} + L_{m2} \cos\left(2\theta_r + \frac{2\pi}{3}\right)\right]i_b \\ & + [L_{ls} + L_{m1} - L_{m2} \cos 2(\theta_r - \frac{2\pi}{3})]i_c + \lambda_m \sin\left(\theta_r + \frac{2\pi}{3}\right) \end{aligned} \quad (2.15)$$

Equations in space vector form

Instantaneous three phase components can be represented by a space vector along the reference phase axis, in order to simplify calculations and provide compact notations. Choosing the stationary a-axis as the reference, the resultant space vector of any three phase quantities (stator phase currents, voltages and flux linkages) is calculated by multiplying instantaneous phase values (f_a , f_b and f_c) by the stator winding orientation (\vec{a} and \vec{a}^2), as shown in equation (2.16).

$$\vec{f}_{abc} = \frac{2}{3}[f_a + \vec{a}f_b + \vec{a}^2f_c] \quad (2.16)$$

where

$$\vec{a} = e^{j2\pi/3} \quad (2.17)$$

$$\vec{a}^2 = e^{j4\pi/3} \quad (2.18)$$

Additionally, the conjugate of \vec{f}_{abc} can be defined as follows:

$$\vec{f}_{abc}^* = \frac{2}{3}[f_a + \vec{a}^2 f_b + \vec{a} f_c] \quad (2.19)$$

Applying equation (2.16) to (2.1), the voltage equation can be written as:

$$\vec{v}_{abc} = r_s \vec{i}_{abc} + \frac{d}{dt} \vec{\lambda}_{abc} \quad (2.20)$$

where

$$\vec{v}_{abc} = \frac{2}{3}[v_a + \vec{a}v_b + \vec{a}^2v_c] \quad (2.21)$$

$$\vec{i}_{abc} = \frac{2}{3}[i_a + \vec{a}i_b + \vec{a}^2i_c] \quad (2.22)$$

$$\vec{\lambda}_{abc} = \frac{2}{3}[\lambda_a + \vec{a}\lambda_b + \vec{a}^2\lambda_c] \quad (2.23)$$

In the above, r_s is the stator resistance per phase while \vec{v}_{abc} , \vec{i}_{abc} and $\vec{\lambda}_{abc}$ are the stator phase voltage, current and flux linkage space vectors respectively.

The stator winding flux linkage of each phase is the sum of flux linkages related to the stator current and the mutual flux linkage resulting from the permanent magnet. The flux linkage space vector can then be expressed using equations (2.13) - (2.15) as follows:

$$\vec{\lambda}_{abc} = (L_{ls} + \frac{3}{2}L_{m1})\vec{i}_{abc} - \frac{3}{2}L_{m2}\vec{i}_{abc}^* e^{j2\theta_r} + \lambda'_m e^{j(\theta_r - \pi/2)} \quad (2.24)$$

Here, λ'_m is the amplitude of the mutual flux linkages resulting from the permanent magnet as seen from the reference. θ_r is the rotor angle. L_{ls} is the leakage inductance. L_{m1} and L_{m2} are magnetizing inductances based on motor construction.

qd0 transformation

It is evident from equation (2.24) that the stator winding flux linkages and hence the stator winding inductances are a function of the rotor angle which varies with time at the rate of the rotor's angular speed. These time-dependent coefficients presents computational complexity which could produce numerical problems.

In order to obtain time-invariant inductance coefficients, the three phase (a, b, c) stator variables can be transformed into Park ($q, d, 0$) variables in rotor reference frame, that is turned at the system frequency as shown in **Figure 2.3**. This transformation may be expressed as shown in equation (2.25).

$$f_{qd0} = T_{qd0} f_{abc} \quad (2.25)$$

where f_{qd0} is the $(q, d, 0)$ component matrix, f_{abc} is the (a, b, c) component matrix, and T_{qd0} is the Park transformation matrix, as shown in the following equations:

$$f_{qd0}^T = [f_q \quad f_d \quad f_0] \quad (2.26)$$

$$f_{abc}^T = [f_a \quad f_b \quad f_c] \quad (2.27)$$

$$T_{qd0} = \frac{2}{3} \begin{bmatrix} \cos \theta_r & \cos(\theta_r - 2\pi/3) & \cos(\theta_r + 2\pi/3) \\ \sin \theta_r & \sin(\theta_r - 2\pi/3) & \sin(\theta_r + 2\pi/3) \\ 1/2 & 1/2 & 1/2 \end{bmatrix} \quad (2.28)$$

The zero sequence component f_0 associated with the symmetrical components:

$$f_0 = \frac{1}{3}(f_a + f_b + f_c) \quad (2.29)$$

will be equal to zero under balanced conditions, since $f_a + f_b + f_c = 0$.

Equations in the rotor's qd0 reference frame

Using equation (2.26), the three phase voltage, current and flux linkage space vectors in stationary a-axis reference frame can be related to the dq space vectors in rotating reference frame as follows:

$$\vec{v}_{abc} = \vec{v}_{qd} e^{j\theta_r} \quad (2.30)$$

$$\vec{i}_{abc} = \vec{i}_{qd} e^{j\theta_r} \quad (2.31)$$

$$\vec{\lambda}_{abc} = \vec{\lambda}_{qd} e^{j\theta_r} \quad (2.32)$$

Inputting the above equations into equation (2.20) gives:

$$\begin{aligned} \vec{v}_{abc} &= r_s \vec{i}_{abc} + \frac{d}{dt} \vec{\lambda}_{abc} \\ \vec{v}_{dq} e^{j\theta_r} &= r_s \vec{i}_{qd} e^{j\theta_r} + \frac{d}{dt} (\vec{\lambda}_{qd} e^{j\theta_r}) \\ \vec{v}_{dq} e^{j\theta_r} &= r_s \vec{i}_{qd} e^{j\theta_r} + \frac{d\vec{\lambda}_{qd}}{dt} e^{j\theta_r} + j \frac{d\theta_r}{dt} \vec{\lambda}_{qd} e^{j\theta_r} \end{aligned} \quad (2.33)$$

Hence the voltage equation can be expressed in rotor dq reference frame as:

$$\vec{v}_{qd} = r_s \vec{i}_{qd} + \frac{d\vec{\lambda}_{qd}}{dt} + j w_r \vec{\lambda}_{qd} \quad (2.34)$$

where $w_r = \frac{d}{dt} \theta_r$ is the instantaneous speed.

Separating the real and imaginary components in equation (2.34) gives:

$$v_q = r_s i_q + \frac{d\lambda_q}{dt} + w_r \lambda_d \quad (2.35)$$

$$v_d = r_s i_d + \frac{d\lambda_d}{dt} - w_r \lambda_q \quad (2.36)$$

Solving for the flux linkage space vector, equation (2.24) in rotor dq reference frame gives:

$$\begin{aligned} \vec{\lambda}_{qd} &= \vec{\lambda}_{abc} e^{-j\theta_r} \\ &= (L_{ls} + \frac{3}{2}L_{m1})\vec{i}_{abc} e^{-j\theta_r} - \frac{3}{2}L_{m2}\vec{i}_{abc}^* e^{j2\theta_r} e^{-j\theta_r} + \lambda'_m e^{j(\theta_r - \frac{\pi}{2})} e^{-j\theta_r} \\ &= (L_{ls} + \frac{3}{2}L_{m1})\vec{i}_{abc} e^{-j\theta_r} - \frac{3}{2}L_{m2}\vec{i}_{abc}^* e^{j\theta_r} + \lambda'_m e^{-j\frac{\pi}{2}} \\ &= (L_{ls} + \frac{3}{2}L_{m1})\vec{i}_{qd} - \frac{3}{2}L_{m2}(\vec{i}_{qd})^* + \lambda'_m e^{-j\frac{\pi}{2}} \end{aligned} \quad (2.37)$$

Here, λ'_m is the amplitude of the mutual flux linkages resulting from the permanent magnet as seen from the reference. L_{ls} is the leakage inductance, L_{m1} is the average single phase magnetizing inductance and L_{m2} is half the amplitude of the varying magnetizing inductance due to saliency.

It can be seen from equation (2.37) the inductance coefficients are no longer time-dependent, compared to equation (2.24).

The dq magnetizing inductances are defined as: [17]

$$L_{md} = \frac{3}{2}(L_{m1} + L_{m2}) \quad (2.38)$$

$$L_{mq} = \frac{3}{2}(L_{m1} - L_{m2}) \quad (2.39)$$

Solving for L_{m1} and L_{m2} gives:

$$L_{m1} = \frac{L_{md} + L_{mq}}{3} \quad (2.40)$$

$$L_{m2} = \frac{L_{md} - L_{mq}}{3} \quad (2.41)$$

Inputting above equations to equation (2.37) gives:

$$\vec{\lambda}_{qd} = (L_{ls} + \frac{L_{md} + L_{mq}}{2})\vec{i}_{qd} - \frac{L_{md} - L_{mq}}{2}(\vec{i}_{qd})^* + \lambda'_m e^{-j\frac{\pi}{2}} \quad (2.42)$$

Separating the real and imaginary components in equation (2.42) and defining L_d and L_q as the sum of the leakage inductance and the corresponding magnetizing inductance of the axis gives equations (2.43) and (2.44).

$$\begin{aligned}\lambda_q &= (L_{ls} + L_{mq})i_q \\ &= L_q i_q\end{aligned}\quad (2.43)$$

$$\begin{aligned}\lambda_d &= (L_{ls} + L_{md})i_d + \lambda'_m \\ &= L_d i_d + \lambda'_m\end{aligned}\quad (2.44)$$

Inputting above equations to equations (2.35) and (2.36) gives the following dq voltage equations:

$$v_q = r_s i_q + L_q \dot{i}_q + w_r (L_d i_d + \lambda'_m) \quad (2.45)$$

$$v_d = r_s i_d + L_d \dot{i}_d - w_r L_q \dot{i}_q \quad (2.46)$$

Electrical power and torque

The instantaneous input power can be expressed as:

$$\begin{aligned}p_e &= \frac{3}{2} \Re(\vec{v}_{qd} \vec{i}_{qd}^*) \\ &= \frac{3}{2} (\vec{v}_d \vec{i}_d + \vec{v}_q \vec{i}_q)\end{aligned}\quad (2.47)$$

Using equations (2.45) and (2.46) to express the voltage components in terms of flux linkages and voltages gives:

$$\begin{aligned}p_i &= \frac{3}{2} r_s [(i_d)^2 + (i_q)^2] + \frac{3}{4} \frac{d}{dt} [L_d (i_d)^2 + L_q (i_q)^2] + \frac{3}{2} w_r [\lambda_d i_q - \lambda_q i_d] \\ &= p_{cu} + p_{dW} + p_{em}\end{aligned}\quad (2.48)$$

where p_{cu} represents the armature resistance loss, p_{dW} represents the rate of change of armature magnetic energy, and p_{em} represents the electromechanical power which is transferred across the air gap.

The output torque can be obtained by dividing the electromechanical power by the rotor's angular mechanical speed w_m as follows:

$$T_{em} = \frac{P_{em}}{w_m} \quad (2.49)$$

The relationship between the mechanical speed and the electrical speed and the electrical rotor position θ_r is given by:

$$\frac{d\theta_r}{dt} = \omega_r = \frac{p}{2} \omega_m \quad (2.50)$$

Here, p is the number of poles.

Inputting above equation to equation (2.49) and substituting the dq flux components of T_{em} with equations (2.43) and (2.44) results to equation (2.51)

$$T_{em} = \frac{3p}{4} [\lambda_m i_q + (L_d - L_q) i_d i_q] \quad (2.51)$$

Mechanical equation

The mechanical system can be represent as follows:

$$\frac{d\omega_m}{dt} = \frac{1}{J} (T_{em} - T_{fric} - T_m) \quad (2.52)$$

where J is the combined inertia of the rotor and mechanical load, T_{fric} is the rotational friction torque and T_m is the load torque.

Summary

Using the Park transformation matrix, the $qd0$ equations of a PMSM without damper windings have thus been derived and are as follows:

Voltage equations:

$$\begin{aligned} v_q &= r_s i_q + \frac{d\lambda_q}{dt} + \lambda_d \frac{d\theta_r}{dt} \\ v_d &= r_s i_d + \frac{d\lambda_d}{dt} - \lambda_q \frac{d\theta_r}{dt} \\ v_0 &= r_s i_0 + \frac{d\lambda_0}{dt} \end{aligned} \quad (2.53)$$

Flux linkages:

$$\begin{aligned} \lambda_q &= (L_{ls} + L_{mq}) i_q \\ &= L_q i_q \\ \lambda_d &= (L_{ls} + L_{md}) i_d + L_{md} i'_m \\ &= L_d i_d + \lambda'_m \\ \lambda_0 &= L_{ls} i_0 \end{aligned} \quad (2.54)$$

Electromagnetic torque:

$$T_{em} = \frac{3p}{4} (\lambda_d i_q - \lambda_q i_d) \quad (2.55)$$

For modelling purposes, the permanent magnet inductance, L_{rc} associated with its recoil slope, can be lumped with the d-axis mutual inductance [18].

The resulting equivalent circuit of a PMSM without damper windings in the rotor's $qd0$ reference frame can then be established, as shown in **Figure 2.4**.

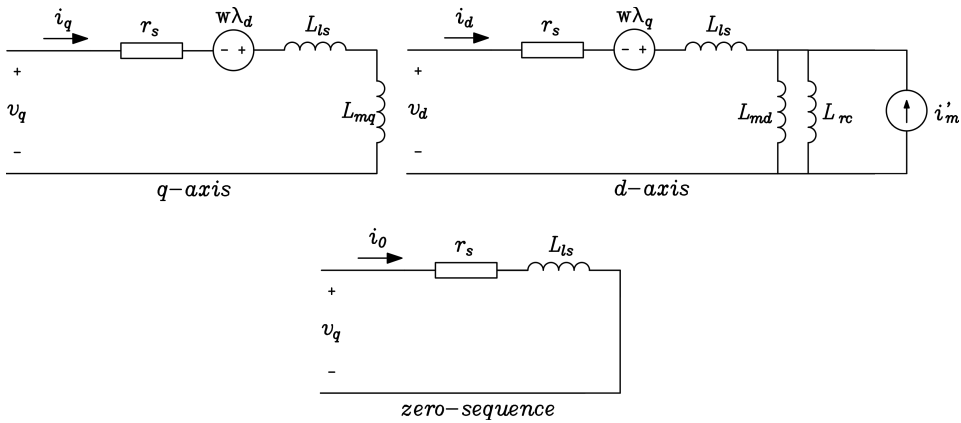


Figure 2.4: Equivalent circuit of a PMSM in the rotor's $qd0$ reference frame

Following are the symbols used in both the $qd0$ equations and the equivalent circuit:

v_q, v_d, v_0	$qd0$ -axis voltages
i_q, i_d, i_0	$qd0$ -axis currents
i'_m	equivalent magnetizing current of the permanent magnet, referred to the stator side
$\lambda_q, \lambda_d, \lambda_0$	$qd0$ -axis flux linkages
λ'_m	flux linkage of the permanent magnet
r_s	armature or stator winding resistance
L_{mq}, L_{md}	mutual inductances in q-axis and d-axis
L_{ls}	armature or stator winding leakage inductance
L_q, L_d	qd -axis synchronous inductances
L_{rc}	permanent magnet inductance
p	number of poles
θ_r	rotor angle
T_{em}	electromagnetic torque

2.4.3 Mathematical model of a PMSM with damper windings

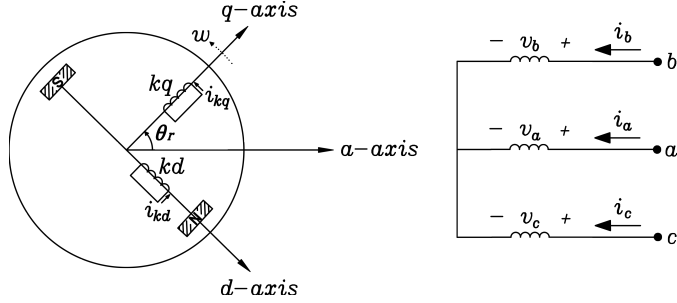


Figure 2.5: Circuit representation of a PMSM with damper windings showing the dq axes in arbitrary rotating reference frame

Including eventual damper elements in the previously established model is as simple as adding a set of damper windings in both d and q axes, as shown in **Figure 2.5**. Following the same derivation procedure as described in the previous section, the $qd0$ equations of a PMSM with damper windings are as follows:

Voltage equations:

$$\begin{aligned}
 v_q &= r_s i_q + \frac{d\lambda_q}{dt} + \lambda_d \frac{d\theta_r}{dt} \\
 v_d &= r_s i_d + \frac{d\lambda_d}{dt} - \lambda_q \frac{d\theta_r}{dt} \\
 v_0 &= r_s i_0 + \frac{d\lambda_0}{dt} \\
 0 &= r'_{kd} i'_{kd} + \frac{d\lambda'_{kd}}{dt} \\
 0 &= r'_{kq} i'_{kq} + \frac{d\lambda'_{kq}}{dt}
 \end{aligned} \tag{2.56}$$

Flux linkages:

$$\begin{aligned}
 \lambda_q &= (L_{ls} + L_{mq}) i_q + L_{mq} i'_{kq} \\
 &= L_q i_q + L_{mq} i'_{kq} \\
 \lambda_d &= (L_{ls} + L_{md}) i_d + L_{md} i'_{kd} + L_{md} i'_m \\
 &= L_d i_d + L_{md} i'_{kd} + \lambda'_m \\
 \lambda_0 &= L_{ls} i_0 \\
 \lambda'_{kq} &= L_{mq} i_q + L'_{kqkq} i'_{kq} \\
 \lambda'_{kd} &= L_{md} i_d + L'_{kdkd} i'_{kd} + L_{md} i'_m \\
 &= L_{md} i_d + L'_{kdkd} i'_{kd} + \lambda'_m
 \end{aligned} \tag{2.57}$$

Electromagnetic torque:

$$T_{em} = \frac{3p}{4}(\lambda_d i_q - \lambda_q i_d) \quad (2.58)$$

The resulting equivalent circuit of a PMSM with damper windings in the rotor's $qd0$ reference frame can then be established, as shown below.

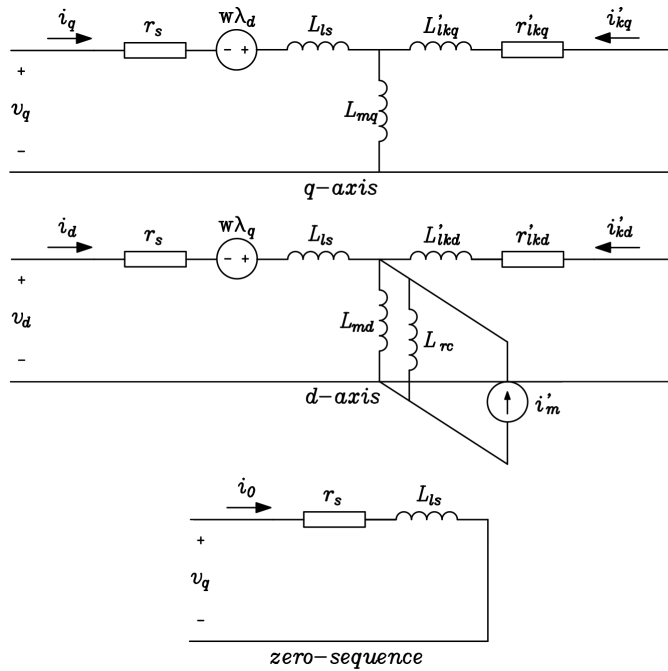


Figure 2.6: Equivalent circuit of a PMSM in the rotor's $qd0$ reference frame

Following are the symbols used in both the $qd0$ equations and the equivalent circuit:

v_q, v_d, v_0	$qd0$ -axis voltages
i_q, i_d, i_0	$qd0$ -axis currents
i'_{kq}, i'_{kd}	qd -axis damper winding currents, referred to the stator side
i'_m	equivalent magnetizing current of the permanent magnet, referred to the stator side
$\lambda_q, \lambda_d, \lambda_0$	$qd0$ -axis flux linkages
$\lambda'_{kq}, \lambda'_{kd}$	qd -axis damper winding flux linkages
λ'_m	flux linkage of the permanent magnet
r_s	armature or stator winding resistance
r'_{kq}, r'_{kd}	qd -axis damper winding resistances, referred to the stator side
L_{mq}, L_{md}	mutual inductances in q-axis and d-axis
L_{ls}	armature or stator winding leakage inductance
L'_{lkq}, L'_{lkd}	qd -axis damper winding leakage inductances, referred to the stator side
L'_{kqkq}, L'_{kdkd}	qd -axis damper winding self-inductances, referred to the stator side
L_q, L_d	qd -axis synchronous inductances
L_{rc}	permanent magnet inductance
p	number of poles
θ_r	rotor angle
T_{em}	electromagnetic torque

2.5 Control of PMSMs

Since a PMSM is a synchronous motor, average torque can be produced when the applied Alternating Current (AC) excitation is precisely synchronized with the rotor frequency and instantaneous position. This requirement is always met by continuously measuring the rotor's absolute angular position so that excitation can be switched among the PMSM motor phases in exact synchronism with the rotor's motion. This concept is known as self-synchronization and is illustrated in **Figure 2.7**. [19]

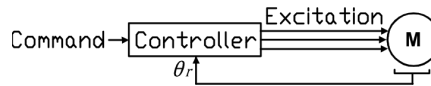


Figure 2.7: Self synchronization concept for PMSM

In order to ensure self-synchronization at required speed, different control methods can be used. It can either be through scalar control or vector control. This section introduces both control schemes, in order to provide necessary background for the more detailed controller chapters of the thesis.

2.5.1 Scalar control

Scalar control schemes controls the speed of the motor by varying the magnitudes of two parameters. Typically, the applied voltage and the frequency are chosen as the control

parameters. This control method is thus referred to as scalar V/Hz control and can be implemented with either an open-loop or a closed loop control scheme. It is a relatively easy control scheme and is well suited for applications which does not require high dynamic performance.

Open-loop V/Hz control

PMSMs can be designed with an induction motor squirrel cage winding (damper windings) embedded along the surface of the rotor. This hybridization adds a component of asynchronous torque production when the PMSM rotor does not rotate in synchronous speed. This makes it possible for the PMSM machine to operate stably from an inverter without position sensors. This simplification makes it practical to use a simple constant V/Hz control algorithm as shown in **Figure 2.8** to achieve open loop speed control for application such as pumps and fans that do not require fast dynamic response. According to this approach, a sinusoidal voltage Pulse Width Modulation (PWM) algorithm is implemented which linearly increases the amplitude of the applied fundamental voltage amplitude in proportion to the speed command to hold the stator magnetic flux approximately constant. [19]

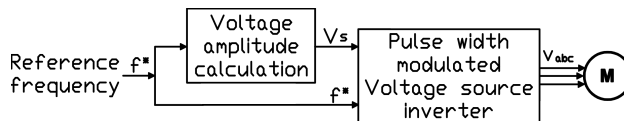


Figure 2.8: Open-loop V/Hz control of PMSM

The open loop nature of this control scheme makes it necessary to avoid sudden large changes in the speed command or the applied load to avoid undesired loss of synchronization of the PMSM. [19]

Closed loop V/Hz control

For PMSMs without an induction motor squirrel cage windings, the lack of asynchronous torque production does not guarantee stable operation, and synchronization of the rotor with the excitation frequency. In order to compensate for power and speed oscillation due to instability, rotor position feedback is required as shown in **Figure 2.9**.

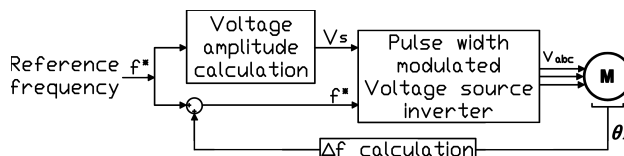


Figure 2.9: Closed loop V/Hz control of PMSM

However due to harsh operating conditions found subsea, usage of revolver or encoder

to provide position feedback to the control system is not preferable. This necessitates sensor-less control schemes through the use of rotor position estimators.

2.5.2 Vector control

Vector control is a more advanced control method that utilizes current space vectors in order to control the motor flux and the torque. This results to a more robust control scheme which gives fast response and good performance characteristics compared to scalar control. There exists different kind of vector control. The two most used ones are Direct Torque Control (DTC) and Field Oriented Control (FOC).

Both of these methods were based on the same idea that transforms the machine's three phase variables into two phase variables to separate of stator current two orthogonal component as flux-component and torque-component which already exist naturally in dc motors, as shown in section 2.4. Naturally, the DTC and the FOC have some structural and behavioural differences. [20]

Field oriented control

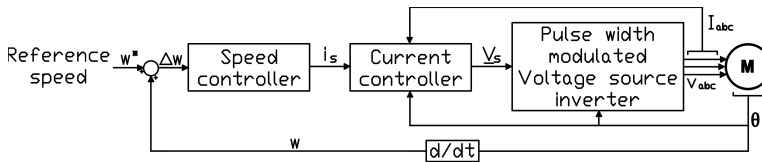


Figure 2.10: Field oriented control of PMSM

Figure 2.10 shows an overview of a controller using FOC. As seen in the figure, this control scheme uses position and current feedback along with regulators to calculate the voltage reference.

This control strategy provides high torque quality at all speed ranges. [20] The drawbacks are increased complexity due to the current and speed regulators, and the requirement of position and speed measurement.

Direct torque control

Figure 2.11 shows an overview of a controller using DTC. As seen in the figure, this control scheme estimates flux and torque using measured currents and the voltages of the motor. The torque and flux errors, which are obtained by comparing the reference and observed values, are converted to control signals by hysteresis comparators. A switching table is then used to determine the optimum switching inverter states. [20]

Unlike the FOC, the DTC does not require any current regulator, complex coordinate transformation, not needed many parameters, etc. Consequently, these comparisons makes DTC much simpler than FOC.

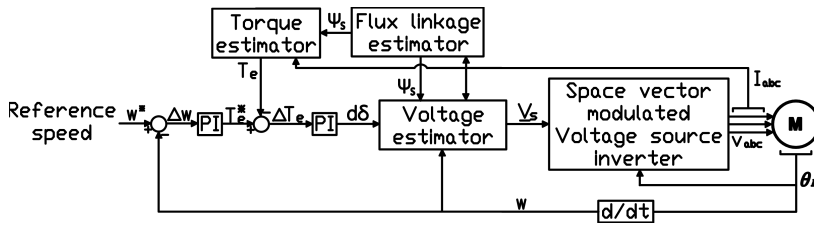


Figure 2.11: Direct torque control of PMSM

However, DTC presents some disadvantages like control difficulties at low speed and high current and torque ripples. [20] Consequently, this makes the control scheme unfavourable for motor start-up.

2.5.3 Control during start-up

Sensor-less vector control schemes are usually problematic during PMSM start-up procedure, due to inaccuracies of predicting rotor position at zero speed [4, 5, 6, 7].

Due to this, start-up of PMSM is typically done through scalar control; by controlling both applied voltage and frequency.

2.6 PMSM start-up by reducing electrical frequency

Motor action

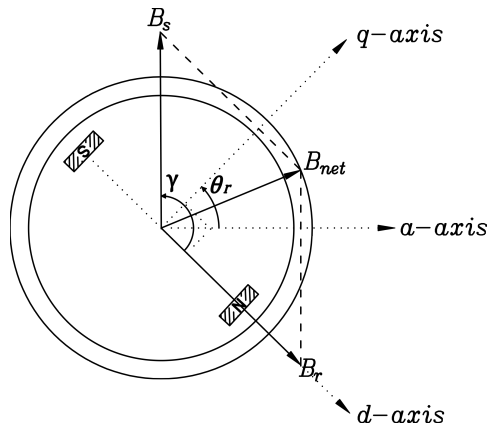


Figure 2.12: Diagram of a PMSM showing the components of the magnetic flux density

Figure 2.12 shows the components of the magnetic flux density inside a PMSM, where \vec{B}_s is the stator magnetic field, \vec{B}_r is the rotor magnetic field established by the permanent magnet, and γ is the angle between \vec{B}_s and \vec{B}_r .

Torque is induced on the rotor shaft as a consequence of the permanent magnet trying to align with the stator magnetic field, and can therefore be expressed as follows:

$$\begin{aligned}\tau_{ind} &= k\vec{B}_r \times \vec{B}_s \\ &= kB_r B_s \sin \gamma \quad (\text{counterclockwise})\end{aligned}\quad (2.59)$$

Equation (2.59) shows that the torque is induced only when both magnetic field vectors are not aligned, and the direction of the induced torque is dependent on the alignment of both magnetic field vectors. The induced torque will be positive (counter clockwise) when $0^\circ < \gamma < 180^\circ$ and negative when $180^\circ < \gamma < 360^\circ$.

Start-up procedure

Figure 2.13 shows a result from a Simulink simulation where the applied frequency to the PMSM terminals are set to the synchronous frequency during start-up. As shown, the net induced torque over an electrical cycle is zero. As a consequence, the PMSM fails to accelerate from stand-still and wobbles in one position.

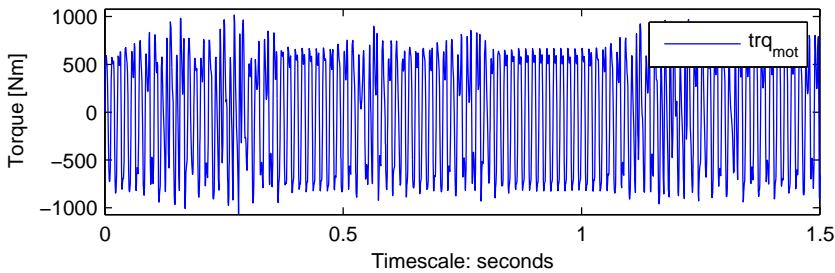


Figure 2.13: PMSM start-up failure

A positive net torque over an electrical cycle is required in order to accelerate the rotor. This can be achieved by reducing the speed of the stator magnetic field, and thus the electrical frequency to a low enough value so that the rotor can accelerate and lock in with it during one half-cycle of the magnetic field's rotation [21]. This is achieved using scalar control as discussed in section 2.5.

2.7 Estimation of rotor position

In order to remove the usage of position sensor in several vector control schemes, rotor position must be estimated. In sinusoidal back emf motors, the rotor position is required continuously; and in trapezoidal back emf motors, it is enough to have the rotor position every 60 degrees to obtain proper switching sequence.

Several schemes for position sensorless operation of PMSM exists and are based on one of the following techniques: [22]

1. Position information based on the measurement of voltages and currents
2. Position information based on the hypothetical rotor position
3. Sensorless operation based on Kalman filtering
4. Position estimation based on state observers
5. Position information based on the inductance variation of the machine

2.7.1 Position information based on the measurement of voltages and currents

This method uses measured stator voltages and currents in order to construct a flux linkage signal through which the phase angle of the stator current can be controlled.

The performance of this position estimation method depends on the quality and accuracy of the measured stator voltages and currents, and thus the estimated flux linkages. Parameter variations due to temperature and saturation will also affect the accuracy of the position estimation. [22]

This position estimation method is described in detail on the following papers: [23, 24, 25, 26, 27].

2.7.2 Position information based on the hypothetical rotor position

This method uses the difference between the detected actual state variables and estimated state variables to obtain the position information. The controller determines the applied voltage to the motor according to the hypothetical rotor position, which is not necessarily coincident with the actual rotor position. The ideal applied voltage is calculated using the detected current. The difference between the actual and ideal voltage is proportional to the angular difference between hypothetical and actual rotor positions. Self-synchronization is achieved by reducing this angular difference to zero. [22]

Due to the required computational accuracy of this position estimation method, fast processors with high resolution is required. [22]

This position estimation method is described in detail on the following papers: [28, 29, 30, 31].

2.7.3 Sensorless operation based on Kalman filtering

A Kalman filter provides an optimum observation from noisy sensed signals and process that are disturbed by noise. The Kalman filter approach provides an efficient and viable on-line estimation of speed and rotor position. [22]

The rotor position is estimated using PMSM state equations, and voltage and current measurements.

The Kalman filter is an optimum state estimator. The filter's estimation is constantly corrected by an additional term originated from the measurements. The estimated state $x'(n)$ is the minimum variance estimate of $x(n)$. The Kalman filter consists of a two-step process: prediction and filtering. The predictor takes states from k^+ to $(k+1)^-$, whereas the filter takes states from time $(k+1)^-$ to $(k+1)^+$. The prediction part of the algorithm calculates the next estimate values for x and the state covariance matrix P before the new measurement is made. In doing so, the predictor uses the state variable equations, state transition matrix, disturbance covariance Q , and measurement covariance R . [22]

The function of the filter is to correct the estimation process in a recursive manner. The filter constantly works on the output and corrects its quality in a recursive manner based on measured values. Based on the deviation from the estimated value, the filter provides an optimum output value at the next output instant. [22]

The main disadvantage to Kalman filters is the design and tuning of the covariance matrices, which determines the position estimation performance.

This position estimation method is described in detail on the following papers: [32, 33, 34].

2.7.4 Position estimation based on state observers

In a state observer, the output is defined as a combination of states, and this output is compared with the equivalent measured output of the real motor. Any error between the two signals is used to correct the state trajectory of the observer. [22]

The stability of an observer is an important issue in providing accurate position estimation. Optimal observer stability is obtained by optimizing the observer gains under all operating conditions.

This position estimation method is described in detail on the following papers: [35, 36, 37, 38, 39].

2.7.5 Position information based on the inductance variation of the machine

This method utilizes the variation of the inductance as a function of the rotor position, to estimate the rotor position; assuming that the inductance of the motor along the d-axis and the q-axis are not equal.

The scheme requires prior calculation of inductance. Hence the position information depends on the accuracy of the calculation of the inductance. [22] Consequently, the scheme requires accurate motor parameters.

This position estimation method is described in detail on the following papers: [40, 41].

2.8 Load modelling

As discussed earlier, subsea-based booster and compression systems are basically pumps driven by a motor. In order to properly model this load type, two characteristics of the load are required to be covered: its torque requirement, and its rotational friction torque.

2.8.1 Torque requirement

A pump is a variable torque load with a torque demand that increases with a quadratic function of speed. Consequently, the torque demand can be expressed as follows:

$$T_{dem} = K_t w_m^2 \quad (2.60)$$

Here, K_t is the machine's torque constant, and w_m is the rotor's angular mechanical speed. This corresponds to the speed torque curve shown in **Figure 2.14**.

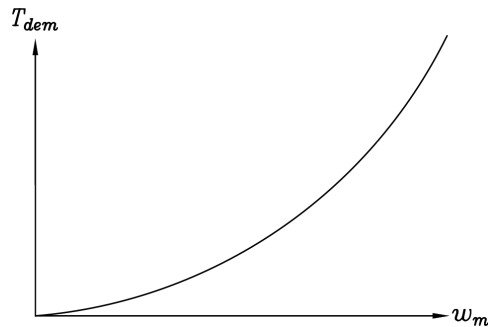


Figure 2.14: Pump torque requirement

2.8.2 Rotational friction

Friction is the tangential reaction force between two surfaces in contact. Physically these reaction forces are the results of many different mechanisms, which depend on contact geometry and topology, properties of the bulk and surface materials of the bodies, displacement and relative velocity of the bodies and presence of lubrication. [42]

The friction in contact between rotating bodies represents an additional torque demand and is thus required to be properly modelled.

The classical models of friction consist of different components, which each take care of certain aspects of the friction force. Rotational friction torque is thus assumed to be the sum of Stribeck, Coulomb, and viscous components [42], as shown in **Figure 2.15**.

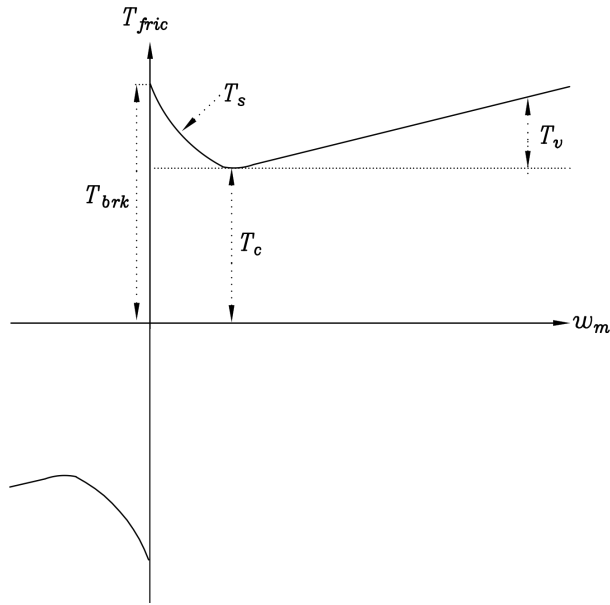


Figure 2.15: Rotational friction torque

The Stribeck friction, F_s is the negatively sloped characteristics taking place at low velocities. The Coulomb friction, F_c results in a constant torque in any velocity. The viscous friction, F_v opposes motion with the torque directly proportional to the relative velocity. The sum of the Coulomb and Stribeck frictions at the vicinity of zero velocity is often referred to the stiction or breakaway friction, F_{brk} .

The rotational friction torque is approximated as follows: [42]

$$T_{fric} = (T_c + (T_{brk} - T_c))e^{-c_v|w_m|}sign(w_m) + fw_m \quad (2.61)$$

where

T_{fric}	Rotational friction torque
T_c	Coulomb friction torque
T_{brk}	Breakaway friction torque
c_v	coefficient
w_m	rotor angular mechanical speed
f	Viscous friction coefficient

2.9 Transformer modelling

Equivalent circuit

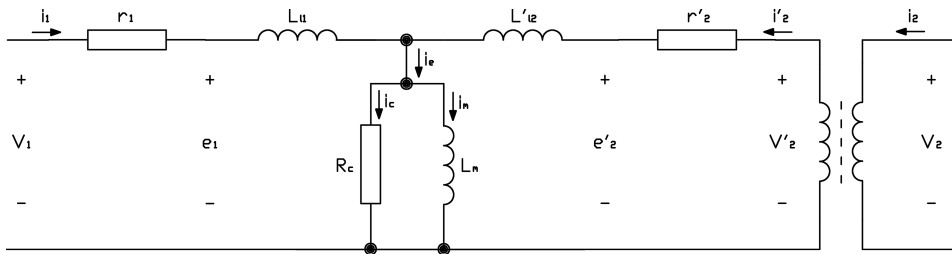


Figure 2.16: Equivalent circuit of a one-phase two-winding transformer

Figure 2.16 shows the equivalent circuit of a one-phase two winding transformer, referred to the primary side. i_j , u_j , r_j and L_{lj} are the current, voltage, winding resistance and leakage inductance of the j th ($j \in [1, 2]$) windings respectively. i_e is the excitation current. r_c and i_c are the core loss resistance and current respectively. L_m and i_m are the magnetizing inductance and current respectively.

Electrical equations

The following voltage equations can be derived from **Figure 2.16**:

$$v_1 = i_1 r_1 + e_1 = i_1 r_1 + L_{l1} \frac{di_1}{dt} + L_m \frac{di_m}{dt} = i_1 r_1 + \frac{d\lambda_1}{dt} = i_1 r_1 + \frac{1}{\omega_b} \frac{d\psi_1}{dt} \quad (2.62)$$

$$v'_2 = i'_2 r'_2 + e'_2 = i'_2 r'_2 + L'_{l2} \frac{di'_2}{dt} + L_m \frac{di_m}{dt} = i'_2 r'_2 + \frac{d\lambda_2}{dt} = i'_2 r'_2 + \frac{1}{\omega_b} \frac{d\psi_2}{dt} \quad (2.63)$$

where λ_j and ψ_j are the flux linkage and flux linkage per second of the j th ($j \in [1, 2]$) windings respectively, and ω_b corresponds to the base frequency.

The following relationships applies for the voltage equations above:

$$v'_2 = \frac{N_1}{N_2} v_2 \quad (2.64)$$

$$i'_2 = \frac{N_2}{N_1} i_2 \quad (2.65)$$

$$r'_2 = \left(\frac{N_1}{N_2} \right)^2 r_2 \quad (2.66)$$

$$L'_{l2} = \left(\frac{N_1}{N_2} \right)^2 L_{l2} \quad (2.67)$$

The magnetizing current can be derived through the excitation current and the core loss current as shown below.

$$i_m = i_e - i_c = i_1 + i_2' - i_c \quad (2.68)$$

2.10 Transformer saturation

Why does the transformer's core saturate?

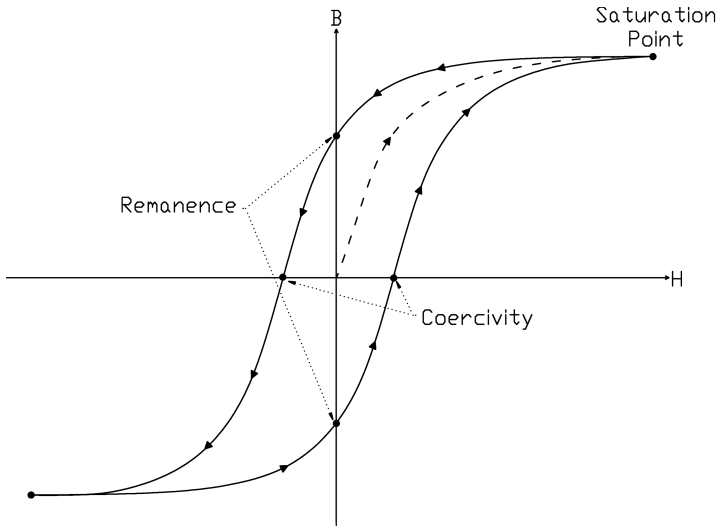


Figure 2.17: B-H curve of a ferromagnetic material showing saturation

The transformer's core is a ferromagnetic material which has non-linear magnetic behaviour that can be described graphically in terms of their hysteresis loop as shown in **Figure 2.17**. This curve shows the relationship between magnetic induction B and the magnetic field strength H . Using the hysteresis curve, various magnetic properties can be determined as shown in the same figure.

Of utmost importance is the material's saturation magnetization M_{sat} which refers to the maximum magnetization that can be achieved by the material. This represents a condition in which all of the magnetic dipoles within the material are aligned in the direction of the applied magnetic field. [43] As a consequence, further increase in magnetic field strength will not increase the magnetization.

The saturation point can be described through magnetic induction, B_{sat} as follows:

$$B_{sat} = \mu_0(H_c + M_{sat}) \quad (2.69)$$

Here, H_c refers to the material's coercivity which is the maximum magnetic field strength at zero magnetization. This corresponds to the amount of reverse magnetic field required to

demagnetize the material. [43]

How does the transformer's core saturate?

Under AC excitation, a sinusoidal voltage v_1 is applied on the primary winding where:

$$v_1(t) = \hat{v}_1 \cos \omega t \quad (2.70)$$

Assuming that the voltage drop across the resistance is negligible compared to the rate of change of the flux linkage will simplify the voltage equation to:

$$v_1 = e_1 = \frac{d\lambda_1}{dt} \quad (2.71)$$

Equation (2.71) shows a sinusoidal variation of the flux linkage.

$$\lambda_1(t) = \frac{\hat{v}_1}{\omega} \sin \omega t = \lambda_{1,max} \sin \omega t \quad (2.72)$$

Consequently the core flux and flux density must be sinusoidal.

$$\phi(t) = \phi_{max} \sin \omega t = A_c B_{max} \sin \omega t \quad (2.73)$$

Using equations (2.70) to (2.73), the induced voltage in the primary winding can be deduced as follows:

$$\begin{aligned} v_1(t) = e_1(t) &= \frac{d\lambda_1}{dt} \\ &= \omega \lambda_{1,max} \cos \omega t \\ &= \omega N \phi_{max} \cos \omega t = \omega N_1 A_c B_{max} \cos \omega t \\ &= E_{max} \cos \omega t \end{aligned} \quad (2.74)$$

where the maximum induced voltage E_{max} is defined as:

$$E_{max} = \omega N_1 A_c B_{max} \quad (2.75)$$

Consequently, the root-mean-square (rms) value of the induced voltage can be defined as follows:

$$E_{rms} = \frac{E_{max}}{\sqrt{2}} = \sqrt{2} \pi f N_1 A_c B_{max} \quad (2.76)$$

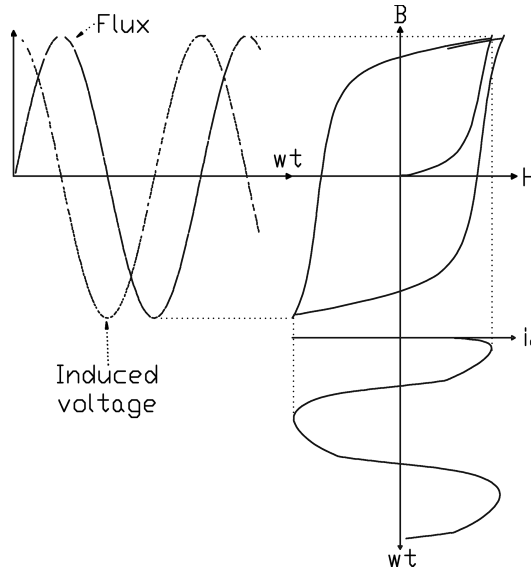


Figure 2.18: Relationship between exciting current, voltage, flux and B-H curve obtained via a Simulink simulation during the preliminary project work [8]

To produce and maintain the required sinusoidal flux density and induced voltage waveforms, a coil current referred to as excitation current i_e is required, as shown in **Figure 2.18**. Knowing that a current flowing through a coil with N windings produces a magnetomotive force (mmf), i_e can be expressed as:

$$i_e = \frac{1}{N} \oint H dl = \frac{l_c H_c}{N} \quad (2.77)$$

The non-linear magnetic properties of a transformer core results to varying core magnetic field strength H_c decided by the core material's hysteresis loop. Since i_e is proportional to H_c , the exciting current's waveform is of the same shape as the hysteresis loop; as shown in **Figure 2.18**.

The rms value of the excitation current can be defined as:

$$i_{e,rms} = \frac{l_c H_{c,rms}}{N} \quad (2.78)$$

By combining equations (2.76) and (2.77), the rms exciting volt-amperes required to excite the core can be expressed. [44]

$$E_{rms} i_{e,rms} = \sqrt{2} \pi f B_{max} H_{c,rms} A_c l_c \quad (2.79)$$

Since the saturation point is defined by B_{sat} , the saturation point is reached when $B_{max} \geq B_{sat}$. Arranging equation (2.79) to solve for B_{max} gives the saturation condition:

$$B_{max} = \frac{E_{rms} i_{e,rms}}{\sqrt{2} \pi f H_{c,rms} A_c l_c} \geq B_{sat} \quad (2.80)$$

Assuming $H_{c,rms}$ and $i_{e,rms}$ constant parameters pre-saturation, (2.80) can be expressed as:

$$B_{max} = K \frac{E_{rms}}{f} \geq B_{sat} \quad (2.81)$$

where K is a constant dependent on the core's material and dimensions.

Equation (2.81) shows that the magnetic flux density in the core is proportional to the quotient of the applied voltage and frequency (E_{rms}/f). Consequently, the flux in the core increases by either increasing the applied voltage or decreasing the frequency, and can easily reach the saturation flux. This condition is often referred to as over-fluxing.

Why is core saturation a problem?

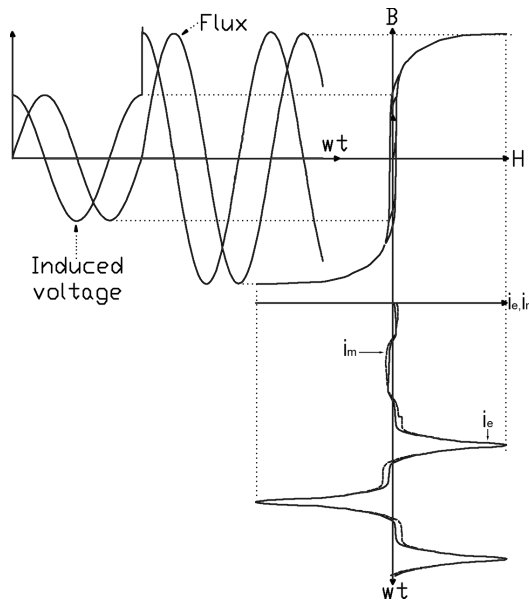


Figure 2.19: Relationship between excitation current, voltage, flux and B-H curve during saturation obtained via a Simulink simulation during the preliminary project work [8]

Figure 2.19 shows the current, voltage and flux waveforms during saturation. As can be implicitly seen in the figure, the differential permeability goes to zero at the top of the B-H curve due to saturation.

Since the excitation current is proportional to the magnetic field strength of the curve, it drastically increases as the core saturates. It can be seen that the magnetizing current is symmetrical and has the same waveform as the excitation current. Consequently, the magnetizing inductance becomes small, and the windings are effectively shorted out. Analytically, this would mean that the transformer experiences a huge amount of leakage

flux. This in turn induces huge amount of eddy currents in the core and nearby structural components, which causes over heating within a short amount of time and may cause severe damage to the transformer.

Additionally, the flux and the voltage waveforms shows that the voltage induced in the secondary windings has distortions, which can typically cause disturbances on the underlying network.

How to avoid transformer core saturation?

In order to avoid the saturation of the transformer's core, it should be correctly designed to withstand the maximum flux density so that $B_{max} < B_{sat}$. Consequently, the required condition to avoid saturation would be as follows:

$$\frac{E_{rms} i_{e,rms}}{\sqrt{2} \pi f H_{c,rms} A_c l_c} < B_{sat} \quad (2.82)$$

Modelling core saturation

The non-linearity of the transformer's core can be incorporated into the simulation by using various computational methods and engineering models which have been developed for decades [45]. A good example would be the, Simulink SimPowerSystems "Saturable Transformer" block model which uses a static model of hysteresis which defines the relation between the flux and the magnetization current that is equal to the total excitation current measured in DC [46].

2.11 Cable modelling

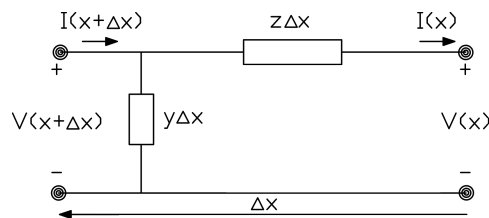


Figure 2.20: Long line with distributed parameters

In order to provide a more accurate solution for long transmission lines, the exact effect of distributed parameters must be considered as illustrated in **Figure 2.20**. Starting from the load, the receiving end of the line is located at $x = 0$. Consequently, the sending end of the line is at $x = l$ where l is the line's length. Δx refers to the incremental length of the line. Additionally, z and y are the cable's series impedance and shunt admittance respectively which are calculated as follows:

$$z = r + j\omega L \quad (2.83)$$

$$y = g + j\omega C \quad (2.84)$$

Performing Kirchhoff's Current Law at the sending node gives:

$$\begin{aligned} I(x + \Delta x) &= I(x) + y\Delta x V(x + \Delta x) \\ &\Downarrow \\ \frac{I(x + \Delta x) - I(x)}{\Delta x} &= yV(x + \Delta x) \Rightarrow \frac{dI}{dx} = yV \end{aligned} \quad (2.85)$$

Performing Kirchhoff's Voltage Law to the loop comprising the sending end node and receiving end node gives:

$$\begin{aligned} V(x + \Delta x) &= V(x) + z\Delta x I(x) \\ &\Downarrow \\ \frac{V(x + \Delta x) - V(x)}{\Delta x} &= zI(x) \Rightarrow \frac{dV}{dx} = zI \end{aligned} \quad (2.86)$$

Combining the differential equations (2.85) and (2.86) gives:

$$\begin{aligned} \frac{d^2 V(x)}{dx^2} &= z \frac{dI(x)}{dx} \\ &= zyV(x) = \gamma^2 V(x) \end{aligned} \quad (2.87)$$

Here, γ is known as the propagation constant and is defined as:

$$\gamma = \sqrt{zy} \quad (2.88)$$

Solving the differential equation (2.87) gives the following voltage and current equations:

$$V(x) = k_1 e^{\gamma x} + k_2 e^{-\gamma x} \quad (2.89)$$

$$\begin{aligned} I(x) &= \frac{1}{z} \frac{dV(x)}{dx} = \frac{\gamma}{z} (k_1 e^{\gamma x} - k_2 e^{-\gamma x}) \\ &= \frac{1}{Z_c} (k_1 e^{\gamma x} - k_2 e^{-\gamma x}) \end{aligned} \quad (2.90)$$

Here, Z_c is known as the characteristic impedance and is defined as:

$$Z_c = \sqrt{\frac{z}{y}} \quad (2.91)$$

Solving for the constants, given that $V(x = 0) = V_R$ and $I(x = 0) = I_R$, where V_R and I_R are the receiving end voltage and current respectively, gives the following voltage and current equations at any point x from the receiving end:

$$V(x) = V_R \cosh(\gamma x) + Z_c I_R \sinh(\gamma x) \quad (2.92)$$

$$I(x) = I_R \cosh(\gamma x) + \frac{V_R}{Z_C} \sinh(\gamma x) \quad (2.93)$$

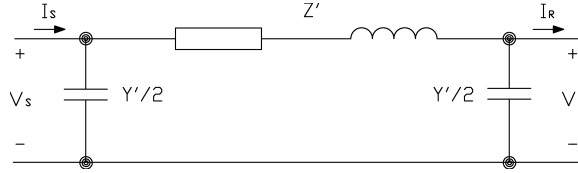


Figure 2.21: Equivalent π model for long length line

Setting $x = l$ and making use of the identity:

$$\tanh \frac{\gamma l}{2} = \frac{\cosh(\gamma l) - 1}{\sinh(\gamma l)} \quad (2.94)$$

gives the equivalent π model is illustrated in **Figure 2.21** where

$$Z' = Z_c \sinh(\gamma l) = Z \frac{\sinh(\gamma l)}{\gamma l} \quad (2.95)$$

$$S \frac{Y'}{2} = \frac{1}{Z_c} \tanh \frac{\gamma l}{2} = \frac{Y}{2} \frac{\tanh(\gamma l/2)}{\gamma l/2} \quad (2.96)$$

Study case and simulation description

This chapter describes the electrical system of the study case, the simulation, and the corresponding Simulink model of the system components.

3.1 General

The electrical power supply system features torque and speed control of the subsea PMSM. It consists of the following system components:

- Three-phase supply system
- VFD
- Step-up transformer
- Umbilical cable
- Step-down transformer
- High Voltage Electrical Flying Leads (HV EFL)
- PMSM

Since the HV EFLs are significantly shorter than umbilical cable, they are neglected in this study.

3.1.1 Study case description

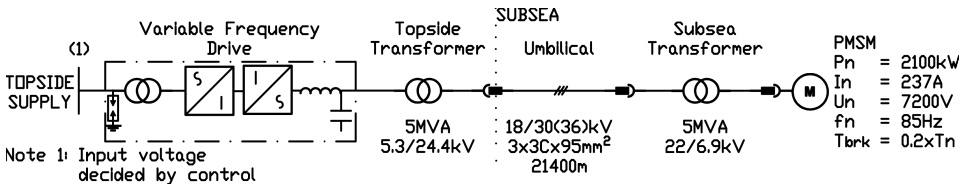


Figure 3.1: Electrical system topology - Base case

A study case comprising of a PMSM operated by a VFD without position feedback has been defined as illustrated in **Figure 3.1**. As shown, the PMSM is operated by a VFD. The transmission system comprises of a topside transformer, a long cable and a subsea transformer. The key parameters of the components are also shown in the figure. All component parameters have been provided by OneSubsea AS. Detailed component parameters are shown further down in this chapter.

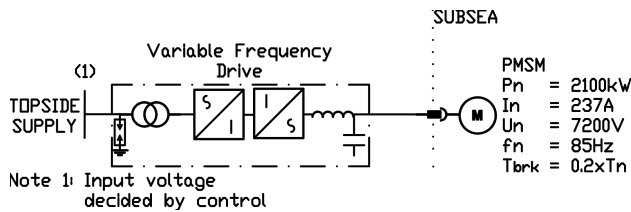


Figure 3.2: Electrical system topology - Test case

In order to test the controller, a similar case without the transmission system components has been established; as shown in **Figure 3.2**. This case will be referred to as the **Test case**, while the previously mentioned case will be referred to as the **Base case**.

Note the huge difference between the components parameters used for this study and the preliminary project, shown in section 1.2.

3.1.2 Simulation description

As described in section 2.3, the simulations are performed using Simulink, Simscape and SimPowerSystems softwares.

New component models and control systems are developed using either the MATLAB based Simscape language or the built-in Simulink blocks. Component blocks and subsystems made using the Simscape language will be documented through the used codes. Subsystems made using the Simulink blocks will be documented through screenshots of the subsystem.

The simulation models of the electrical system is divided into three subsystems as illustrated in **Figure 3.3**.

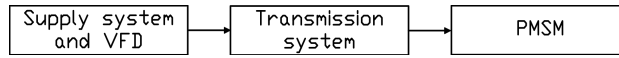


Figure 3.3: Simulation subsystems

3.2 Supply system and VFD

The supply system and VFD are modelled as one subsystem, which acts as a voltage source with a variable V/Hz profile. The voltage output depends on the selected control method.

Both sensorless scalar and vector control schemes are implemented for this study.

Detailed information about the controller subsystem is given in chapters 4 and 5.

3.3 PMSM

Data

The provided PMSM data has a terminal voltage of 7200 V and a rated current of 237 A. Detailed PMSM parameters are shown in **Table 3.1**.

V_n	7200 V	I_n	237 A
P_n	2100 kW	J	5.7 kgm^2
Pole pair	1	n_n	5100 rpm
R_s	0.165Ω	λ_m	10.90 Vs
L_d	0.0256 H	L_q	0.0256 H

Table 3.1: PMSM parameters [47]

The PMSM is to drive a load with a breakaway torque of $0.2 \times T_n$ and a load torque which is a quadratic function of speed.

Simulation model

Two PMSM models have been developed in Simulink using Simscape language. The resulting blocks are shown in **Figure 3.4**.

Model 1.0 implements a PMSM without damper windings while model 2.1 implements a PMSM with damper windings. These models are based on the derived equations in sections 2.4.2 and 2.4.3. The Simscape codes used, and more detailed information about these models can be found in appendix A.1.

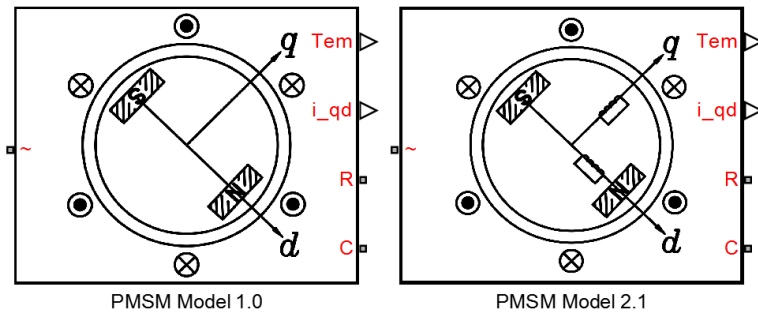


Figure 3.4: User-made PMSM blocks

The R and C connection ports on the motor models are the mechanical conserving ports. This means that they are to be connected to the subsystem simulating the mechanical characteristics of the motor, as shown in **Figure 3.5**.

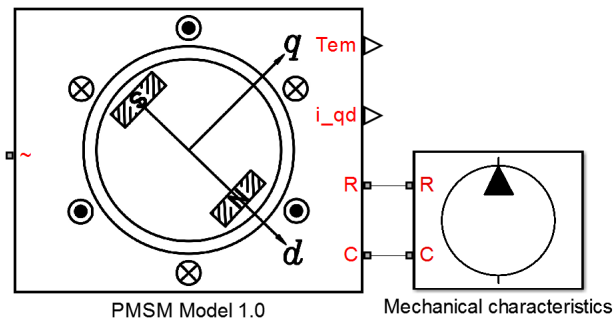


Figure 3.5: Mechanical connection between the PMSM and the mechanical characteristics block

As discussed in section 2.8, two characteristics of the load are required to be modelled: its torque requirement, and its rotational friction torque. This is realized in Simulink as illustrated in **Figure 3.6**.

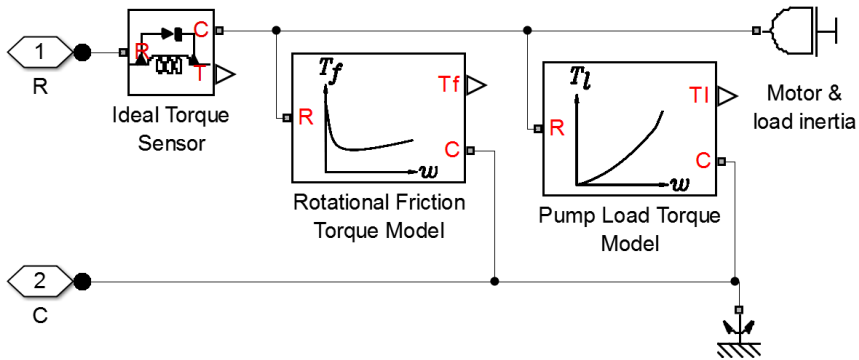


Figure 3.6: Inside the mechanical characteristics block, showing the user-made rotational friction and load torque blocks

The load torque requirement expressed in equation (2.60) can easily be simulated. However, the rotational friction torque described by equation (2.61) creates computational problems due to it being discontinuous at $w_m = 0$. This discontinuity can be eliminated by introducing a small transition period during zero speed, as illustrated in **Figure 3.7**.

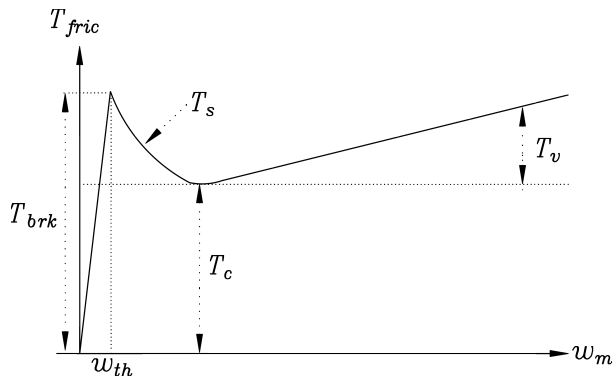


Figure 3.7: Rotational friction torque

During this transition period, the friction torque is assumed to be linearly proportional to velocity, with the proportionality coefficient T_{brk}/w_{th} where w_{th} is the velocity threshold. It has been proven experimentally that the velocity threshold in the range between 10^{-3} and 10^{-5} rad/s is a good compromise between the accuracy and computational robustness and effectiveness. Notice that friction torque computed with this approximation does not actually stop relative motion when an acting torque drops below breakaway friction level. The bodies will creep relative to each other at a very small velocity proportional to the acting torque. [42, 48]

The rotational friction torque can then be expressed as follows: [42, 48]

$$T_{fric} = \begin{cases} (T_c + (T_{brk} - T_c))e^{-c_v|w_m|}sign(w_m) + fw_m, & |w_m| \geq w_{th} \\ \frac{w_m}{w_{th}}(T_c + (T_{brk} - T_c))e^{-c_v w_{th}} + fw_{th}, & \text{otherwise} \end{cases} \quad (3.1)$$

where

T_{fric}	Rotational friction torque
T_c	Coulomb friction torque
T_{brk}	Breakaway friction torque
c_v	coefficient
w_m	rotor angular mechanical speed
w_{th}	velocity threshold
f	Viscous friction coefficient

The Simscape codes used, and more detailed information about these models can be found in appendix A.2.

3.4 Transmission system

The transmission system can be divided into three subsystems: the two transformers and the cable. More detailed information about the corresponding models can be found in appendix A.3.

3.4.1 Transformers

Data

The provided transformer parameters are shown in **Tables 3.2 and 3.3**.

Pn	5 MVA		
V1 (Vrms)	5.3 kV	V2 (Vrms)	24.4 kV
R1	13.76 mΩ	L1	0.41 mH
R2	291.73 mΩ	L2	8.68 mH
Rm	96.80 kΩ	Lm	43.40 H

Table 3.2: Topside step-up transformer parameters [47]

Pn	5 MVA		
V1 (Vrms)	22 kV	V2 (Vrms)	6.9 kV
R1	242.0 $m\Omega$	L1	10.25 mH
R2	23.8 $m\Omega$	L2	1.0 mH
Rm	2.39 $k\Omega$	Lm	750 mH

Table 3.3: Subsea step-down transformer parameters [47]

Simulation model

To reduce computational complexity of the simulation, a three-phase two-winding transformer model comprising of three single phase cores is chosen. The transformer's primary and secondary windings are chosen to be star connected.

The linear model based on equations (2.62) - (2.68) can be implemented in Simulink by using the SimPowerSystem third generation blocks "Ideal Transformer" and "RLC".

The non-linearity of the transformer's core can be incorporated into the simulation by using various computational methods and engineering models which have been developed for decades [45]. In Simulink SimPowerSystems, the "Wye-Wye Transformer" block model (Third generation) uses a static model of hysteresis which defines the relation between the flux and the magnetization current that is equal to the total excitation current measured in Direct Current (DC) [46].

3.4.2 Cable

Data

The provided cable parameters are shown in **Table 3.4 and 3.3**.

Resistance	0.21 Ω/km
Inductance	0.776 mH/km
Capacitance	0.14 $\mu F/km$
Length	21400 m

Table 3.4: Cable parameters [47]

To reduce computational complexity of the simulation, the HV EFL can be neglected since its length is comparably shorter than the umbilical cable.

Simulation model

A three-phase transmission line model using the distributed parameters line model described in section 2.11 already exists in Simulink SimPowerSystems as a third generation block named "Transmission Line". This model is thus used in the simulations.

Scalar controller

This chapter describes the mathematical equations used to model the V/Hz controller in order to accelerate the PMSM from stand-still to synchronous speed, and the simulation model that is used in Simulink.

4.1 Control description

The speed of a PMSM can be controlled by varying the frequency of the applied AC excitation.

Assuming that the stator flux linkage is constant and the stator resistance is negligible, the stator flux linkage can be expressed using the derived voltage equation (2.20) as follows:

$$\hat{v}_{abc} \approx w_r \hat{\lambda}_{abc} \Leftrightarrow \hat{\lambda}_{abc} \approx \frac{\hat{v}_{abc}}{w_r} = \frac{\hat{v}_{abc}}{2\pi f} \quad (4.1)$$

where \hat{v}_{abc} and $\hat{\lambda}_{abc}$ are the magnitudes of the voltage and the stator flux linkage space vectors respectively.

Equation (4.1) shows that the stator flux is proportional to the quotient of the applied voltage and frequency (V/f). Therefore, decreasing the electrical frequency during the start-up procedure will cause the stator flux linkage to increase above its nominal value. Consequently, the motor enters over-excitation which leads to rise in magnetizing current, causing huge hysteresis and eddy current losses, and risk of saturation due to the low applied frequency during start-up. Therefore, in order to avoid over-excitation of the motor, the stator flux must be kept constant at its rated value which means that the applied voltage must be varied proportional to the applied frequency.

This control method is referred to as scalar V/Hz control and can be implemented with either an open-loop or a closed loop control scheme. By using the term "closed loop", this would mean that the controller receives and uses some kind of feedback.

4.2 General controller components

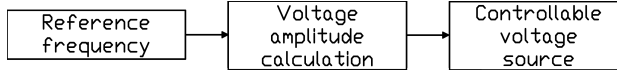


Figure 4.1: Scalar controller subsystem

The general scalar controller subsystem is illustrated in **Figure 4.1**, and shows the hierarchical structure. As shown, the controller subsystem is split up as follows:

- Reference frequency
- Voltage amplitude calculations
- Controllable (V and f) AC voltage source

These components will be discussed further down in this section.

4.2.1 Reference frequency

The reference frequency f^* dictates the speed of the PMSM's stator magnetic field. The rate of change of the reference frequency determines the acceleration of the PMSM and if the rotor is able to keep up with the stator magnetic field. Consequently during the PMSM's start-up procedure, it is desirable to find the maximum rate of change of the reference frequency that will allow the PMSM the maximum acceleration from stand-still without risking loss of synchronism.

4.2.2 Voltage amplitude calculation

Since the d-axis reactance is proportional to the electrical frequency as shown in equation (2.53), the stator resistance cannot be neglected at low frequencies; as discussed in section 4.1. As a consequence, the applied voltage needs to compensate for the resistive voltage drop caused by the stator resistance through voltage boosting.

The suitable stator voltage amplitude can be calculated from the steady-state equivalent circuit. Since the magnitude of the total stator flux and the flux produced by the permanent magnets are the same, the required voltage magnitude can be expressed as:

$$\begin{aligned}
 V_s &= \hat{v}_{abc} = r_s \hat{i}_{abc} + w_r \hat{\lambda}_{abc} \\
 &= r_s I_s + w_r \lambda_m
 \end{aligned}
 \tag{4.2}$$

Here, V_s and I_s are the steady state magnitudes of the voltage vector \hat{v}_{abc} and the current vector \hat{i}_{abc} .

This stator voltage amplitude calculation can be implemented through different methods with varying accuracy as follows:

- Constant voltage boosting through rated stator current
- Partial and delayed voltage boosting through rated stator current
- Voltage boosting through measured stator current

These control methods will be discussed further down in the chapter.

4.2.3 Controllable voltage source

Normally, the reference signals \hat{v}_{abc}^* and f^* are used as input signals for PWM which determines the output voltage of the VFD. In order to simplify the system modelling, it is assumed that the output voltage of the VFD is perfectly filtered and contains no harmonics. Consequently, the output voltage of controller can be expressed as follows:

$$\begin{aligned}v_a(t) &= V_s \cos(\theta_r^*) \\v_b(t) &= V_s \cos(\theta_r^* - 2\pi/3) \\v_c(t) &= V_s \cos(\theta_r^* + 2\pi/3)\end{aligned}\tag{4.3}$$

However, it must be noted that the output voltage of the VFD are not perfect at low speed in reality, with two transformers and a long cable in the system.

4.3 Constant voltage boosting through rated stator current

This section describes the control scheme using constant voltage boosting through rated stator current and the corresponding simulation model that is used in Simulink.

4.3.1 Control scheme

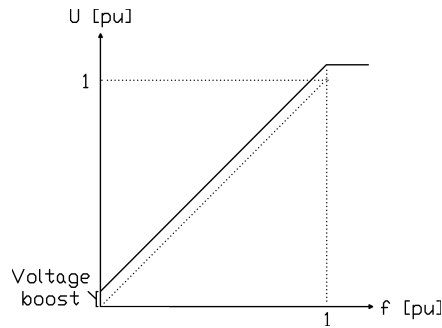


Figure 4.2: Constant voltage boosting through rated stator current

Inputting the peak value of the rated stator current to equation (4.2) gives the following equation:

$$V_s = r_s I_{s,rated} + w_r \lambda_m \quad (4.4)$$

This voltage amplitude calculation method can be illustrated as **Figure 4.2**.

This method assumes that the peak value of the stator current is constant and equal to the rated value throughout the whole frequency range.

Transmission system voltage drop compensation

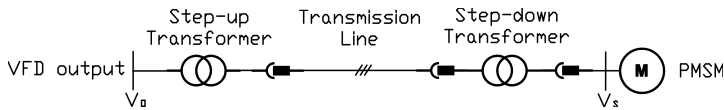


Figure 4.3: Overview of the transmission system components

Additionally, the voltage amplitude calculation needs to take into account the voltage drop of transmission system components shown in **Figure 4.3**. However, due to the lack of measurements, calculating the transmission voltage drop accurately is not possible. Consequently, it can be assumed that the transmission system's reactance is negligible

during start-up due to the low electrical frequency, the approximate equivalent circuit of the above figure can be illustrated as follows:

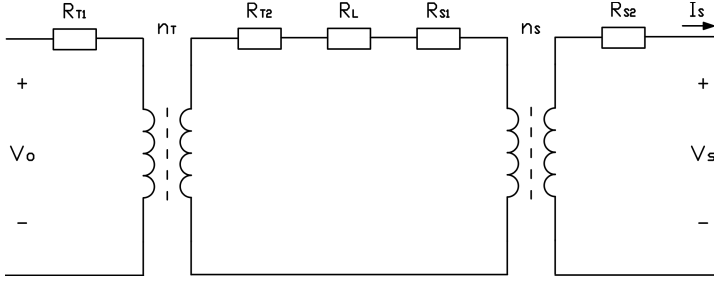


Figure 4.4: Equivalent circuit of the transmission system

Here, V_o and V_s corresponds to the required converter output voltage and PMSM voltage respectively. R_{T1} and R_{T2} are the primary and secondary winding resistances of the step-up transformer. R_{S1} and R_{S2} are the primary and secondary winding resistances of the step-down transformer. R_L is the transmission line resistance, and n_T and n_S are the turns ratio of the step-up and the step-down transformers respectively.

Since the resistances of **Figure 4.3** are in series with the stator resistance, the equivalent resistance of the transmission system can be integrated to the PMSM equivalent circuit. This allows the usage of the same voltage amplitude calculation equations derived in the previous section.

The total system resistance referred to the motor side can be obtained as follows:

$$R_{tot} = r_s + R_{S2} + \frac{R_{S1} + R_L + R_{T2}}{n_S^2} + \frac{R_{T1}}{n_S^2 n_T^2} \quad (4.5)$$

The proposed resulting voltage amplitude equation referred to the drive side will be as follows:

$$V_o = (R_{tot} I_{s, rated} + w_r \lambda_m) n_T n_S \quad (4.6)$$

4.3.2 Simulation model

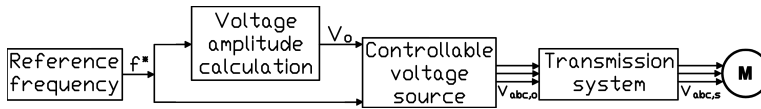


Figure 4.5: Open-loop scalar controller overview

A Simulink model of the controller based on equations derived in this section has been established.

The complete open-loop controller subsystem is illustrated in **Figure 4.5**, and shows the hierarchical structure. As shown, the open-loop controller subsystem is split up into the blocks previously discussed in this chapter.

The controller subsystem and its blocks implemented in Simulink are discussed in detail in Appendix A.5.

4.4 Partial and delayed voltage boosting through rated stator current

This section describes the control scheme using partial and delayed voltage boosting through rated stator current and the corresponding simulation model that is used in Simulink.

4.4.1 Control scheme

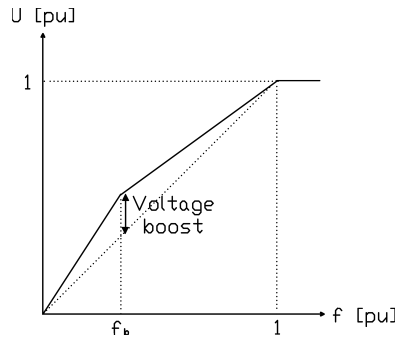


Figure 4.6: Partial and delayed voltage boosting through rated stator current

Since the peak stator current is not constant throughout the whole frequency range, and the resistive voltage drop is negligible at high frequencies, a delayed and partial voltage boosting can be implemented as shown in **Figure 4.6**. In the figure, the voltage boosting frequency delay is denoted with f_b (border frequency). [16]

The voltage amplitude when $f < f_b$ can be calculated as follows:

$$\begin{aligned} V_s &= (r_s I_{s,rated} + w_{rb} \lambda_m) \frac{w_r \lambda_m}{w_{rb} \lambda_m} \\ &= F_b w_r \lambda_m \end{aligned} \quad (4.7)$$

where F_b and w_{rb} are the voltage boosting constant and border frequency respectively. w_{rb} can be defined based on when the stator resistive voltage drop can be assumed to be neglected. This can be mathematically expressed using the ratio between the back emf and the stator voltage drop, K_b as follows:

$$K_b = \frac{w_{rb}\lambda_m}{r_s I_{s,rated}} \Leftrightarrow w_{rb} = K_b \frac{r_s I_{s,rated}}{\lambda_m} \quad (4.8)$$

Since the stator resistive voltage drop is negligible during high frequency, the voltage amplitude when $f > f_b$ can be expressed as follows:

$$\begin{aligned} V_s &= \frac{V_{s,rated} - V_s|_{f=f_b}}{f_{rated} - f_b} f \\ &= F_{b2} f \end{aligned} \quad (4.9)$$

where a constant called F_{b2} is introduced in order to simplify calculation.

Transmission system voltage drop compensation

Since measurements are still lacking as the previous control scheme, negligible transmission system's reactance is still assumed. Consequently, the same total resistance can be obtained as shown in equation (4.5). Inputting the total resistance to equation (4.7) gives the proposed voltage amplitude equation when $f < f_b$:

$$\begin{aligned} V_s &= (R_{tot} I_{s,rated} + w_{rb}\lambda_m) \frac{w_r\lambda_m}{w_{rb}\lambda_m} \\ &= F_b w_r \lambda_m \end{aligned} \quad (4.10)$$

4.4.2 Simulation model

A Simulink model of the controller based on equations derived in this section has been established.

Since the control scheme is open-loop in nature, the same controller overview shown in **Figure 4.5** can be used.

The controller subsystem and its blocks implemented in Simulink are discussed in detail in Appendix A.5.

4.5 Voltage boosting through measured stator current

This section describes the control scheme using voltage boosting through measured stator current and the corresponding simulation model that is used in Simulink.

4.5.1 Control scheme

The stator voltage drop can be compensated accurately using current measurements as proposed by Perera et al. [49] This allows constant torque throughout the whole frequency range. Consequently, this would mean that measured current used as a feedback is required.

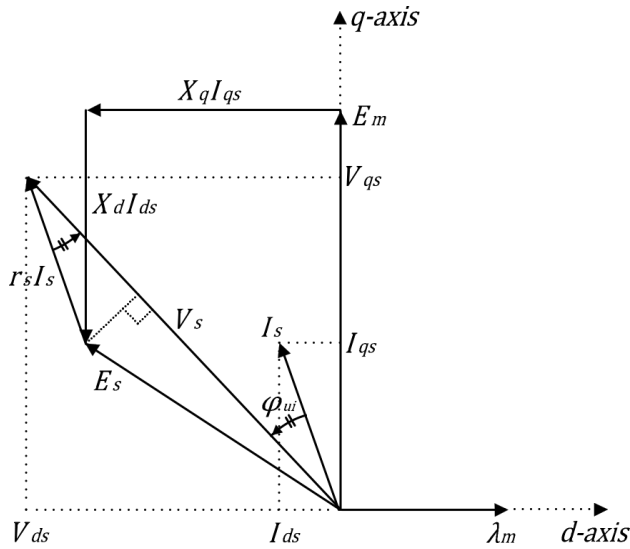


Figure 4.7: Steady-state vector diagram of a PMSM in rotor dq reference frame

The steady-state vector diagram shown in **Figure 4.7** shows that the steady state voltage magnitude can be expressed as follows:

$$\begin{aligned} V_s &= r_s I_s \cos \varphi_{ui} + \sqrt{E_m^2 - (r_s I_s \sin \varphi_{ui})^2} \\ &= r_s I_s \cos \varphi_{ui} + \sqrt{E_m^2 + (r_s I_s \cos \varphi_{ui})^2 - (r_s I_s)^2} \end{aligned} \quad (4.11)$$

where φ_{ui} is the angle between the voltage and current vector and E_m is the back-EMF produced by the permanent magnet.

The current vector I_s and the term $I_s \cos \varphi_{ui}$ can be obtained through measured phase currents as follows:

$$\begin{aligned}
 i_s &= \sqrt{i_{ds}^2 + i_{qs}^2} \\
 &= \sqrt{\left[\frac{1}{3}(2i_a - i_b - i_c)\right]^2 + \left[\frac{1}{\sqrt{3}}(i_b - i_c)\right]^2}
 \end{aligned} \tag{4.12}$$

$$i_s \cos \varphi_{ui} = \frac{2}{3}[i_a \cos \theta_r + i_b \cos(\theta_r - 120^\circ) + i_c \cos(\theta_r + 120^\circ)] \tag{4.13}$$

Transmission system voltage drop compensation

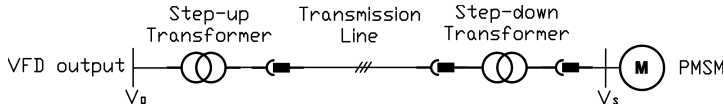


Figure 4.8: Overview of the transmission system components

As previously done, the voltage amplitude calculation needs to take into account the voltage drop of transmission system components shown in **Figure 4.8**. Since current measurements are available, calculating the transmission voltage drop accurately is possible.

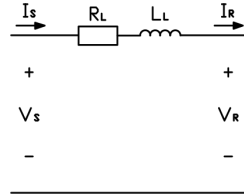


Figure 4.9: Short line model

To reduce computational complexity, the transmission line capacitance can be ignored. This is justifiable as it will not give much error if the lines are less than about 80 km, or if the voltage is not over 69 kV [50]. Since the cable length used in the study case is less than 80 km, the short line model illustrated in **Figure 4.9** is adequate. The subscripts *S* and *R* corresponds to whether the per phase voltage and current is located at the sending end and the receiving end respectively.

Consequently, the equivalent circuit of the transmission system shown in **Figure 4.8** can be illustrated as follows:

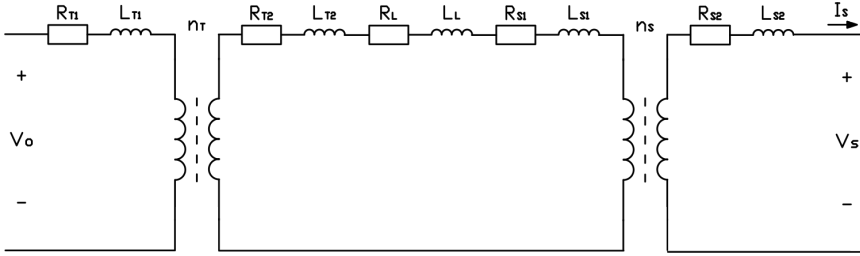


Figure 4.10: Equivalent circuit of the transmission system

Here, V_o and V_s corresponds to the required converter output voltage and PMSM voltage respectively. R and L corresponds to the resistances and the inductances of the components respectively. The subscripts $T1$ and $T2$ refers to the primary and secondary windings of the step-up transformer, while $S1$ and $S2$ refers to the primary and secondary windings of the step-down transformer. The subscript L refers to the transmission line. n_T and n_S are the turns ratio of the step-up and the step-down transformers respectively.

Since the resistances of **Figure 4.10** are in series with the stator resistance, the equivalent resistance of the transmission system can be integrated to the PMSM equivalent circuit as previously done. Consequently, the equivalent steady-state vector diagram of the system can be shown as in **Figure 4.11**. Additional points have been placed in the figure for equation derivations.

The total system resistance and inductance referred to the motor side can be obtained as follows:

$$R_{tot} = r_s + R_{S2} + \frac{R_{S1} + R_L + R_{T2}}{n_S^2} + \frac{R_{T1}}{n_S^2 n_T^2} \quad (4.14)$$

$$L_{tot} = L_{S2} + \frac{L_{S1} + L_L + L_{T2}}{n_S^2} + \frac{L_{T1}}{n_S^2 n_T^2} \quad (4.15)$$

As seen in **Figure 4.11**, the steady-state amplitude of the voltage vector V_o referred to the motor side can be obtained as:

$$V_o = \overline{OA} + \overline{AD} + \overline{DE} \quad (4.16)$$

Lines AD and DE can easily be found as follows:

$$\overline{AD} = X_{tot} I_s \sin \varphi_{ui} \quad (4.17)$$

$$\overline{DE} = R_{tot} I_s \cos \varphi_{ui} \quad (4.18)$$

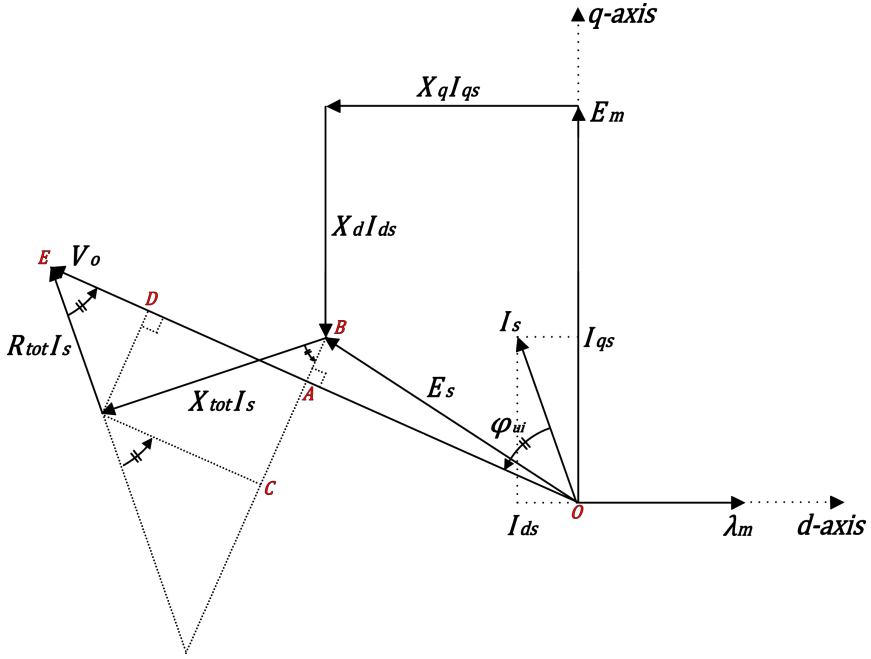


Figure 4.11: Steady-state vector diagram of the electrical system

Line OA can be obtained via Pythagorean theorem as follows:

$$\begin{aligned}
 \overline{OA} &= \sqrt{\overline{OB}^2 - \overline{AB}^2} \\
 &= \sqrt{E_s^2 - (\overline{BC} - \overline{AC})^2} \\
 &= \sqrt{E_s^2 - (X_{tot} I_s \cos \varphi_{ui} - R_{tot} I_s \sin \varphi_{ui})^2}
 \end{aligned} \tag{4.19}$$

The proposed resulting voltage amplitude equation referred to the drive side will be as follows:

$$\begin{aligned}
 V_o &= [\sqrt{E_s^2 - (X_{tot} I_s \cos \varphi_{ui} - R_{tot} I_s \sin \varphi_{ui})^2} + \dots \\
 &\quad X_{tot} I_s \sin \varphi_{ui} + R_{tot} I_s \cos \varphi_{ui}] n_T n_S
 \end{aligned} \tag{4.20}$$

Dynamic low-pass filter

Additionally, in order to filter out high frequency ripples in the calculated currents, a low pass filter is required. However, due to the variable frequency input, the filter parameters needs to change as a function of the frequency.

A second-order low-pass filter has the following transfer function:

$$H(s) = \frac{Y(s)}{U(s)} = \frac{\omega_n^2}{s^2 + 2\zeta\omega_n s + \omega_n^2} \quad (4.21)$$

Solving for the output $Y(s)$ gives:

$$Y(s) = \omega_n^2 U(s) \frac{1}{s^2} - 2\omega_n \zeta Y(s) \frac{1}{s} - \omega_n^2 Y(s) \frac{1}{s^2} \quad (4.22)$$

Equation (4.22) can be easily implemented in Simulink with $Y(s)$ as a function of the natural frequency ω_n which is equals to the reference frequency.

To be in the conservative side, the damping ratio ζ is chosen to be 0.707 which gives a 0.707 magnitude at the natural frequency, as shown in **Figure 4.12**.

A better filter such as the butterworth filter can be implemented as well, which will make it possible to get as flat a frequency response as possible. However, this will increase computational complexity due to the varying frequency.

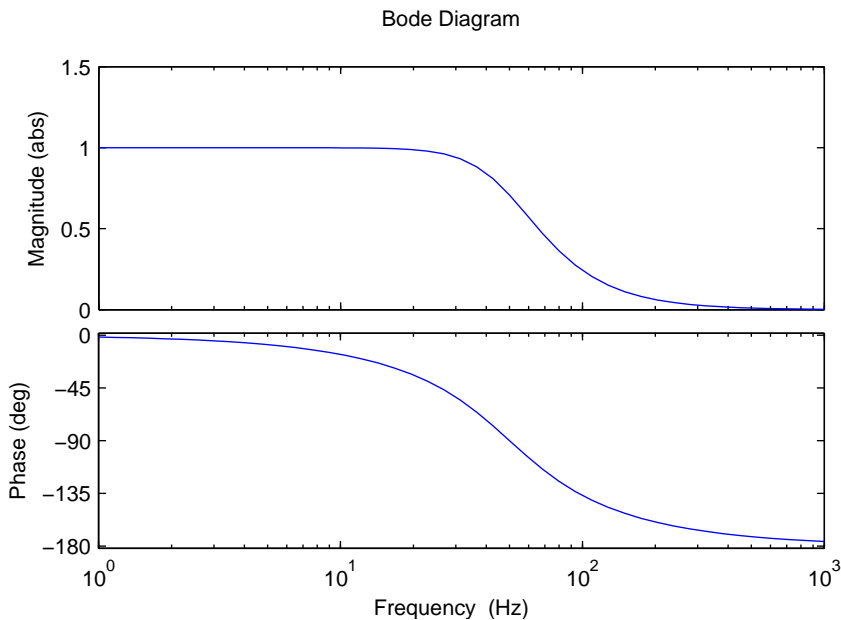


Figure 4.12: Low pass filter response ($\omega_n = 50$ Hz, $\zeta = 0.707$)

4.5.2 Simulation model

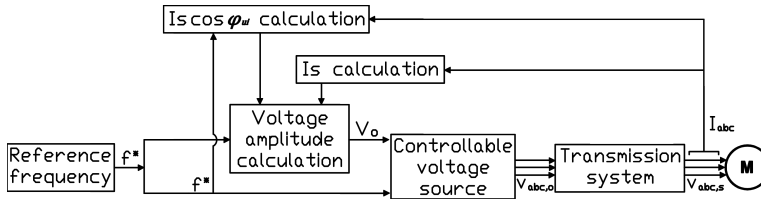


Figure 4.13: Closed-loop scalar controller overview

A Simulink model of the controller based on equations derived in this section has been established.

The complete closed-loop controller subsystem is illustrated in **Figure 4.13**, and shows the hierarchical structure. As shown, the closed-loop controller subsystem is split up into the blocks previously discussed in this chapter.

The controller subsystem and its blocks implemented in Simulink are discussed in detail in Appendix A.5.

4.6 Stabilization loop for PMSMs without damper windings

For PMSMs without an induction motor squirrel cage windings, the lack of asynchronous torque production does not guarantee stable operation, and synchronization of the rotor with the excitation frequency, as discussed in section 2.5.

To stabilize the system for the whole applied frequency range, additional damping to the rotor poles is required. This can be achieved by a proper modulation of the frequency of the machine. [49]

4.6.1 Implementation

As shown by Perera et al. [49], damping can be added to the system by modulating the applied frequency proportional to the perturbations in the input power of the machine, as follows:

$$\Delta w_e = -k_p \Delta p_e \quad (4.23)$$

where Δw_e , k_p and Δp_e are the frequency modulation signal, proportional gain, and input power perturbation respectively.

The input power to the machine can be calculated by using the calculated current given by equation (4.13) and the calculated voltage reference, as follows:

$$p_e = \frac{3}{2} v_s^* i_s \cos \varphi_{ui} \quad (4.24)$$

The input power perturbation can then be extracted by using a high pass filter on the calculated input power, as shown in **Figure 4.14**.

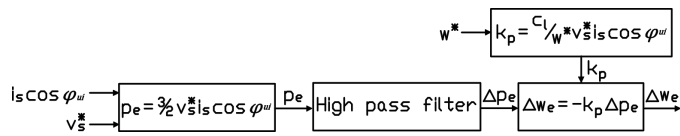


Figure 4.14: Frequency modulation signal calculation

Dynamic high-pass filter

Due to the variable frequency input, the high pass filter parameters needs to change as a function of the frequency.

A second-order high-pass filter has the following transfer function:

$$H(s) = \frac{Y(s)}{U(s)} = \frac{s^2}{s^2 + 2\zeta\omega_n s + \omega_n^2} \quad (4.25)$$

Solving for the output $Y(s)$ gives:

$$Y(s) = U(s) - 2\omega_n \zeta Y(s) \frac{1}{s} - \omega_n^2 Y(s) \frac{1}{s^2} \quad (4.26)$$

Equation (4.26) can be easily implemented in Simulink with $Y(s)$ as a function of the natural frequency ω_n which is equals to the reference frequency.

In order to be able to filter out fundamental signals, the damping ratio ζ is chosen to be 10 which gives a 0.05 magnitude at the natural frequency, as shown in **Figure 4.15**.

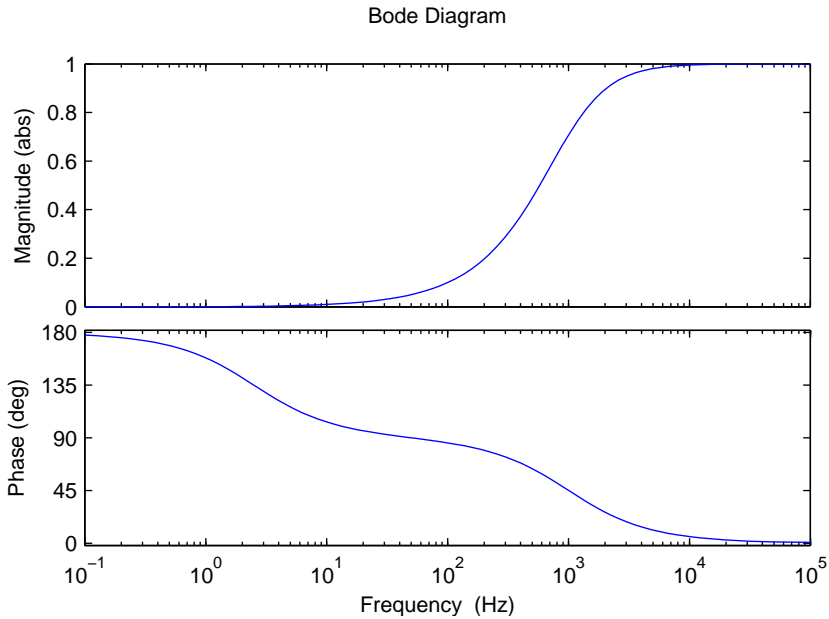


Figure 4.15: High pass filter response ($w_n = 50$ Hz, $\zeta = 10$)

4.6.2 Simulation model

A Simulink model of the controller based on equations derived in this section has been established.

The complete closed-loop controller subsystem is illustrated in **Figure 4.16**, and shows the hierarchical structure. As shown, the closed-loop controller subsystem is split up into the blocks previously discussed in this chapter.

The controller subsystem and its blocks implemented in Simulink are discussed in detail in Appendix A.5.

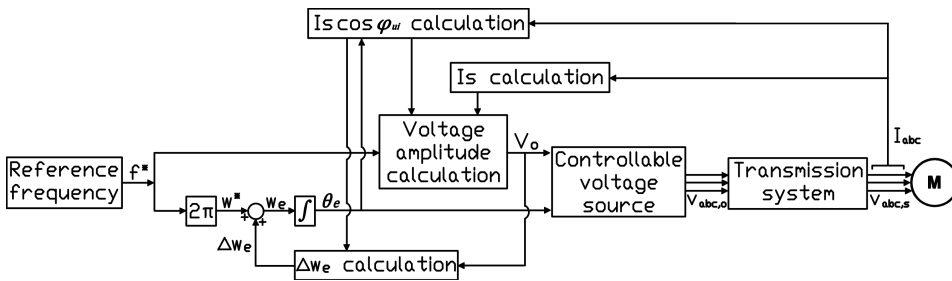


Figure 4.16: Closed-loop scalar controller with stabilization loop overview

Vector controller

Due to the advantages of FOC over DTC, FOC is used in this thesis. This chapter describes the mathematical equations used to model the field oriented controller, and the simulation model that is used in Simulink.

5.1 Control description

In this control scheme, the rotor field is controlled. In order to do this, the control scheme uses transformed variables in rotor reference frame that is turned at the system frequency, as described in section 2.4. Consequently, rotor position feedback is required by the controller.

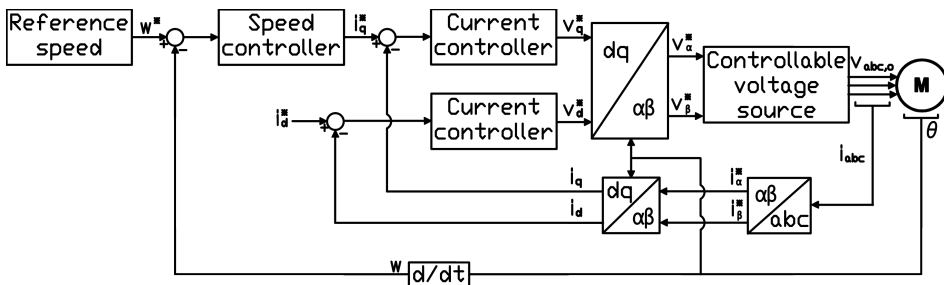


Figure 5.1: Field oriented controller overview

Figure 5.1 shows an overview of a controller using FOC.

As seen in the figure, the speed error, which is obtained by comparing reference and observed speed, is fed into a Proportional Integral (PI) controller. The PI speed controller output the torque command which generates the dq-axis reference currents. The dq currents are independently controlled, where the q-axis current is used to control the generated torque, while the d-axis current is used to control the magnetic state of the machine. The dq current errors, which are obtained by comparing reference and observed currents, are fed into their own PI controllers which then outputs the reference dq voltages.

For this thesis work, conventional control method has been selected where i_d^* is set to zero,

for simplicity. This is illustrated in **Figure 5.1**. However, Maximum Torque Per Amperes (MTPA) technique can be used in order to reduce the stator current and increase drive efficiency. [51]

Comments about the controller

The controller that will be described in this chapter does not include the transmission system components described in chapter 3 and is thus using the **Test case**, since the controller is an optional task as stated in the Scope of Work, section 1.4. The controller is thus used to test FOC and rotor estimation techniques.

5.2 Controller components

The controller overview illustrated in **Figure 5.1** shows that the controller subsystem can be split up as follows:

- Reference speed
- Current controller
- Speed controller
- Controllable (V and f) AC voltage source
- Transformation matrices

These components will be discussed further down in this section, except for the reference speed subsystem, as it is already indirectly defined ($w = 2\pi f$) in section 4.1.

5.2.1 Current controller

As seen from **Figure 5.1**, the current controller generates the dq-axis reference voltages.

Inputting the dq flux linkage equations (2.54) to the qd voltage equations (2.53), gives the following voltage equations:

$$v_q = \underbrace{r_s i_q + \frac{d}{dt} L_q i_q}_{v'_q} + \underbrace{(L_d i_d + \lambda'_m) w_r}_{v_{q,comp}} \quad (5.1)$$

$$v_d = \underbrace{r_s i_d + \frac{d}{dt} L_d i_d}_{v'_d} - \underbrace{L_q i_q w_r}_{v_{d,comp}} \quad (5.2)$$

In the q-axis voltage equation (5.1), only the first two terms are due to the q-axis current. The other term due to other variables can be considered as disturbances. Similarly, in equation (5.2), the last term can be considered as disturbances.

Therefore, these equation can be rewritten as:

$$v'_q = r_s i_q + \frac{d}{dt} L_q i_q \quad (5.3)$$

$$v'_d = r_s i_d + \frac{d}{dt} L_d i_d \quad (5.4)$$

where the compensation terms are:

$$v_{q,comp} = (L_d i_d + \lambda'_m) \omega_r \quad (5.5)$$

$$v_{d,comp} = -L_q i_q \omega_r \quad (5.6)$$

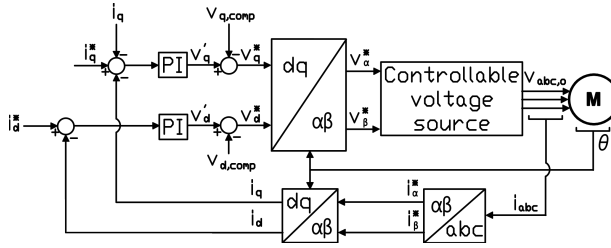


Figure 5.2: Vector control with applied voltages

To obtain v'_q and v'_d signals, PI controllers are used as illustrated in **Figure 5.2**, which has the well-known transfer function as follows:

$$\begin{aligned} PI(s) &= K_p + \frac{K_i}{s} \\ &= \frac{K_i}{s} \left(1 + \frac{K_p s}{K_i} \right) \end{aligned} \quad (5.7)$$

Controller design

The q-axis current reference are generated by the cascaded speed controller shown in **Figure 5.1**. Cascaded control requires the bandwidth to increase towards the inner loop. Hence, the current loop is required to have a faster response than the speed loop. This is achieved using the Modulus Optimum method which also fulfils Nyquist stability criterion without any problems. [52]

To compute the parameters of the PI controllers, it can be assumed that the compensation is perfect. The plant model can then be represented by the transfer functions below:

$$M_d(s) = \frac{i_d(s)}{v'_d(s)} = \frac{1}{r_s + L_d s} \quad (5.8)$$

$$M_q(s) = \frac{i_q(s)}{v'_q(s)} = \frac{1}{r_s + L_q s} \quad (5.9)$$

Hence each channel results in the block diagram shown in **Figure 5.3**, where a time delay T_v is added for computational delay as follows:

$$D(s) = \frac{1}{1 + T_v s} \quad (5.10)$$

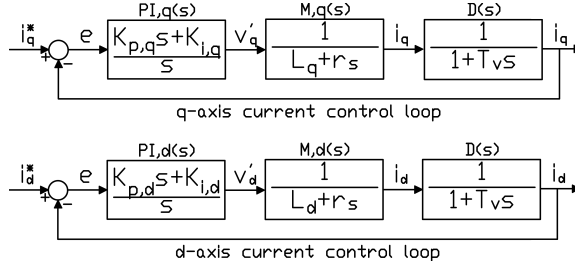


Figure 5.3: Current control loop

The open loop transfer function of the current control loop can be obtained as follows:

$$\begin{aligned} G_{OL,x}(s) &= PI_x(s)M_x(s)D_x(s) \\ &= \frac{K_{i,x}}{s} \left(1 + \frac{K_{p,x}s}{K_{i,x}}\right) \frac{1}{r_s + L_x s} \frac{1}{1 + T_v s} \\ &= K_{p,x} \frac{1 + T_{i,x}s}{T_{i,x}s} \frac{\frac{1}{r_s}}{1 + \frac{L_x}{r_s}s} \frac{1}{1 + T_v s} \\ &= \frac{K_{p,x}}{r_s} \frac{1 + T_{i,x}s}{T_{i,x}s} \frac{1}{1 + \frac{L_x}{r_s}s} \frac{1}{1 + T_v s} \end{aligned} \quad (5.11)$$

where x is the corresponding dq-axis variable, and $T_{i,x} = K_{p,x}/K_{i,x}$.

Applying zero-pole cancellation, where the zero in the PI controller is used to cancel the poles in the plant model transfer function gives the following:

$$G_{OL,x}(s) = \frac{K_{p,x}}{T_{i,x}r_s} \frac{1}{s(1 + T_v s)} \quad (5.12)$$

where

$$T_{i,x} = \frac{L_x}{r_s} \quad (5.13)$$

The closed loop transfer function of the current control loop can then be obtained as follows:

$$G_{CL,x}(s) = \frac{K_{p,x}}{T_v T_{i,x} r_s s^2 + T_{i,x} r_s s + K_{p,x}} \quad (5.14)$$

To make the transfer function of the closed control loop constant in a wide frequency range:

$$|G_{CL,x}(j\omega)| = 1 \quad (5.15)$$

$$|G_{CL,x}(jw)| = \frac{K_{p,x}}{T_v T_{i,x} r_s (jw)^2 + T_{i,x} r_s (jw) + K_{p,x}} \quad (5.16)$$

$$\begin{aligned} |G_{CL,x}(jw)|^2 &= \frac{K_{p,x}^2}{(K_{p,x} - w^2 T_v T_{i,x} r_s)^2 + T_{i,x}^2 r_s^2 w^2} \\ &= \frac{K_{p,x}^2}{K_{p,x}^2 + w^4 T_v^2 T_{i,x}^2 r_s^2 + w^2 (T_{i,x}^2 r_s^2 - 2T_v T_{i,x} r_s K_{p,x})} \end{aligned} \quad (5.17)$$

for small w : $w^4 T_v^2 T_{i,x}^2 r_s^2 \approx 0$

↓

$$\begin{aligned} |G_{CL,x}(jw)|^2 &= 1 \text{ for} \\ w^2 (T_{i,x}^2 r_s^2 - 2T_v r_s K_{p,x}) &= 0 \\ T_{i,x} &= \frac{2T_v K_{p,x}}{r_s} \end{aligned}$$

Solving for the PI controller gains gives the following:

$$K_{p,x} = \frac{L_x r_s}{2r_s T_v} = \frac{L_x}{2T_v} \quad (5.18)$$

$$K_{i,x} = \frac{K_{p,x}}{T_{i,x}} \quad (5.19)$$

For the motor used in this study, the computed controller gains are as follows:

$$\begin{cases} K_{p,d} = K_{p,q} = 160.85 \\ K_{i,d} = K_{i,q} = 1036.7 \end{cases} \quad (5.20)$$

5.2.2 Speed controller

As seen from **Figure 5.1**, the speed controller generates the q-axis reference current.

Following equation (2.52), the mechanical system can be represented as follows:

$$\frac{d\omega_m}{dt} = \frac{1}{J} (T_{em} - T_{fric} - T_m) \quad (5.21)$$

where J is the combined inertia of the rotor and mechanical load, T_{em} is the electromagnetic torque, T_{fric} is the rotational friction torque and T_m is the load torque.

The relationship between the electromagnetic torque and the qd-axis currents are described by (2.55) as follows:

$$T_{em} = \frac{3p}{4} (\lambda_d i_q - \lambda_q i_d) \quad (5.22)$$

Since i_d^* is set to zero as discussed in section 5.1, the above equation can be simplified to:

$$T_{em} = \frac{3p}{4} \lambda'_m i_q \quad (5.23)$$

Here, p is the number of poles of the PMSM, and λ'_m is the flux linkage of the permanent magnet.

To obtain i_q^* , PI controller is used as illustrated in **Figure 5.1**.

Controller design

As discussed earlier, the speed loop is required to have a slower response than the current loop. This is achieved using the Symmetrical Optimum method which also fulfils Nyquist stability criterion without any problems. [52]

In equation (5.21), the load torque can be considered as disturbance, and the rotational friction torque can be neglected due to its low value. Taking these into account, the following transfer functions can be obtained from equations (5.21) and (5.23).

$$S(s) = \frac{T_{em}(s)}{i_q(s)} = \frac{3p}{4} \lambda'_m \quad (5.24)$$

$$T(s) = \frac{w_m(s)}{T_{em}(s)} = \frac{1}{Js} \quad (5.25)$$

The current loop can be modelled as a time delay T_c as follows:

$$C(s) = \frac{1}{1 + T_c s} \quad (5.26)$$

where $T_c = 2T_v$.

Hence the speed loop results in the block diagram shown in **Figure 5.4**.

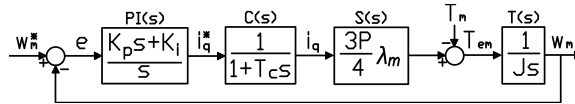


Figure 5.4: Speed control loop

The open loop transfer function of the speed control loop can be obtained as follows:

$$\begin{aligned} H_{OL}(s) &= PI(s)C(s)S(s)T(s) \\ &= \frac{K_i}{s} \left(1 + \frac{K_p s}{K_i}\right) \frac{1}{1 + T_c s} \frac{3p \lambda'_m}{4} \frac{1}{Js} \\ &= \frac{3p \lambda'_m K_p}{4J} \frac{1 + T_w s}{T_w s^2} \frac{1}{1 + T_c s} \end{aligned} \quad (5.27)$$

where $T_w = K_p / K_i$.

The closed loop transfer function of the speed control loop can then be expressed as:

$$H_{CL}(s) = \frac{3p\lambda'_m K_p (1 + T_w s)}{3p\lambda'_m K_p (1 + T_w s) + 4JT_w s^2 (1 + T_c s)} \quad (5.28)$$

The optimization then proceeds by applying the same principles used for the modulus optimum. This includes substituting jw for s , and setting the first $2n$ derivatives of the modulus, squared of the frequency response function, evaluated at $w = 0$, equal to zero. The resulting optimum criteria is: [53]

$$T_w = 4T_c \quad (5.29)$$

$$K_p = \frac{2J}{3p\lambda'_m T_c} \quad (5.30)$$

$$K_i = \frac{K_p}{T_w} \quad (5.31)$$

For the motor used in this study, the computed controller gains are as follows:

$$\begin{cases} K_p = 3581.4 \\ K_i = 0.63 \end{cases} \quad (5.32)$$

5.2.3 Controllable voltage source and transformation matrices

Normally, the reference signals \hat{v}_{dq}^* and θ^* are used as input signals which determines the output voltage of the VFD. In order to simplify the system modelling, it is assumed that the output voltage of the VFD is perfectly filtered and contains no harmonics.

Since the output signals of the vector control scheme is in dq reference frame, the output voltage of controller can be expressed using dq to abc transformation by the inverse of equation (2.25) as follows:

$$\begin{aligned} v_a(t) &= v_q^* \cos(\theta_r^*) + v_d^* \sin(\theta_r^*) \\ v_b(t) &= v_q^* \cos(\theta_r^* - 2\pi/3) + v_d^* \sin(\theta_r^* - 2\pi/3) \\ v_c(t) &= v_q^* \cos(\theta_r^* + 2\pi/3) + v_d^* \sin(\theta_r^* + 2\pi/3) \end{aligned} \quad (5.33)$$

The inverse transformation of the above is also used to transform phase currents to dq currents, which is used in current control loop. This is already described by equation (2.25).

5.3 Simulation model

A Simulink model of the controller based on equations derived in the previous section has been established.

The complete controller subsystem is illustrated in **Figure 5.1**, and shows the hierarchical structure. As shown, the controller subsystem is split up into the blocks previously discussed in this chapter.

The controller subsystem and its blocks implemented in Simulink are discussed in detail in Appendix A.5.

5.4 Estimation of rotor position using Extended Kalman Filter

The controller model described hitherto uses a position sensor. In order to remove the usage of position sensor, rotor position must be estimated.

Several schemes for position sensorless operation of PMSM exists and are presented in section 2.7. Of all these schemes, Kalman filtering is the most viable and efficient candidate for position estimation due to its recursive observation, prediction and correction processes as described in section 2.7.3. Consequently, in order for the controller model described hitherto to be sensorless, Extended Kalman Filter (EKF) is to be implemented.

This thesis follows the EKF algorithm proposed by Xiao-ling et al. [54] Some changes and corrections had been done, due to either misprints or miscalculations in the cited paper.

5.4.1 Speed and position estimation using EKF

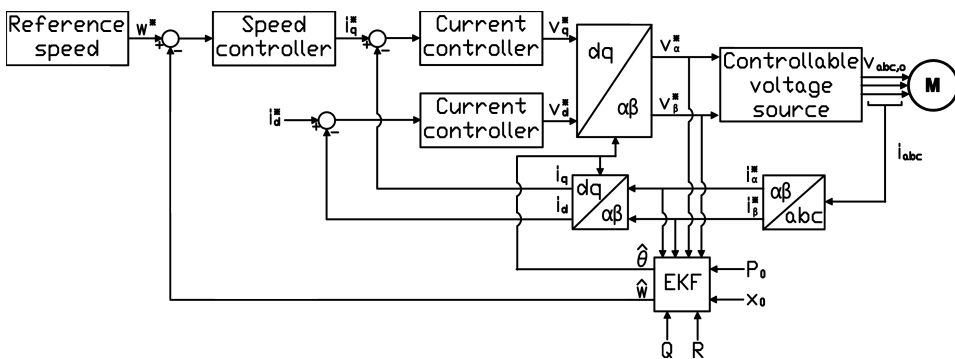


Figure 5.5: Sensorless field oriented controller using EKF overview

Using the field oriented controller described hitherto, the structure of the EKF sensorless PMSM drive is shown in **Figure 5.5**.

Assuming that the change in mechanical speed is negligible within one sampling period, the state equations of the PMSM can be expressed as follows:

$$\begin{cases} \frac{dx}{dt} = Ax + BU \\ y = Cx \end{cases} \quad (5.34)$$

Here, x is the state variable, U is the input and y is the output, as follows:

$$x^T = [i_d \quad i_q \quad w_r \quad \theta_r] \quad (5.35)$$

$$U^T = [U_\alpha \quad U_\beta] \quad (5.36)$$

$$y^T = [i_\alpha \quad i_\beta] \quad (5.37)$$

The matrices A , B and C are defined as follows:

$$A = \begin{bmatrix} -\frac{R_s}{L_d} & w_r \frac{L_q}{L_d} & 0 & 0 \\ -w_r \frac{L_d}{L_q} & -\frac{R_s}{L_q} & -\frac{\lambda_m}{L_q} & 0 \\ v0 & 0 & 0 & 0 \\ 0 & 0 & 1 & 0 \end{bmatrix} \quad (5.38)$$

$$B = \begin{bmatrix} \frac{\cos \theta_r}{L_d} & \frac{\sin \theta_r}{L_d} \\ -\frac{\sin \theta_r}{L_q} & \frac{\cos \theta_r}{L_q} \\ 0 & 0 \\ 0 & 0 \end{bmatrix} \quad (5.39)$$

$$C = \begin{bmatrix} \cos \theta_r & -\sin \theta_r & 0 & 0 \\ \sin \theta_r & \cos \theta_r & 0 & 0 \end{bmatrix} \quad (5.40)$$

Using a sampling time T , the discrete state equation is as follows:

$$\begin{cases} x(k+1) = A'x(k) + B'U(k) \\ y(k) = C'x(k) \end{cases} \quad (5.41)$$

where

$$A' = \begin{bmatrix} 1 - T \frac{R_s}{L_d} & w_r T \frac{L_q}{L_d} & 0 & 0 \\ -w_r T \frac{L_d}{L_q} & 1 - T \frac{R_s}{L_q} & -T \frac{\lambda_m}{L_q} & 0 \\ v 0 & 0 & 1 & 0 \\ 0 & 0 & T & 1 \end{bmatrix} \quad (5.42)$$

$$B' = \begin{bmatrix} T \frac{\cos \theta_r}{L_d} & T \frac{\sin \theta_r}{L_d} \\ -T \frac{\sin \theta_r}{L_q} & T \frac{\cos \theta_r}{L_q} \\ 0 & 0 \\ 0 & 0 \end{bmatrix} \quad (5.43)$$

$$C' = \begin{bmatrix} \cos \theta_r & -\sin \theta_r & 0 & 0 \\ \sin \theta_r & \cos \theta_r & 0 & 0 \end{bmatrix} \quad (5.44)$$

Considering noise and parameter errors, the state equations can be expressed as follows:

$$\begin{cases} x(k+1) = A'x(k) + B'U(k) + w(k) \\ y(k) = C'x(k) + v(k) \end{cases} \quad (5.45)$$

where w and v are the random disturbance and noise expressed via the following covariance matrices:

$$\begin{cases} Q = \text{cov}(w) = E\{ww^T\} \\ R = \text{cov}(v) = E\{vv^T\} \end{cases} \quad (5.46)$$

The grads matrices can be shown as follows:

$$\begin{aligned} G(k+1) &= \frac{\delta}{\delta x} (A'x + B'U)|_{x=\tilde{x}(k+1)} \\ &= \begin{bmatrix} 1 - T \frac{R_s}{L_d} & \tilde{w}_r(k+1) T \frac{L_q}{L_d} & T \frac{L_q}{L_d} \tilde{i}_q(k+1) & T \frac{U_q}{L_d} \\ -\tilde{w}_r(k+1) T \frac{L_d}{L_q} & 1 - T \frac{R_s}{L_q} & -\frac{T}{L_q} [L_d \tilde{i}_d(k+1) + \lambda_m] & T \frac{U_d}{L_q} \\ 0 & 0 & 1 & 0 \\ 0 & 0 & T & 1 \end{bmatrix} \end{aligned} \quad (5.47)$$

$$\begin{aligned} H(k+1) &= \frac{\delta}{\delta x} (C'x)|_{x=\tilde{x}(k+1)} \\ &= \begin{bmatrix} \cos \theta_r & -\sin \theta_r & 0 & -\tilde{i}_d \sin \theta_r - \tilde{i}_q \cos \theta_r \\ \sin \theta_r & \cos \theta_r & 0 & \tilde{i}_d \cos \theta_r - \tilde{i}_q \sin \theta_r \end{bmatrix} \end{aligned} \quad (5.48)$$

The EKF algorithm is composed of a three step loop. The first step performs a computation to get prediction state, output and covariance matrix P. The EKF gain matrix is get in the second step. In the last step, prediction state and covariance matrix P are corrected by real output.

The equations are shown as follow: [54]

Step 1: Prediction (time update)

$$\begin{aligned}\tilde{x}(k+1) &= A'\tilde{x}(k) + B'U(k) \\ \tilde{y}(k+1) &= C'\tilde{x}(k+1) \\ \tilde{p}(k+1) &= G(k+1)\tilde{p}(k)G(k+1)^T + Q\end{aligned}\quad (5.49)$$

Step 2: Compute EKF gain

$$K(k+1) = \tilde{p}(k+1)H(k+1)^T[H(k+1)\tilde{p}(k+1)H(k+1)^T + R]^{-1}\quad (5.50)$$

Step 3: Innovation (measurement update)

$$\begin{aligned}\hat{x}(k+1) &= \tilde{x}(k+1) + K(k+1)[y(k+1) - \tilde{y}(k+1)] \\ \hat{p}(k+1) &= \tilde{p}(k+1) - K(k+1)H(k+1)\tilde{p}\end{aligned}\quad (5.51)$$

5.4.2 Design of the covariance matrices

As discussed in section 2.7.3, the tuning of the covariance matrices P_0 , Q and R determines the position estimation performance. Varying P_0 yields different amplitude of the transient, while both transient duration and steady state conditions will be unaffected. Matrix Q gives the statistical description of the drive model. An increment of the elements of Q will likewise increase the EKF gain, resulting in a faster filter dynamic. On the other hand, matrix R is related to measurement noise. Increasing the values of the elements of R will mean that the measurements are affected by noise and thus they are of little confidence. Consequently, the filter gain will decrease, yielding poorer transient response. [54]

It is a common practice to assume the covariance matrices P_0 , Q and R to be diagonal. Using EKF, the estimated speed always delays the actual speed. This delay depends on the model covariance matrix Q . Lower elements q_{11} and q_{22} of Q , the lower delay of estimated speed. It has been found that the element that most influences the EKF convergence are q_{33} and q_{44} . Matrix R concerns the measurements noise. Tremendous value of R increases the convergence time up to instability. [54]

The covariance matrices are usually designed via trial and error, as they depend on precise system model and parameters. In this thesis, P_0 is set as a fixed diagonal matrix. Q , and R are set as variational diagonal matrices.

For the motor used in this study, the following covariance matrices are found to be appropriate via trial and error:

$$P_0 = \begin{bmatrix} 1 & & & \\ & 1 & & \\ & & 1 & \\ & & & 0.1 \end{bmatrix} \quad Q = \begin{bmatrix} 15.5 & & & \\ & 15.5 & & \\ & & 0.05 & \\ & & & 0.01 \end{bmatrix} \quad R = \begin{bmatrix} 1 & \\ & 1 \end{bmatrix}\quad (5.52)$$

However, the usage of trial and error is time consuming. Through the usage of Fuzzy Logic (FL) in order to modify the covariance matrix online, this design bottleneck is eliminated.

Moreover, through online updating of the covariance matrices, the dynamic response and steady-state accuracy are improved, and at the same time making the system more robust.

According to expert knowledge and experience principles, fuzzy control rules are set up in PMSM drive. Parameter adaptive fuzzy control is achieved by online enquiry form. Rules of ΔQ and ΔR are shown in the following tables: [54]

		E				
		NB	NS	ZE	PS	PB
EC	NB	NB	NB	NS	NS	ZE
	NS	NB	NS	NS	ZE	PS
	ZE	NS	NS	ZE	PS	PS
	PS	NS	ZE	PS	PS	PB
	PB	ZE	PS	PS	PB	PB

Table 5.1: Rules of ΔQ

		E				
		PB	PS	ZE	NS	NB
EC	NB	PB	PB	PS	PS	ZE
	NS	PB	PS	PS	ZE	NS
	ZE	PS	PS	ZE	NS	NS
	PS	PS	ZE	NS	NS	NB
	PB	ZE	NS	NS	NB	NB

Table 5.2: Rules of ΔR

In order to reduce computational complexity, $q_{11} = q_{22} = 15.5$ as obtained via trial and error. The covariance matrices are shown as follow:

$$P_0 = \begin{bmatrix} 1 & & & \\ & 1 & & \\ & & 1 & \\ & & & 0.1 \end{bmatrix}, Q = \begin{bmatrix} 15.5 & & & \\ & 15.5 & & \\ & & q_{33} & \\ & & & q_{44} \end{bmatrix}, R = \begin{bmatrix} r & \\ & r \end{bmatrix} \quad (5.53)$$

Here, $q_{33} = q_{44} = r = 0$ at the beginning.

According to the rules, the increment of parameter is gained by fuzzy inference controller, as described the following equations.

$$\begin{cases} q_{33} = q_{33} + \Delta Q_{33} \\ q_{44} = q_{44} + \Delta Q_{44} \\ r = r + \Delta R \end{cases} \quad (5.54)$$

where ΔQ_{33} , ΔQ_{44} and ΔR are the outputs from the fuzzy logic controller.

5.4.3 Simulation model

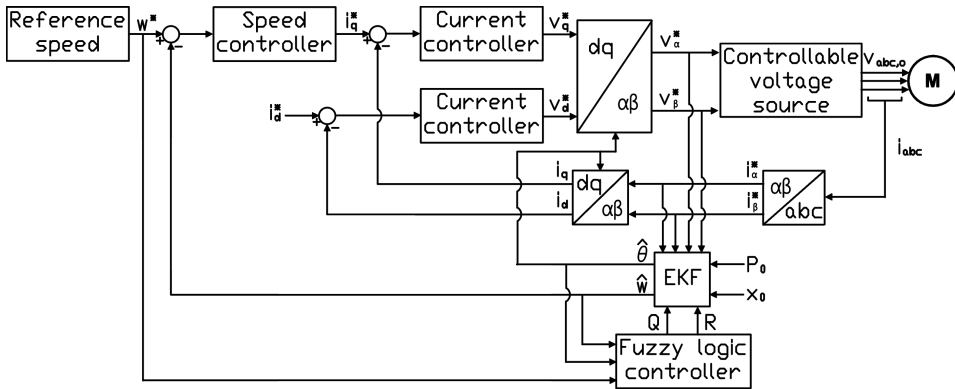


Figure 5.6: Sensorless field oriented controller using EKF and FL overview

A Simulink model of the EKF based on equations derived in the previous section has been established.

The complete controller subsystem including the position estimator is illustrated in **Figure 5.6**, and shows the hierarchical structure. As shown, the controller subsystem is split up into the blocks previously discussed in this chapter.

The controller subsystem and its blocks implemented in Simulink are discussed in detail in Appendix A.5.

Simulations

This chapter presents the simulations made in Simulink and the corresponding results.

6.1 General

6.1.1 Study case review

In order to ease readability, the two study cases presented in chapter 3 are shown again in the following figures:

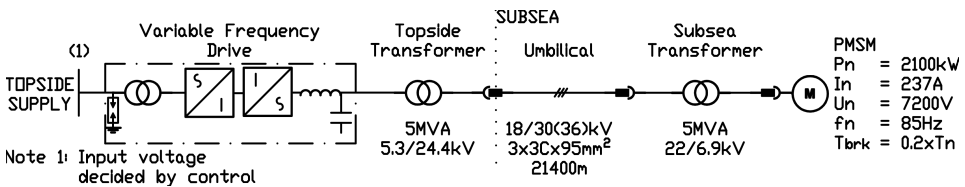


Figure 6.1: Electrical system topology - Base case

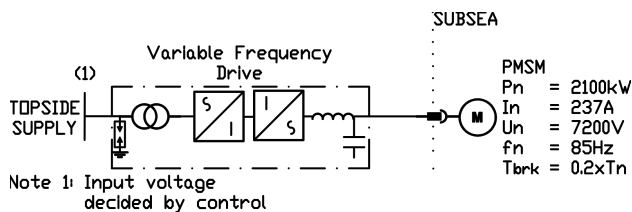


Figure 6.2: Electrical system topology - Test case

For detailed description of the study cases and its components, see chapter 3.

Simulation description

The study case described in chapter 3 is established in Simulink along with the controllers described in Chapters 4 and 5. The Simulink model is illustrated in appendix A.

The simulations are split up into the following sections:

- Open-loop scalar controller using constant voltage boosting
- Open-loop scalar controller using partial and delayed voltage boosting
- Closed-loop scalar controller
- Vector controller

Additionally for each part, it will be investigated how input parameters affect the start-up sequence of a PMSM as a part of the Scope of Work.

The following points affects all simulations unless otherwise stated:

- All input parameters are set to the ones stated in chapter 3.
- The slope of the reference frequency is set to be 0.01 pu/sec which corresponds to 0.85 Hz/sec .
- PMSM model 1.0 is used which has no damper windings, in order to test the control schemes.

The simulations are done using ode23t solver with a sample time of 0.1 ms.

Per-unit representation of simulation results

The per-unit system is a useful tool in presenting data, as all quantities are scaled to the maximum system values. This allows a shift of thinking in terms of percentages rather than absolute quantities. Additionally, all the relative magnitudes of all similar system quantities can directly be compared. Due to these reasons, all simulation results are given in per-unit quantities.

The per-unit quantities are calculated as follows:

$$\text{per - unit quantity} = \frac{\text{Actual quantity}}{\text{Base value of quantity}} \quad (6.1)$$

The base quantities of a P pole PMSM with rated line to line rms voltage and rated phase current of **Table 6.1** are shown in **Table 6.2**.

	Rated value	Base values
Voltage	7200 V Line-Line	$V_{base} = \sqrt{\frac{2}{3}} V_{LinetoLine}$
Current	237 A per phase	$i_{base} = \sqrt{2} i_{rated}$

Table 6.1: Rated and peak values

Primary quantity	Value
Base voltage	$V_b = \sqrt{\frac{2}{3}} V_{rated}$
Base peak current	$I_b = \sqrt{2} i_{rated}$
Angular velocity	$w_b = 2\pi f_{rated}$

Table 6.2: Primary base values

Using **Table 6.2**, the secondary base quantities can be defined as follows:

Secondary quantity	Value
Magnetic flux	$\Psi_b = \frac{V_b}{w_b}$
Base impedance	$Z_b = \frac{V_b}{I_b}$
Base inductance	$L_b = \frac{\Psi_b}{I_b}$
Base volt-ampere	$S_b = \frac{3}{2} V_b I_b$
Base mechanical angular velocity	$w_{bm} = 2 \frac{w_b}{P}$
Base torque	$T_b = \frac{S_b}{w_{bm}}$

Table 6.3: Secondary base values

6.2 Open-loop scalar controller using constant voltage boosting

This section presents the simulation results of the open-loop scalar control scheme using constant voltage boosting through rated stator current.

6.2.1 Testing the control scheme

Test case

In order to test the control scheme, the **Test case** is used with the PMSM model without damper windings.

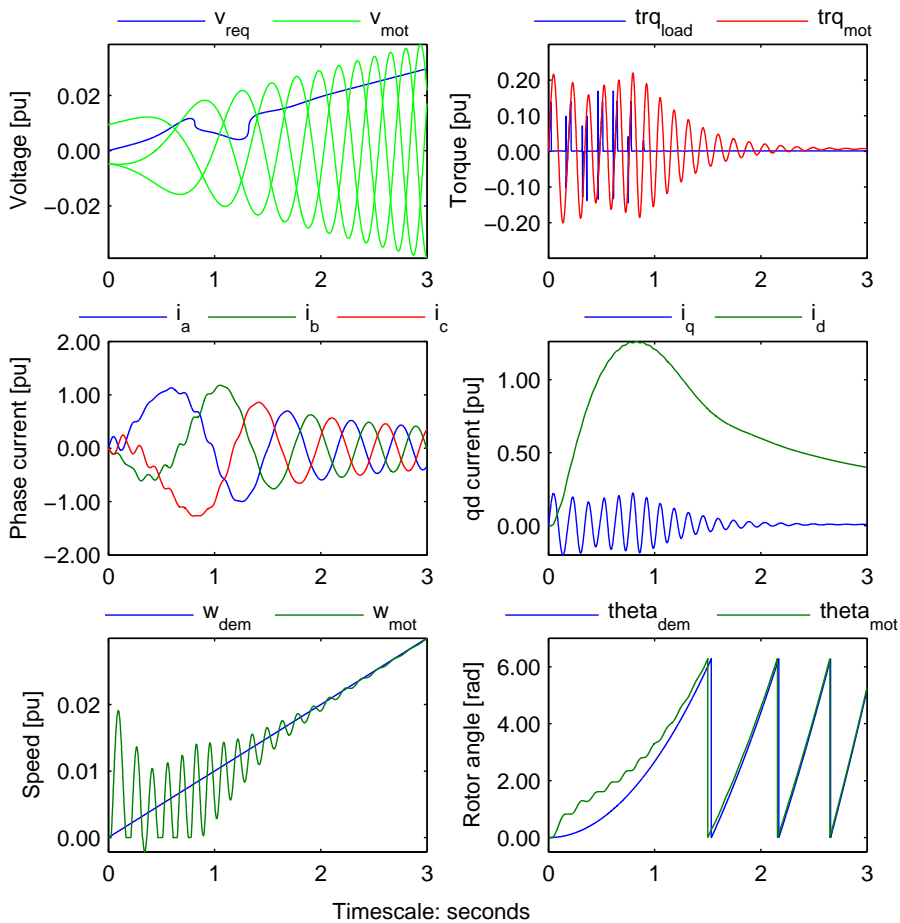


Figure 6.3: Constant voltage boosting simulation measurements - All waveforms - Test case, 3 sec simulation time

The start-up measurements for the mentioned case are shown in **Figure 6.3**.

The voltage waveforms in **Figure 6.3** shows the phase voltages and the required voltage magnitude across the PMSM terminals in green and blue respectively. The later voltage waveform is calculated using equation (4.11). As can be seen, due to calculation assumption that the stator current is constant equals to rated current all throughout the frequency range, the required voltage across the PMSM terminals are not met. Consequently this would mean that the PMSM enters over-excitation. This can clearly be seen on the same waveforms, which shows that the PMSM is overexcited all throughout the start-up period.

The current waveforms in **Figure 6.3** show the phase currents and the dq-axis currents. As shown, the start-up currents are tolerable, with the maximum phase current peak at 1.1 pu. This is primarily due to the high magnetizing current i_d caused by the motor over-excitation.

The start-up currents causes amplified electromagnetic torque oscillations due to lack of synchronism as illustrated by the torque waveforms of **Figure 6.3**. This in turn creates speed oscillations during start-up as shown by the speed waveforms of the same figure. It can also be observed that the oscillations die out after around 2 seconds as the motor achieves synchronization.

The rotor angle waveforms in **Figure 6.3** show the effect of the initial speed oscillation to the rotor's angular position.

Figure 6.3 thereby shows that the PMSM is able to start-up without losing its synchronization.

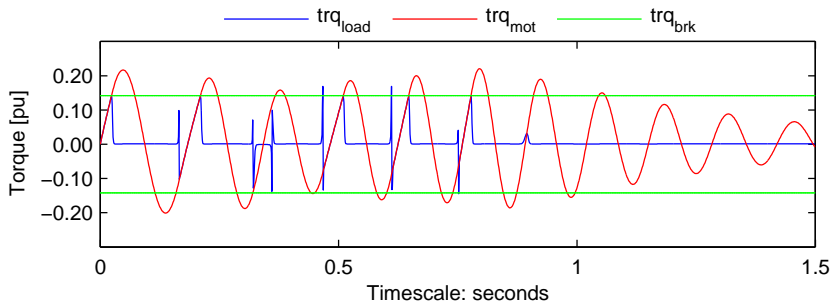


Figure 6.4: Constant voltage boosting simulation measurements - Torque waveforms - Test case, 1.5 sec simulation time

Figure 6.4 shows a closer view of the torque waveforms during the start-up simulation. As can be seen, the electromagnetic torque oscillations and hence the lack of synchronism are directly caused by the breakaway torque, as described by equation (3.1).

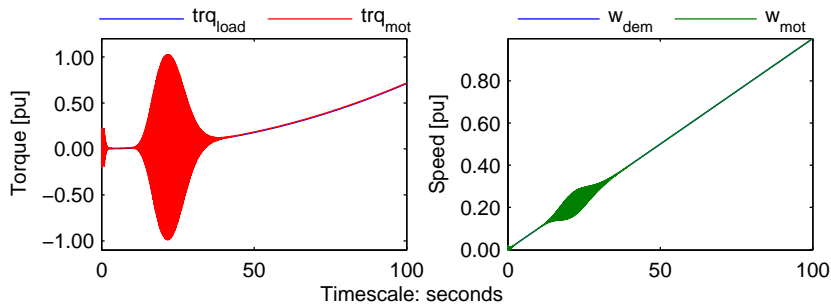


Figure 6.5: Constant voltage boosting simulation measurements - Torque and speed waveforms - Test case, 100 sec simulation time

Figure 6.5 shows the torque and speed waveforms when the control scheme is used up until the rated speed. As can be seen from the figure, stability is not guaranteed at certain speed ranges. This is discussed in section 2.5.

Base case

In order to test the transmission system voltage drop compensation algorithm, the **Base case** is used with the PMSM model without damper windings. The start-up measurements for the mentioned case are shown in **Figure 6.6**.

The voltage waveforms in **Figure 6.6** shows that again due to calculation assumption that the stator current is constant equals to rated current all throughout the frequency range, the required voltage across the PMSM terminals are not met. Consequently this would mean that the PMSM enters over-excitation.

The current waveforms in **Figure 6.6** show that the start-up currents still are tolerable, with the maximum phase current peak at 1.15 pu.

The torque waveforms in **Figure 6.6** still show torque oscillations due to lack of synchronism, which consequently creates speed oscillations as seen from the speed waveforms of the same figure. However, the oscillations die out after around 1.2 seconds as the motor achieves synchronization; which is comparatively faster than the previous simulation.

The rotor angle waveforms in **Figure 6.6** show the effect of the initial speed oscillation to the rotor's angular position.

Figure 6.7 shows the torque and speed waveforms when the control scheme is used up until the rated speed. As can be seen from the figure, the PMSM is stable and does not lose its synchronization all throughout the speed range. This is due to the transmission system components which acts as a damping to small system disturbances.

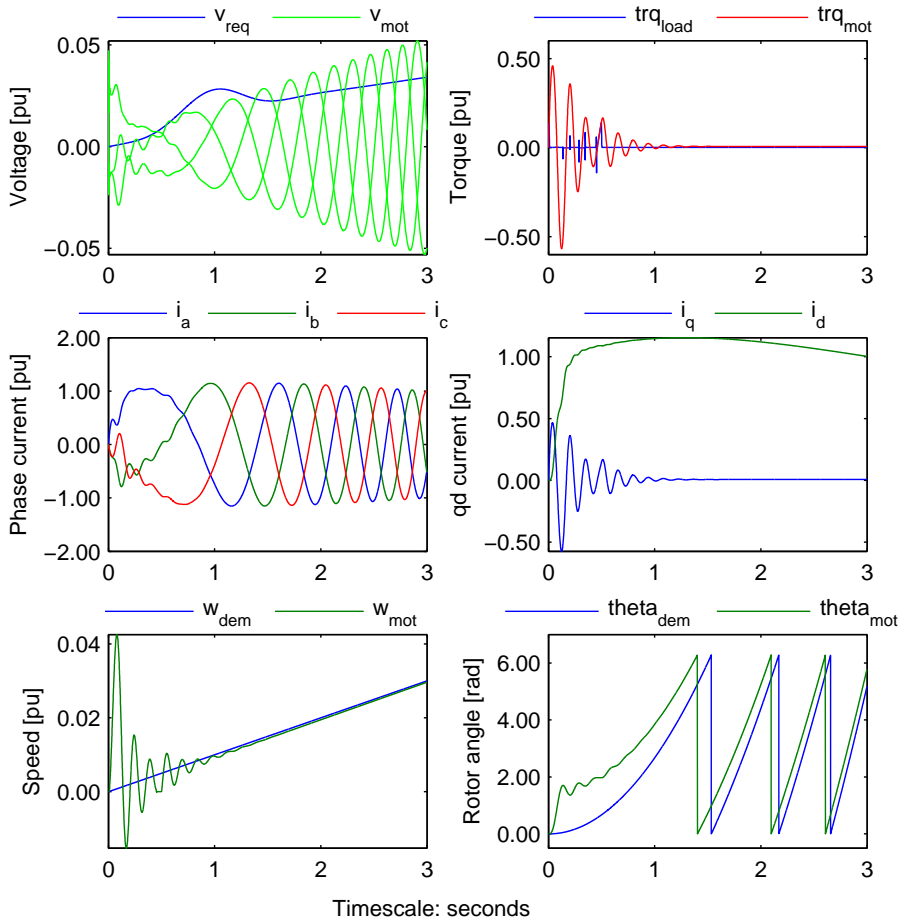


Figure 6.6: Constant voltage boosting simulation measurements - All waveforms - Base case, 3 sec simulation time

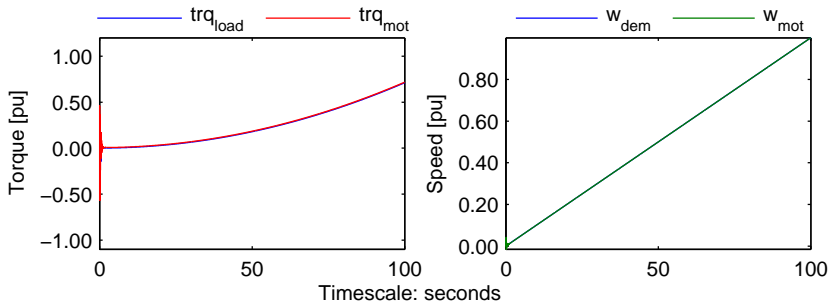


Figure 6.7: Constant voltage boosting simulation measurements - Torque and speed waveforms - Base case, 100 sec simulation time

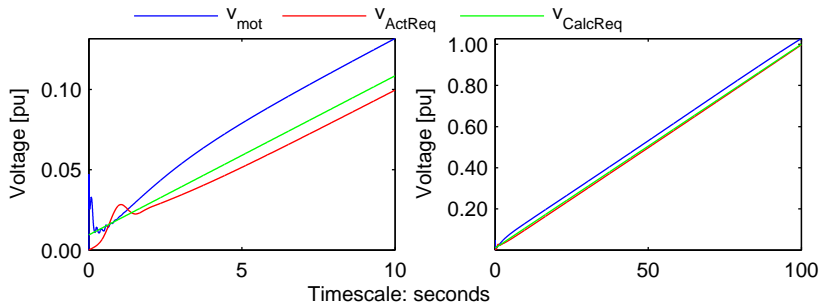


Figure 6.8: Constant voltage boosting simulation measurements - Voltage waveforms - Base case, 100 sec simulation time

Figure 6.8 shows the voltage waveforms during the initial start-up and when the control scheme is used up until the rated speed. The voltage waveforms include the phase voltage magnitude across the motor terminals, the actual required voltage magnitude, and the calculated required voltage magnitude of the control scheme; in blue, red and green respectively.

As can be seen from the figure, the required voltage across the PMSM terminals are not met, even with the voltage requirement calculation done by the control scheme, which consequently mean over-excitation of the PMSM all throughout the speed range. The over-excitation is intensified with the inaccuracy of the voltage drop compensation algorithm.

6.2.2 Parameter variations

This section investigates the effects of varying controller and system parameters on the start-up sequence of the PMSM. All simulations are performed using the **Base case** unless otherwise stated.

Reference frequency slope

The reference frequency slope is gradually increased from 0.001 to 0.075 *pu/sec* in order to see the dependency of the start-up procedure on the frequency slope.

Figure 6.9 shows the start-up currents and the start-up times as a function of the reference frequency slope, as a summary of this study. The start-up time is set to be the time from zero to the time the torque oscillations decrease beyond 0.01 pu.

As seen from the figure, the start-up time decreases rapidly as the frequency ramp slope is initially increased at lower values, and flats out at the higher values. The start-up currents show little variation, to as low as 0.07 pu difference between the result's local minima and maxima.

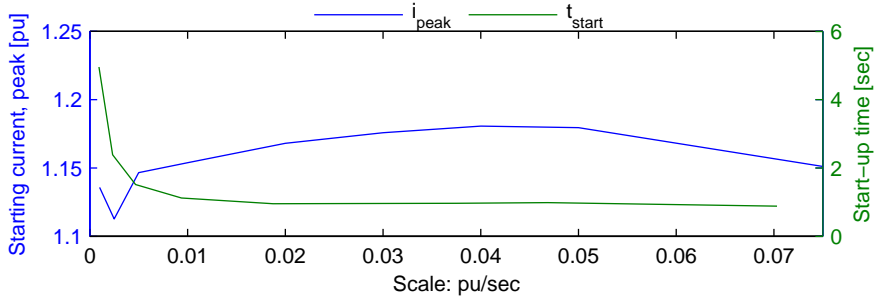


Figure 6.9: Constant voltage boosting simulation measurements - Start-up currents and times as a function of reference frequency slope - Base case

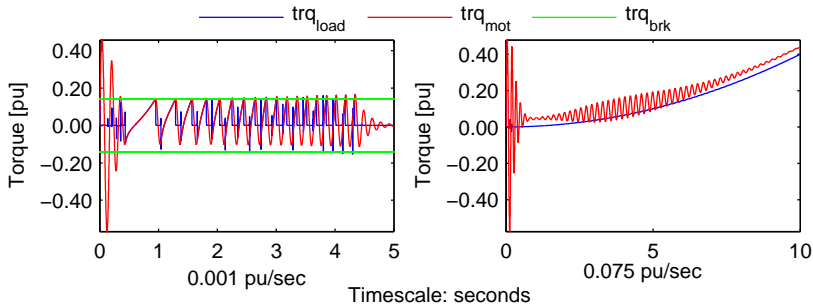


Figure 6.10: Constant voltage boosting simulation measurements - Torque waveforms - Base case, 0.001 and 0.075 pu/sec reference frequency slope

Figure 6.10 shows the torque waveforms from the lowest and the highest reference frequency slope used in the simulations.

As can be seen from the figure, too low reference frequency slope causes unnecessary oscillations due to the reduced torque build up, which consequently makes the start-up time higher as seen in **Figure 6.9**. Too high reference frequency slope on the other hand causes the PMSM to lose stability and thus its synchronization in certain speed ranges, which can be compared to **Figure 6.5**.

Cable length

The cable length is gradually increased from 10 to 100 km in order to see the dependency of the start-up procedure on the cable length.

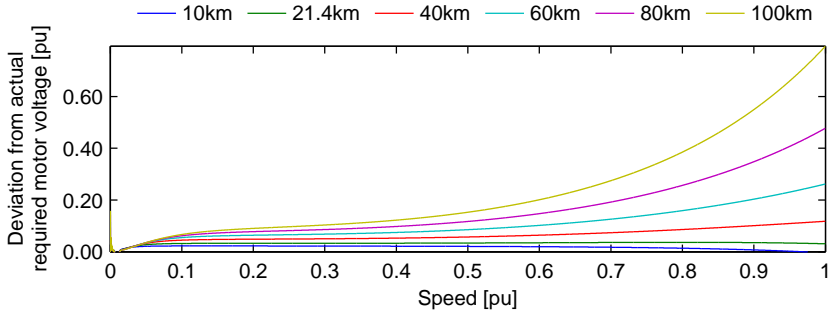


Figure 6.11: Constant voltage boosting simulation measurements - Deviation from actual required motor voltage as a function of speed - Base case

Figure 6.11 shows the deviation of the motor voltage from the actual required motor voltage as a function of the speed, as a summary of this study. Positive voltage deviation means that the PMSM is overexcited.

As seen from the figure, the voltage deviation is almost similar for all cable lengths during the initial period as the applied frequency is low. As the applied frequency is increased, the voltage deviation increases as well. The increase in voltage deviation is more significant in longer cables than shorter cables.

The voltage deviation that is seen from the figure is due to the lack of transmission system voltage drop calculation accuracy. For longer cables, the higher equivalent capacitive line charging current causes a higher voltage drop across the line inductance that is in phase with the sending end voltage, which consequently increases receiving end voltage.

Initial rotor position

The initial rotor position is varied in order to see the dependency of the start-up procedure on the initial rotor position, and in order to see if the controller is able to start-up the motor at all.

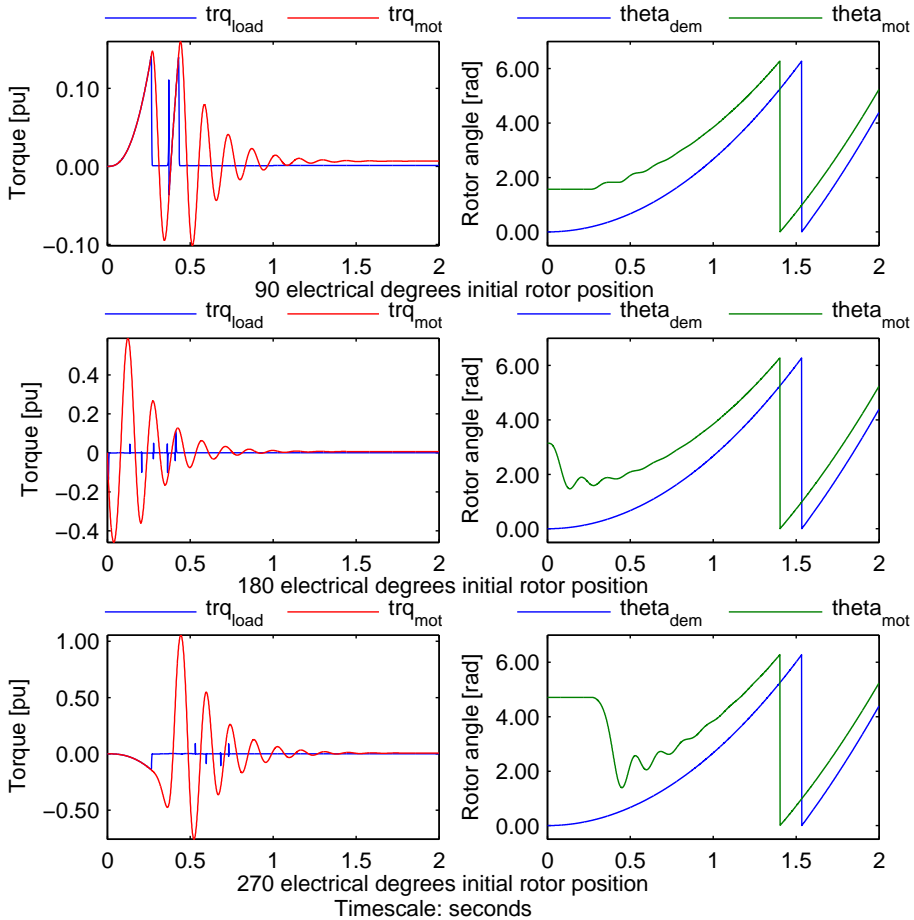


Figure 6.12: Constant voltage boosting simulation measurements - Torque and position waveforms - Base case, different initial rotor positions, 2 sec simulation time

Figure 6.12 shows the torque and angular position waveforms during the initial start-up period, for different initial rotor positions.

As seen from the figure, the controller is able to start-up the motor despite varying the initial rotor position. The torque waveforms illustrate that the initial rotor position decides the direction of the initial torque. This is discussed in section 2.6.

Motor damping

Motor model 2.1 is used with little damping winding coefficients in order to see the dependency of the start-up procedure on motor damping.

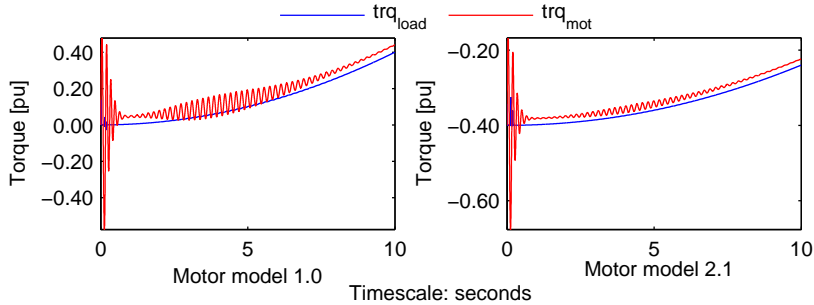


Figure 6.13: Constant voltage boosting simulation measurements - Torque waveforms - Base case, 0.075 pu/sec reference frequency slope, Motor model 1.0 and 2.1, 10 sec simulation time

Figure 6.13 shows the torque waveforms during the initial 10 seconds when the two different motor models developed in this thesis are used. The reference frequency slope is set to 0.075 pu/sec in order to obtain an unstable speed range with torque oscillations.

As seen from the figure, the rotor angle instability seen when using motor model 1.0 is lessened when motor model 2.1 is used. This is due to the addition of the damper windings in the motor equations, which generates opposing fields during periods of disturbances, thus improving machine stability. This is discussed in section 2.4.1.

Since the effects to the system stability of adding damper windings to the motor is expected to be the same for the other control schemes, the investigation of this parameter variation is thereby concluded.

Breakaway torque

The breakaway torque is varied in order to see the dependency of the start-up procedure on the breakaway torque.

Figure 6.14 shows the torque waveforms during the initial 1.5 seconds when the breakaway torque is set to 10% and 40% of the rated torque.

As seen from the figure, the torque oscillations experienced during start-up is directly affected by the breakaway torque. Additional torque oscillations can be experienced if the breakaway torque is too high due to the reduced torque build up, which consequently makes the start-up time higher. This is described by equation (3.1).

Since the effects to the start-up procedure of increasing the breakaway torque is expected to be the same for the other control schemes, the investigation of this parameter variation is thereby concluded.

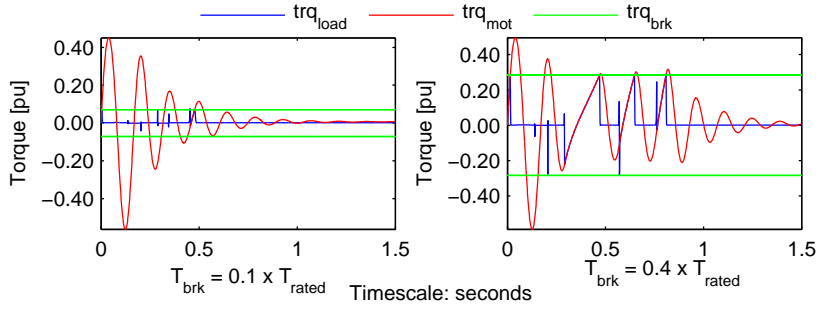


Figure 6.14: Constant voltage boosting simulation measurements - Torque waveforms - Base case, $T_{brk} = 0.1 T_{rated}$ and $T_{brk} = 0.4 T_{rated}$, 1.5 sec simulation time

6.3 Open-loop scalar controller using partial and delayed voltage boosting

This section presents the simulation results of the open-loop scalar control scheme using partial and delayed voltage boosting through rated stator current.

6.3.1 Testing the control scheme

Test case

In order to test the control scheme, the **Test case** is used with the PMSM model without damper windings. The border frequency is set to 6.5 Hz.

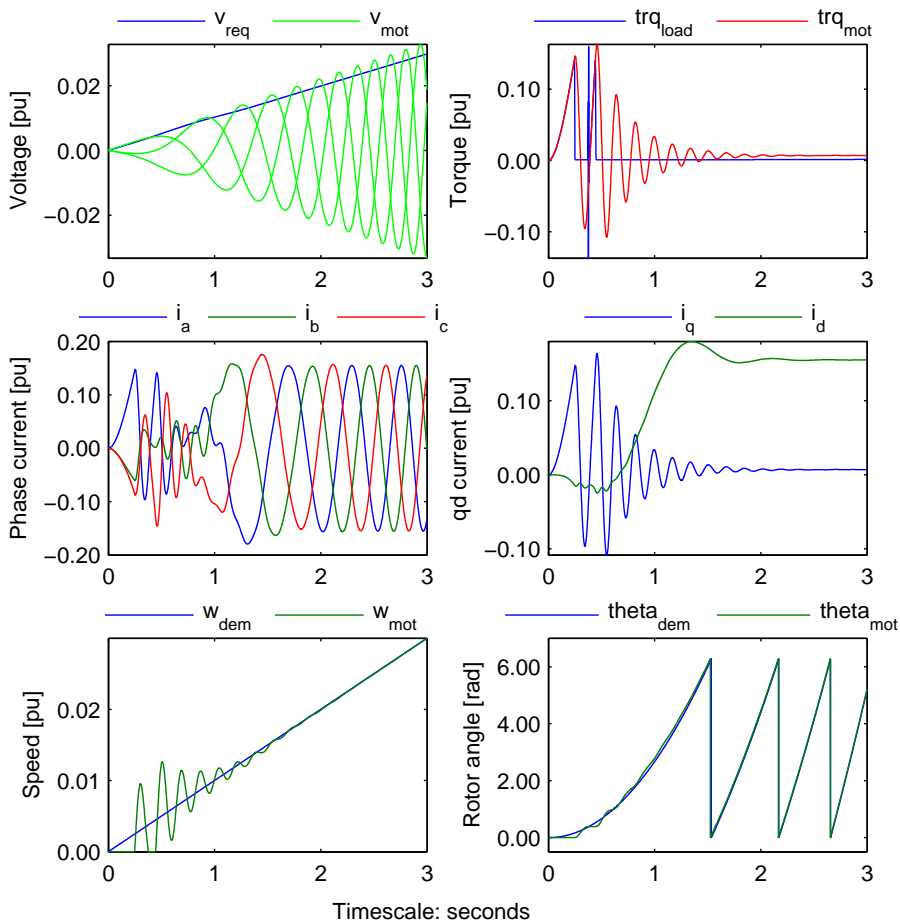


Figure 6.15: Partial and delayed voltage boosting simulation measurements - All waveforms - Test case, 3 sec simulation time

The start-up measurements for the mentioned case are shown in **Figure 6.15**.

The voltage waveforms in **Figure 6.15** shows the phase voltages and the required voltage magnitude across the PMSM terminals in green and blue respectively. As can be seen, due to the correct assumption that the peak stator current is not constant throughout the whole frequency range, the required voltage across the PMSM terminals are met during initial start-up. This is observed by comparing the figure above to **Figure 6.3**. However, after the border frequency is reached and the voltage calculation slope is changed the required voltage across the PMSM terminals are not met. Consequently this would mean that the PMSM enters over-excitation during that period.

The current waveforms in **Figure 6.15** show the phase currents and the dq-axis currents. As shown, the start-up currents are very low compared to the ones in **Figure 6.3**, with the maximum phase current peak at 0.18 pu, as a consequence of meeting the required motor voltage.

The start-up currents causes few electromagnetic torque oscillations due to lack of synchronism compared to the ones in **Figure 6.3**, as illustrated by the torque waveforms of **Figure 6.15**. This in turn creates speed oscillations during start-up as shown by the speed waveforms of the same figure. It can also be observed that the oscillations die out after around 2 seconds as the motor achieves synchronization.

The rotor angle waveforms in **Figure 6.15** show the effect of the initial speed oscillation to the rotor's angular position.

Figure 6.15 thereby shows that the PMSM is able to start-up without loosing its synchronization.

Similar to the previous control scheme, stability is not guaranteed at certain speed ranges, as shown in **Figure 6.5**. This is discussed in section 2.5.

Base case

In order to test the transmission system voltage drop compensation algorithm, the **Base case** is used with the PMSM model without damper windings. The border frequency is set to 28 Hz. The start-up measurements for the mentioned case are shown in **Figure 6.16**.

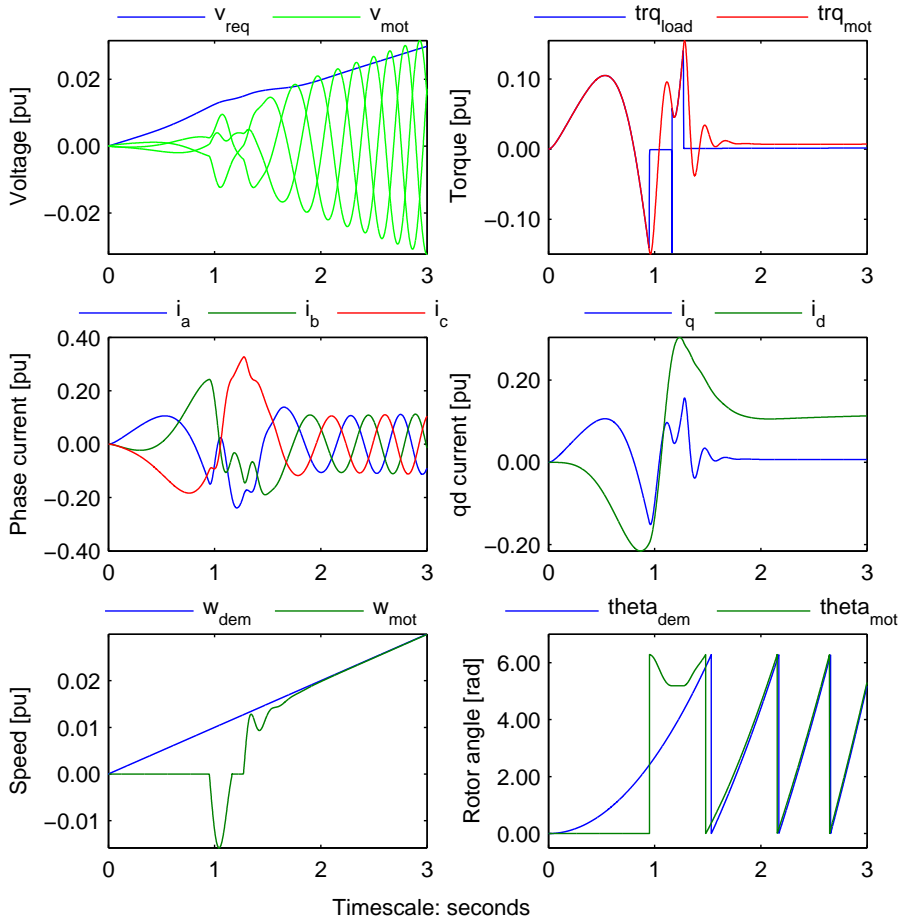


Figure 6.16: Partial and delayed voltage boosting simulation measurements - All waveforms - Base case, 3 sec simulation time

The voltage waveforms in **Figure 6.16** shows that due to calculation assumption that the stator current is constant equals to rated current all throughout the frequency range, the required voltage across the PMSM terminals are not met. Consequently this would mean that the PMSM enters over-excitation. This can be corrected by changing the border frequency.

The current waveforms in **Figure 6.16** show that the start-up currents still are very low due to the partial voltage boosting, with the maximum phase current peak at 0.38 pu; in comparison with the ones in **Figure 6.6**.

The torque waveforms in **Figure 6.16** still show torque oscillations due to lack of synchronism, which consequently creates speed oscillations as seen from the speed waveforms of the same figure. Moreover, the breakaway torque is achieved later due to the decreased volts per hertz ratio.

The rotor angle waveforms in **Figure 6.16** show the effect of the initial speed oscillation to the rotor's angular position.

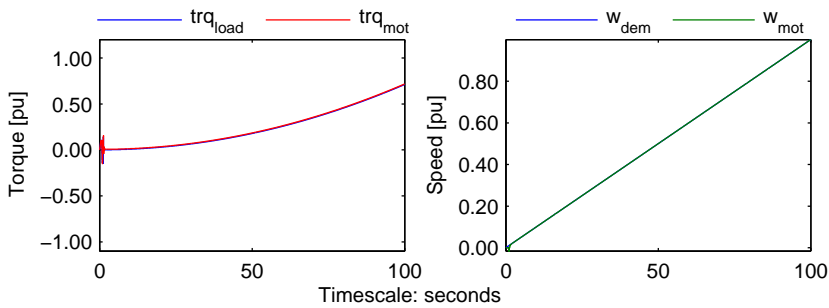


Figure 6.17: Partial and delayed voltage boosting simulation measurements - Torque and speed waveforms - Base case, 100 sec simulation time

Figure 6.17 shows the torque and speed waveforms when the control scheme is used up until the rated speed. As can be seen from the figure, the PMSM is stable and does not lose its synchronization all throughout the speed range. This is due to the transmission system components which acts as a damping to small system disturbances.

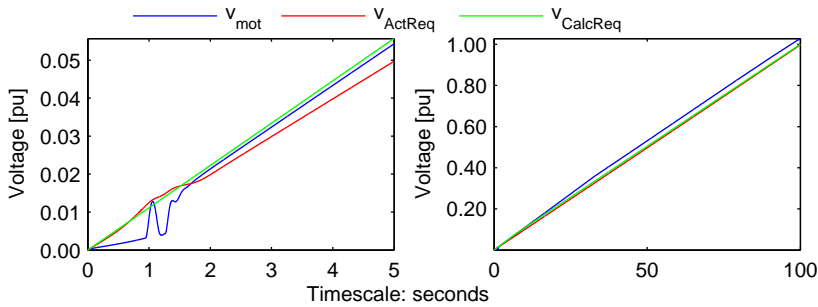


Figure 6.18: Partial and delayed voltage boosting simulation measurements - Voltage waveforms - Base case, 5 sec simulation time

Figure 6.18 shows the voltage waveforms during the initial start-up and when the control scheme is used up until the rated speed. The voltage waveforms include the phase voltage magnitude across the motor terminals, the actual required voltage magnitude, and the calculated required voltage magnitude of the control scheme; in blue, red and green respectively.

As can be seen from the figure, the required voltage across the PMSM terminals are not met, even with the voltage requirement calculation done by the control scheme, which consequently mean over-excitation of the PMSM all throughout the speed range. The over-excitation is intensified with the inaccuracy of the voltage drop compensation algorithm.

6.3.2 Parameter variations

This section investigates the effects of varying controller and system parameters on the start-up sequence of the PMSM. All simulations are performed using the **Base case** unless otherwise stated. The border frequency is set to 6.5 Hz unless otherwise stated.

Reference frequency slope

The reference frequency slope is gradually increased from 0.001 to 0.05 pu/sec in order to see the dependency of the start-up procedure on the frequency slope.

Figure 6.19 shows the start-up currents and the start-up times as a function of the reference frequency slope, as a summary of this study. The start-up time is set to be the time from zero to the time the torque oscillations decrease beyond 0.01 pu.

As seen from the figure, the start-up time decreases rapidly as the frequency ramp slope is initially increased at lower values, and flats out at the higher values.

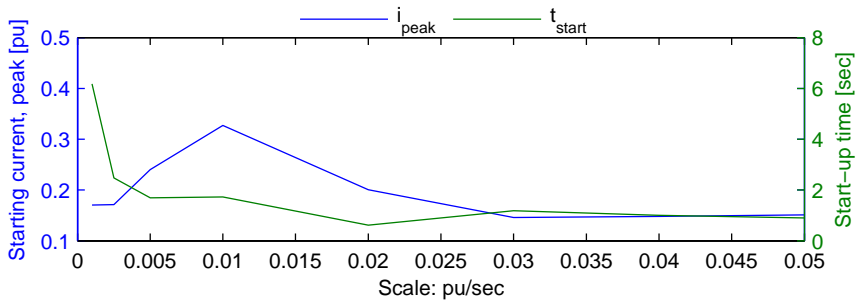


Figure 6.19: Partial and delayed voltage boosting simulation measurements - Start-up currents and times as a function of reference frequency slope - Base case

Cable length

The cable length is gradually increased from 10 to 100 km in order to see the dependency of the start-up procedure on the cable length.

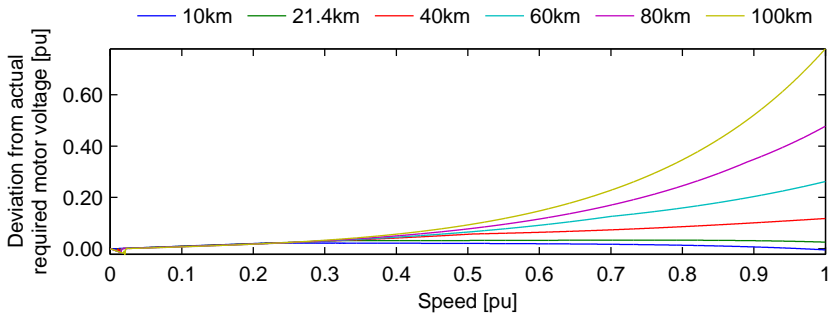


Figure 6.20: Partial and delayed voltage boosting simulation measurements - Deviation from actual required motor voltage as a function of speed - Base case

Figure 6.20 shows the deviation of the motor voltage from the actual required motor voltage as a function of the speed, as a summary of this study. Positive voltage deviation means that the PMSM is overexcited.

As seen from the figure, the voltage deviation is almost similar to the ones in **Figure 6.11**, except for the ones during the initial period as the applied frequency is low. It can be clearly seen that the control algorithm makes the voltage deviation during the initial period negligible. However, just as **Figure 6.11**, as the applied frequency is increased, the voltage deviation increases as well. However, due to the partial and delayed voltage boosting, the voltage deviation increases later than the ones shown in 6.11.

The voltage deviation that is seen from the figure is due to the lack of transmission system voltage drop calculation accuracy. For longer cables, the higher equivalent capacitive line charging current causes a higher voltage drop across the line inductance that is in phase

with the sending end voltage, which consequently increases receiving end voltage.

Initial rotor position

The initial rotor position is varied in order to see the dependency of the start-up procedure on the initial rotor position, and in order to see if the controller is able to start-up the motor at all.

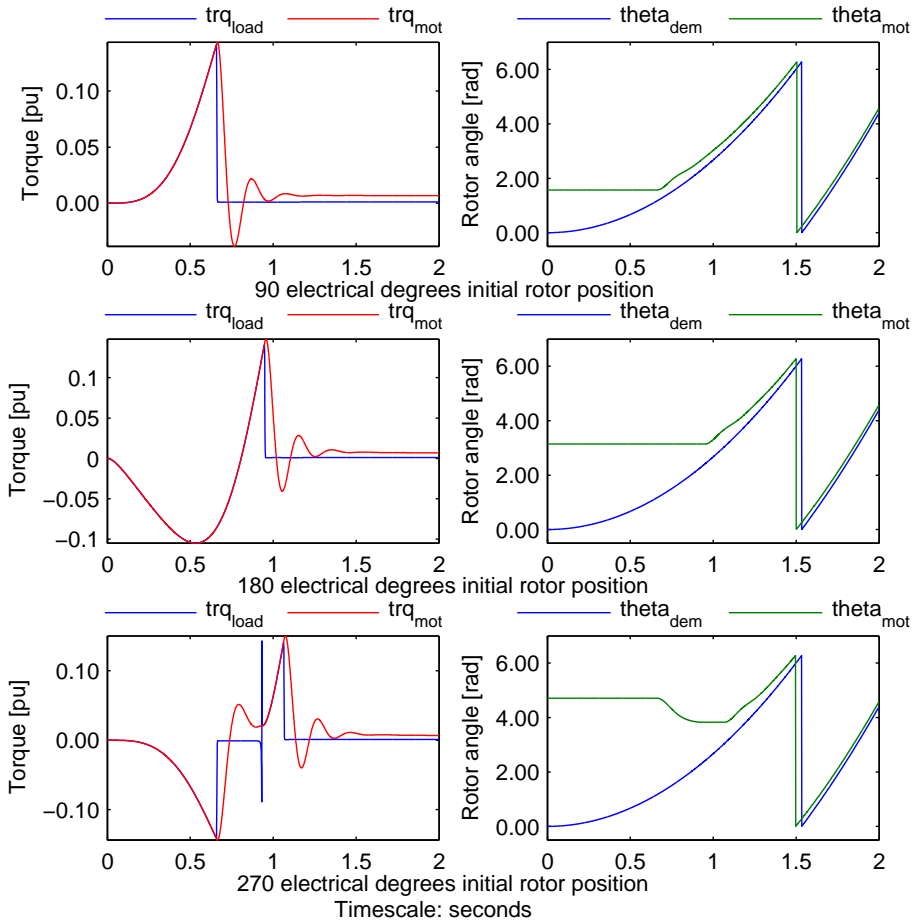


Figure 6.21: Partial and delayed voltage boosting simulation measurements - Torque and position waveforms - Base case, different initial rotor positions, 2 sec simulation time

Figure 6.21 shows the torque and angular position waveforms during the initial start-up period, for different initial rotor positions.

As seen from the figure, the controller is able to start-up the motor despite varying the initial rotor position. The torque waveforms illustrate that the initial rotor position decides

the direction of the initial torque. This is discussed in section 2.6.

Border frequency

The border frequency is varied in order to see the dependency of the start-up procedure on the border frequency.

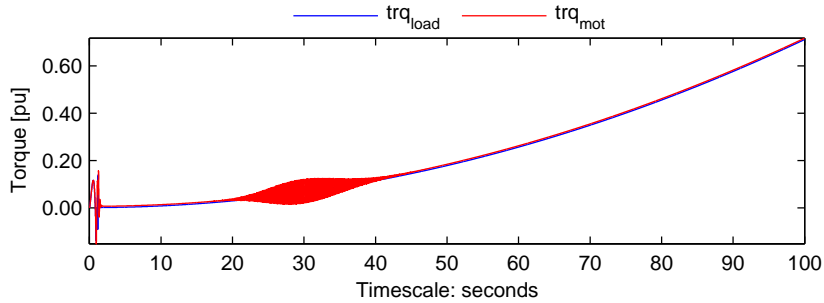


Figure 6.22: Partial and delayed voltage boosting simulation measurements - Torque waveform - Base case, 14 Hz border frequency, 100 sec simulation time

Figure 6.22 shows the torque waveform during the entire speed range when the border frequency is set to 14 Hz. As seen from the figure, decreasing border frequency too much causes oscillatory behaviour to reappear as the volts per hertz ratio after the border frequency becomes too high. The initial start-up waveforms are the same as the ones shown in **Figure 6.16**.

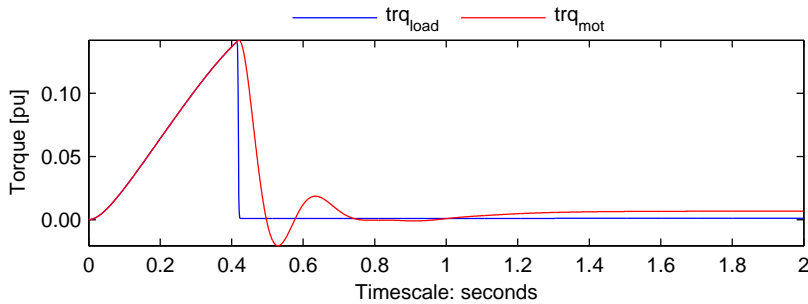


Figure 6.23: Partial and delayed voltage boosting simulation measurements - Torque waveform - Base case, 5 Hz border frequency, 2 sec simulation time

Figure 6.23 shows the torque waveform during the initial start-up period when the border frequency is set to 5 Hz. As seen from the figure, decreasing the border frequency even further enables the breakaway torque to be achieved earlier due to the higher volts per hertz ratio. However, the oscillatory behaviour experienced with the previous simulation still persists, and even more prominent due to the decreased border frequency.

6.4 Closed-loop scalar controller

This section presents the simulation results of the closed-loop scalar control scheme.

6.4.1 Testing the control scheme

Test case

In order to test the control scheme, the **Test case** is used with the PMSM model without damper windings.

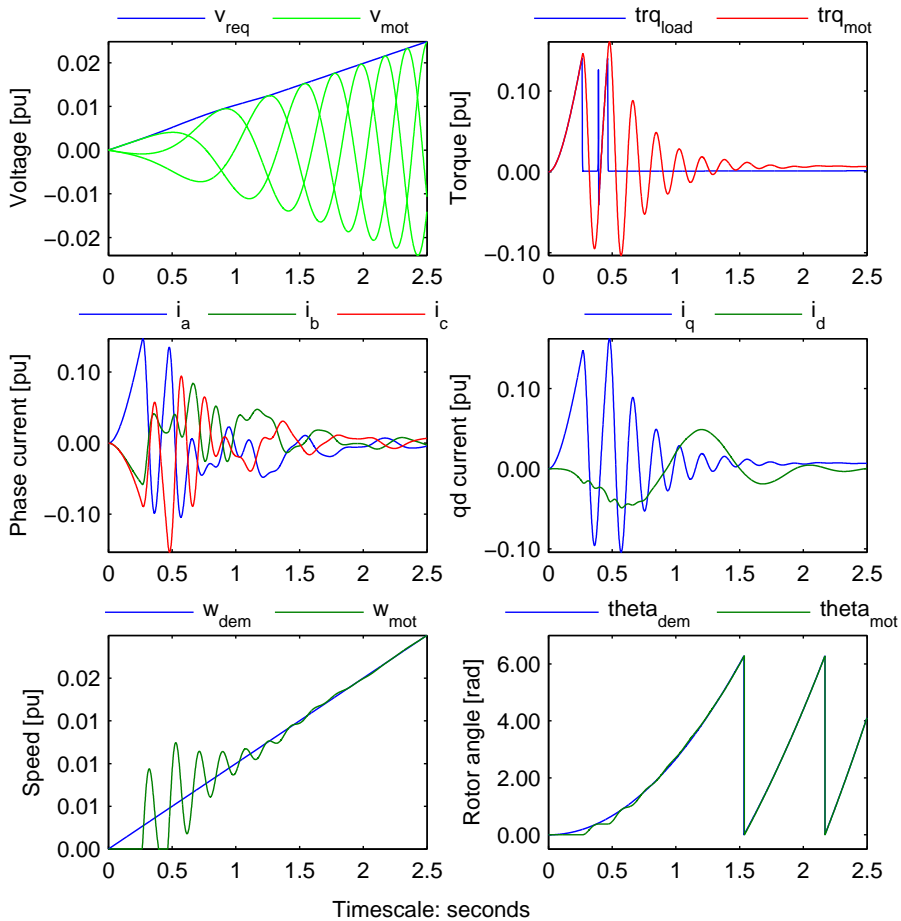


Figure 6.24: Closed-loop scalar control simulation measurements - All waveforms - Test case, 3 sec simulation time

The start-up measurements for the mentioned case are shown in **Figure 6.24**.

The voltage waveforms in **Figure 6.24** shows the phase voltages and the required voltage magnitude across the PMSM terminals in green and blue respectively. As can be seen, since the actual stator current is measured, the required voltage across the PMSM terminals are met all throughout the frequency range. This is observed by comparing the figure above to **Figure 6.3**.

Consequently, the start-up currents are comparably low compared to the two previous control methods as shown in the current waveforms of **Figure 6.24**. This is a consequence of the precise control which makes it certain that the motor does not enter over-excitation.

The start-up currents causes few electromagnetic torque oscillations due to lack of synchronism which are comparable to the ones in **Figure 6.15**, as illustrated by the torque waveforms of **Figure 6.24**. This in turn creates speed oscillations during start-up as shown by the speed waveforms of the same figure. It can also be observed that the oscillations die out after around 2 seconds as the motor achieves synchronization.

The rotor angle waveforms in **Figure 6.24** show the effect of the initial speed oscillation to the rotor's angular position.

To summarize, the motor is able to start-up with almost negligible oscillations and little start-up current. It can be said that the illustrated start-up behaviour is preferable than the previous start-up behaviours produced by other control methods.

However, similar to the previous control schemes, stability is not guaranteed at certain speed ranges; similar to the ones shown in **Figure 6.5**. This is discussed in section 2.5.

Base case

In order to test the transmission system voltage drop compensation algorithm, the **Base case** is used with the PMSM model without damper windings. The start-up measurements for the mentioned case are shown in **Figure 6.25**.

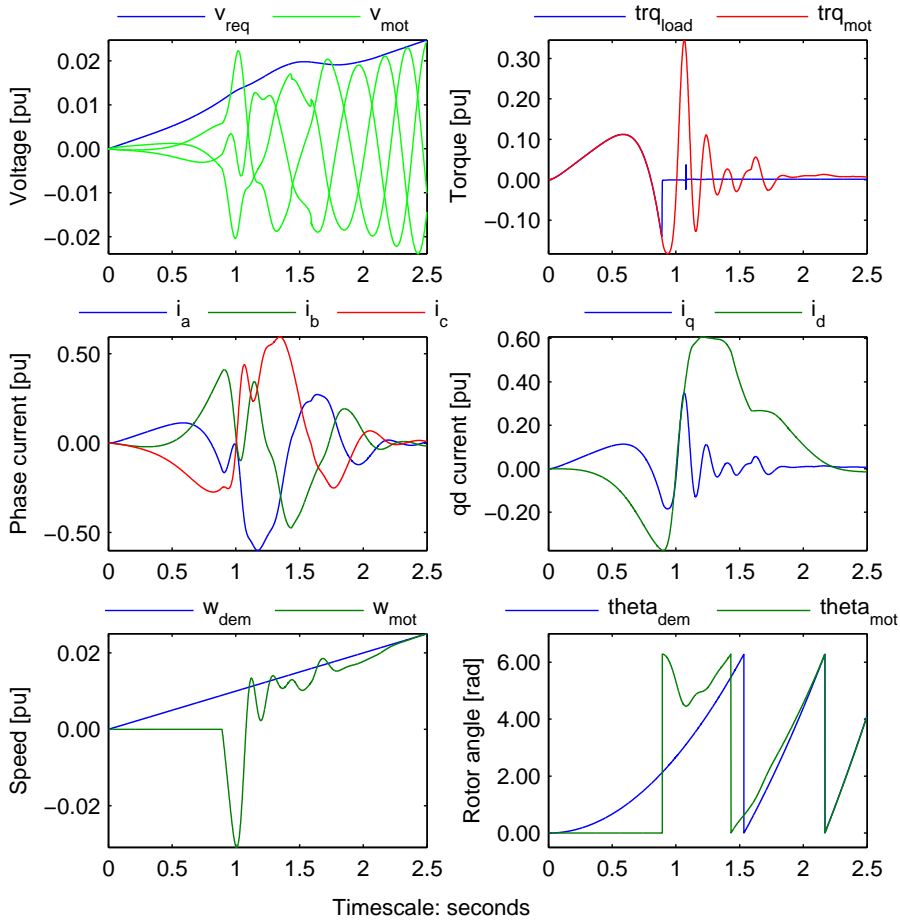


Figure 6.25: Closed-loop scalar control simulation measurements - All waveforms - Base case, 3 sec simulation time

The voltage waveforms in **Figure 6.25** show that the required motor voltage still is met all throughout the frequency range. However, the current waveforms in the same figure show that the start-up currents are higher than the previous simulation, with the maximum phase current peak at 0.52 pu.

The torque waveforms in **Figure 6.25** still show torque oscillations due to lack of synchron-

ism, which consequently creates speed oscillations as seen from the speed waveforms of the same figure. Moreover, the initial breakaway torque is achieved in the negative region due to the reduced initial torque build up. Based from previous simulations, this can be corrected by increasing the reference frequency slope.

However, despite the addition of the transmission system components, stability is still not guaranteed at certain speed ranges, as shown in the torque waveform of **Figure 6.26**. This is discussed in section 2.5. Consequently, this rotor angle instability necessitates the implementation of the stabilization loop.

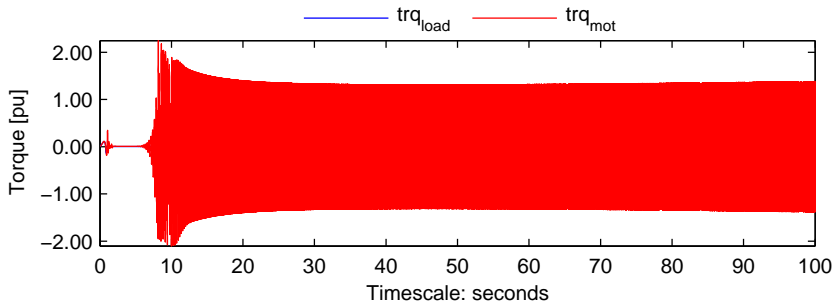


Figure 6.26: Closed-loop scalar control simulation measurements - Torque waveform - Base case, 100 sec simulation time

Base case with stabilization loop

In order to get the closed loop scalar control scheme to be stable all throughout the whole frequency range, the stabilization loop is implemented. The stabilization loop is turned on after 4 seconds when the rotor angle instability starts occurring, as shown in **Figure 6.26**. Through trial and error, the appropriate stabilizer gain has been found to be 0.09.

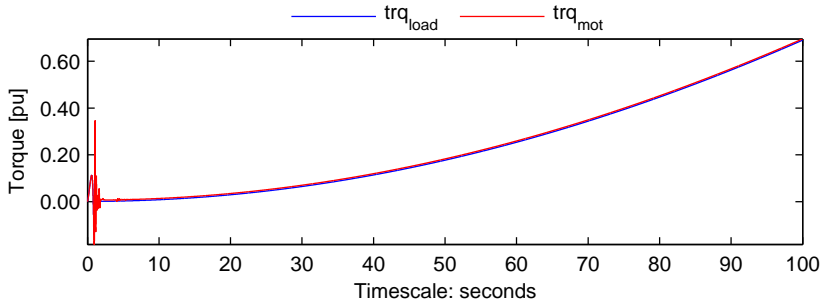


Figure 6.27: Closed-loop scalar control simulation measurements - Torque waveform - Base case with stabilization loop, 100 sec simulation time

The torque waveform shown in **Figure 6.27** illustrates that the stabilization loop is able to properly modulate the frequency of the machine, thus stabilizing the system for the whole applied frequency range.

6.4.2 Parameter variations

This section investigates the effects of varying controller and system parameters on the start-up sequence of the PMSM. All simulations are performed using the **Base case** with stabilization loop unless otherwise stated.

Reference frequency slope

The reference frequency slope is gradually increased from 0.0025 to 0.03 pu/sec in order to see the dependency of the start-up procedure on the frequency slope.

Figure 6.28 shows the start-up currents and the start-up times as a function of the reference frequency slope, as a summary of this study. The start-up time is set to be the time from zero to the time the torque oscillations decrease beyond 0.01 pu.

As seen from the figure, the start-up time decreases rapidly as the frequency ramp slope is initially increased at lower values, and flats out at the higher values.

Additionally, as the reference frequency slope is increased, the time when the stabilization loop is required to be implemented decreases.

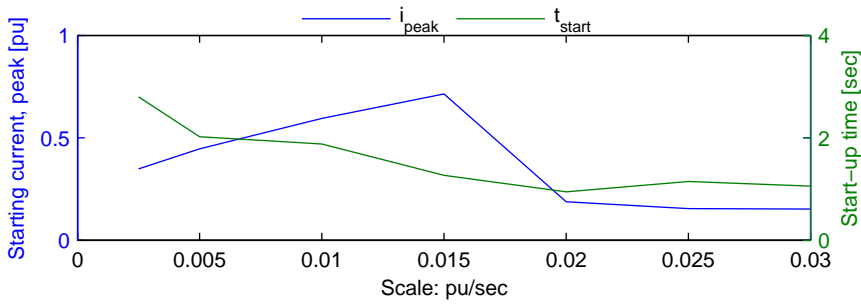


Figure 6.28: Closed-loop scalar control simulation measurements - Start-up currents and times as a function of reference frequency slope - Base case with stabilization loop

Cable length

The cable length is gradually increased from 10 to 80 km in order to see the dependency of the start-up procedure on the cable length.

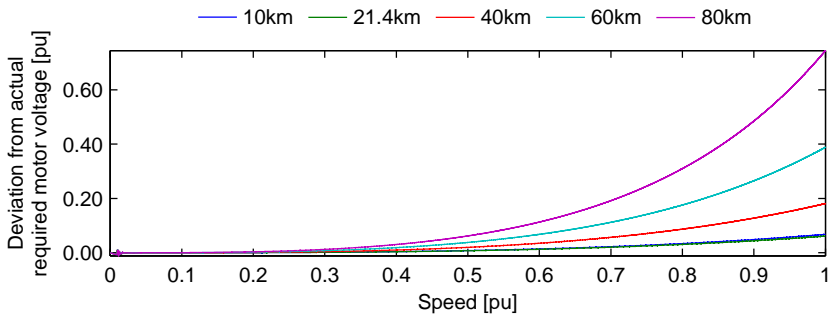


Figure 6.29: Closed-loop scalar control simulation measurements - Deviation from actual required motor voltage as a function of speed - Base case with stabilization loop

Figure 6.29 shows the deviation of the motor voltage from the actual required motor voltage as a function of the speed, as a summary of this study. Positive voltage deviation means that the PMSM is overexcited. Due to the huge increase in simulation time as longer cable lengths are used, the 100 km cable length simulation was skipped, in comparison to the previous cable length variation studies.

The figure illustrates that during the initial period as the applied frequency is low, the voltage deviation is approximately zero; as a consequence of the precise transmission system voltage drop compensation algorithm. However, just as **Figure 6.20**, as the applied frequency is increased, the voltage deviation increases as well.

It can also be noticed that for the 80 km cable length, the voltage deviation caused by the current control algorithm is around 0.7 pu compared to the 0.45 pu caused by the previous

control algorithm, shown in **Figure 6.20**. This is due to the lack of the inductance term in the previous control algorithm. The inclusion of the inductance algorithm increases the voltage signal sent by the controller, which consequently increases the receiving end voltage, higher than what the previous algorithm does.

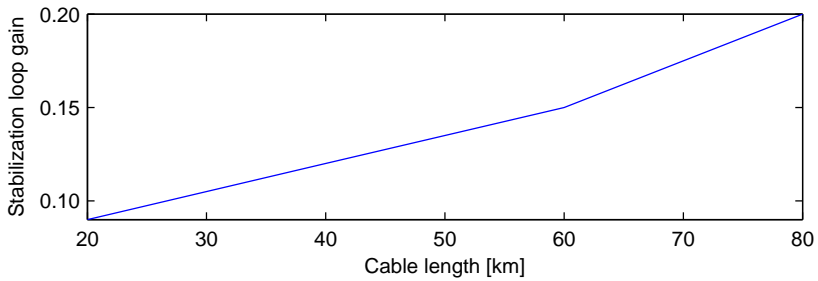


Figure 6.30: Closed-loop scalar control simulation measurements - Required stabilization loop gain as a function of cable length - Base case with stabilization loop

Additionally, **Figure 6.30** illustrates that the required stabilization loop gain in order to maintain system stability all throughout the frequency range increases as cable length is increased.

Initial rotor position

The initial rotor position is varied in order to see the dependency of the start-up procedure on the initial rotor position, and in order to see if the controller is able to start-up the motor at all.

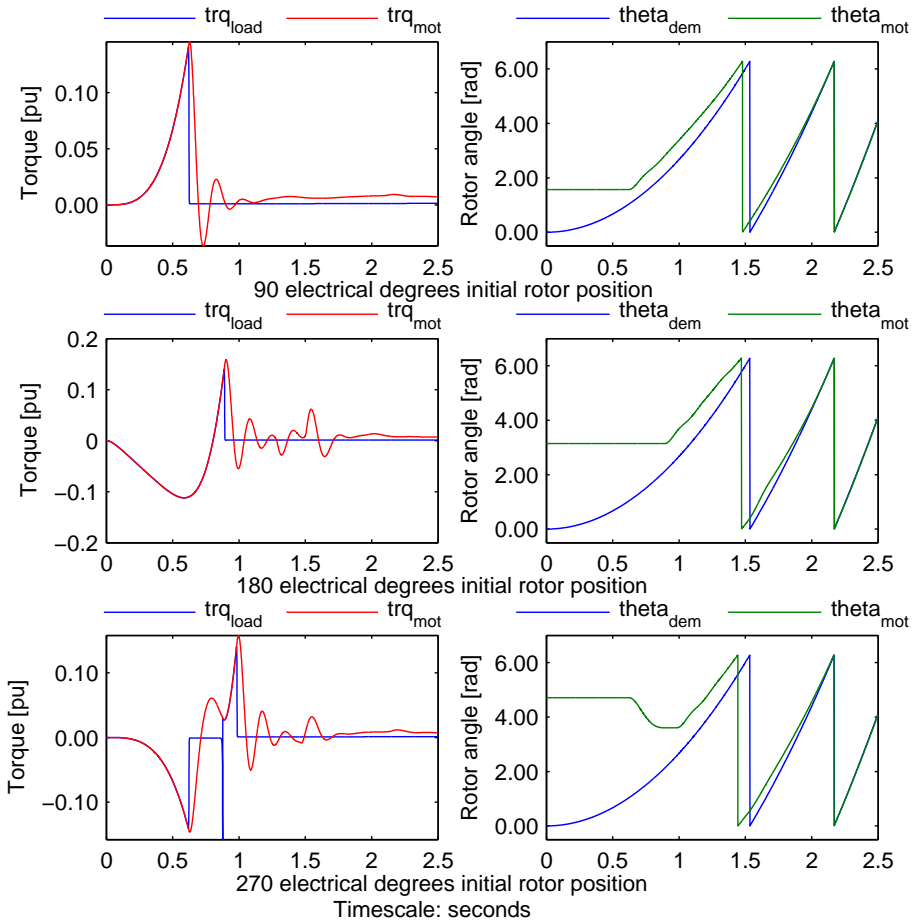


Figure 6.31: Closed-loop scalar control simulation measurements - Torque and position waveforms - Base case with stabilization loop, different initial rotor positions, 2.5 sec simulation time

Figure 6.31 shows the torque and angular position waveforms during the initial start-up period, for different initial rotor positions.

As seen from the figure, the controller is able to start-up the motor despite varying the initial rotor position. The torque waveforms illustrate that the initial rotor position decides the direction of the initial torque. This is discussed in section 2.6.

6.4.3 Response to load change

Since the stabilization loop enables the system to be stable throughout the whole frequency range, the control scheme can therefore be used even after the start-up procedure. In order to test the controller's response to load change during stable operation, the reference frequency is varied after the start-up procedure.

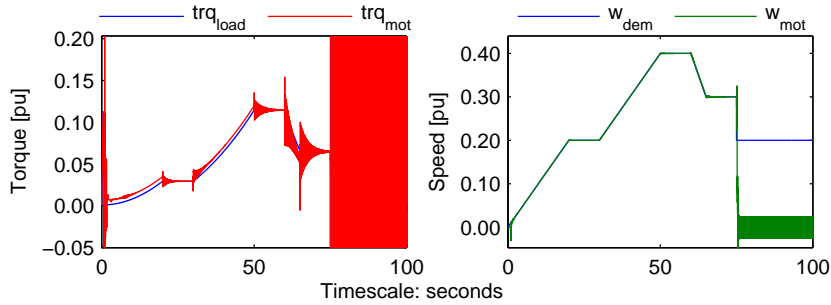


Figure 6.32: Closed-loop scalar control simulation measurements - Speed waveform - Base case with stabilization loop, 100 sec simulation time

Figure 6.31 shows the speed waveforms as the speed reference is changed during steady state.

As seen from the figure, the controller is able to fulfil the speed demands with some overshoot and initial torque oscillations when the rate of change of the speed command is changed. A huge change in the speed command will cause too much torque oscillations which will consequently make the motor go out of synchronization, as observed by the end of the simulation when a step change in speed is demanded.

6.5 Vector controller

This section presents the simulation results of the vector controller using position sensor.

6.5.1 Testing the sensed vector controller

In order to test the response of the sensed vector controller, the reference frequency is varied after the start-up procedure.

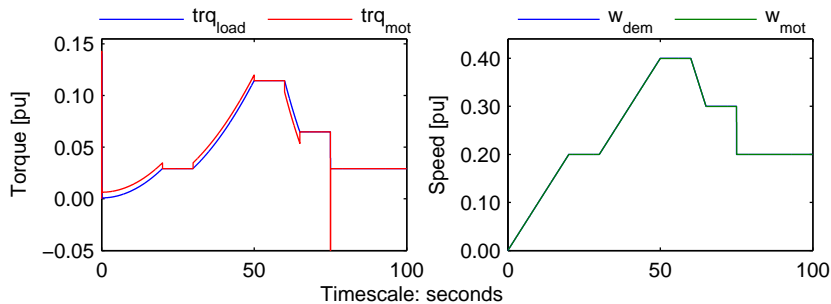


Figure 6.33: Vector control simulation measurements - Torque and speed waveform - Test case, 100 sec simulation time

Figure 6.33 shows the torque and speed waveforms as the speed reference is changed during steady state.

As seen from the figure, the controller is able to start-up and fulfil the speed demands with very little overshoot, even during step changes of the reference speed. This is due to the precise control of the rotor field as described in chapter 5.

6.5.2 Testing the position estimator

EKF with predefined covariance matrices

In order to test the EKF with the predefined matrices described in section 5.4.2, the sensed vector controller is used with varying speed reference. The position estimator is then fed with the measured phase currents and the calculated $\alpha\beta$ voltages by the controller.

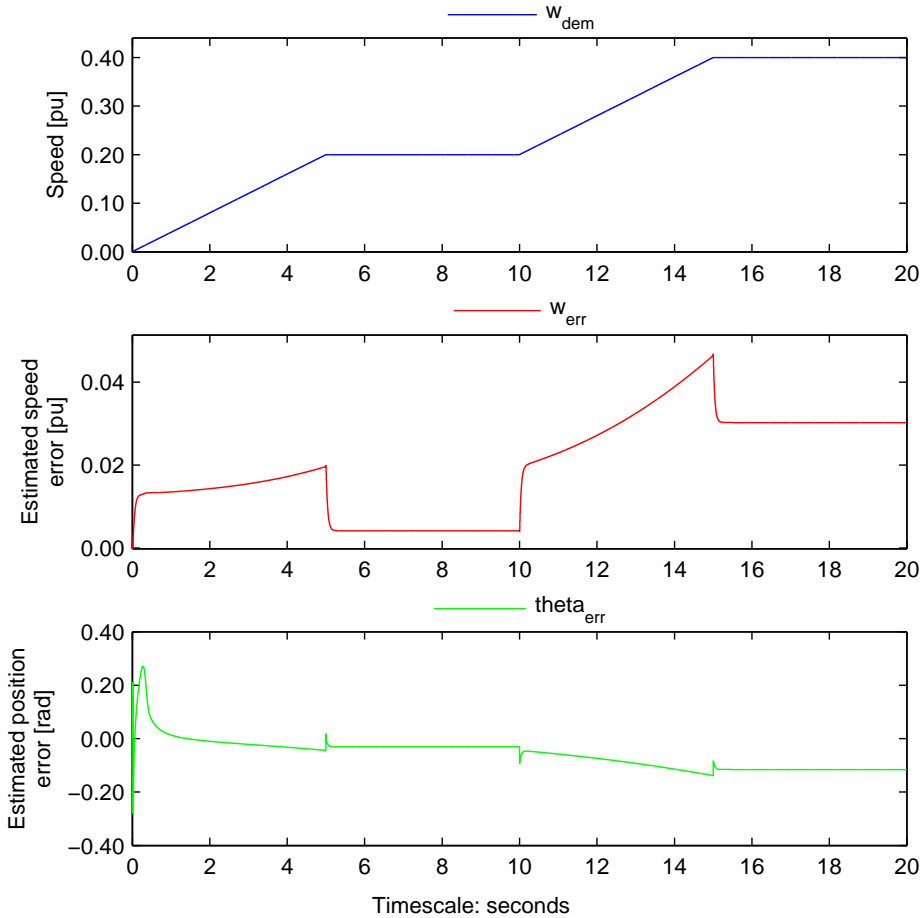


Figure 6.34: Vector control simulation measurements - Speed demand and estimated speed and position errors - Test case, 20 sec simulation time

Figure 6.34 shows the speed reference used by the vector controller along with the estimated speed and position errors.

As seen from the figure, the errors in the estimated speed and position are very little and

changes along with the speed variations.

EKF with FL

FL is then implemented on the EKF in order to do online covariance matrix updating. In order to test this setup, the same procedure as the previous simulation is performed.

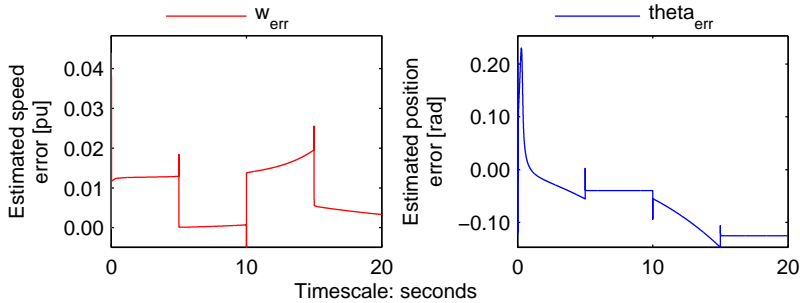


Figure 6.35: Vector control simulation measurements - Speed demand and estimated speed and position errors - Test case, 20 sec simulation time

Figure 6.35 shows the estimated speed and position errors.

As seen from the figure, the errors in the estimated speed and position are comparable to the ones presented in **Figure 6.34**. This means that covariance matrix design can be done without trial and error.

Additionally, it can also be observed that the errors is a little bit better than the ones presented in **Figure 6.34**. This is due to the online updating of the covariance matrices. Theoretically, the performance of the position estimator will get better over time as the FL controller updates the covariance matrices. This has not been proven via simulation as the simulation speed drastically goes down over time, due to lack of computing memory.

Response to a different initial rotor position

The initial rotor position is varied in order to see the response and performance of the position estimator.

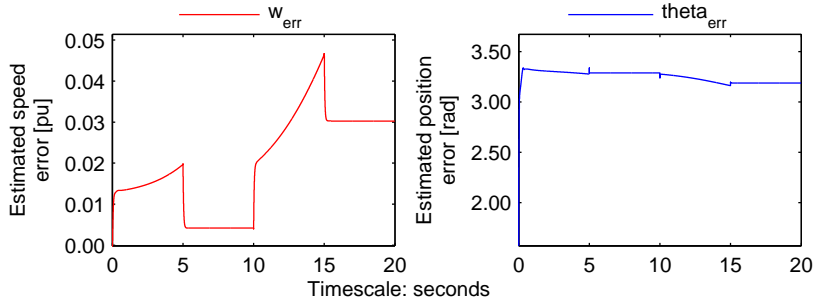


Figure 6.36: Vector control simulation measurements - Speed demand and estimated speed and position errors - Test case, 90 degrees initial rotor position, 20 sec simulation time

Figure 6.36 shows the estimated speed and position errors, when the initial rotor position is set to 90 degrees.

As seen from the figure, the speed error is the same as the ones in **Figure 6.35**. However, the position error is extremely high. This is as expected since the initial rotor position is an input parameter to the EKF.

Discussion

This chapter discusses the simulation results and other relevant elements of the study.

PMSM modelling

While doing this study, the only PMSM model available in Simulink is a Model 1.0 which has no damper windings. Additionally it assumes that the system always is balanced. Mathworks has been informed about this, but no replies have been received.

However, the new PMSM models established in Simulink works as intended and are able to simulate during unbalanced system operations.

Load modelling

While doing the fall project [8], a load model with a step function for the breakaway friction has been used, in order to simplify the simulation. This resulted to an easy start-up of the motor.

The simulation results of this study shows that accurate load modelling affects the start-up procedure, as additional torque is required due to more rotational friction components. This is discussed in section 2.8.

Motor start-up's dependency on damping

The simulation results show that adding damping to the system, be it via transmission system components or motor damper windings damps small system disturbances, which consequently either lessens or eliminates rotor angle instability. Rotor angle instability in the PMSM risks it to lose synchronism. Therefore, adding enough damping to the system ensures that the PMSM not to loose its synchronization all throughout the speed range.

Motor start-up's dependency on breakaway torque

The simulation results show that the torque oscillations experienced during start-up is directly affected by the breakaway torque. Additional torque oscillations can be experienced if the breakaway torque is too high due to the reduced torque build up, which consequently makes the start-up time higher. This is described by equation (3.1).

Motor start-up's dependency on reference frequency slope

The simulation results show that the start-up time decreases rapidly as the frequency ramp slope is initially increased at lower values, and flats out at the higher values.

Additionally, too low reference frequency slope causes unnecessary oscillations due to the reduced torque build up, which consequently makes the start-up time higher. Too high reference frequency slope on the other hand causes the PMSM to lose stability and thus its synchronization in certain speed ranges, for scalar control schemes.

Open-loop scalar controller using constant voltage boosting

The simulation results show that the proposed open-loop scalar control scheme using constant voltage boosting is able to start-up the PMSM successfully, regardless of the initial rotor position.

However, stability is not guaranteed at certain speed ranges due to small system disturbances. This is eliminated by adding enough damping to the system as discussed earlier, and as shown via simulation results.

Additionally, during the start-up procedure, due to calculation assumption that the stator current is constant equals to rated current all throughout the frequency range, the required voltage across the PMSM terminals are not met. Consequently this would mean that the PMSM enters over-excitation. The over-excitation is intensified with the inaccuracy of the voltage drop compensation algorithm. This causes high start-up currents.

Open-loop scalar controller using partial and delayed voltage boosting

The simulation results show that the proposed open-loop scalar control scheme using partial and delayed voltage boosting is able to start-up the PMSM successfully, regardless of the initial rotor position.

However, stability is still not guaranteed at certain speed ranges due to small system disturbances. This is eliminated by adding enough damping to the system as discussed earlier, and as shown via simulation results.

Simulation results also show that due to the correct assumption that the peak stator current is not constant throughout the whole frequency range, the required voltage across the PMSM terminals are met during initial start-up, by adjusting the border frequency. Consequently, this results to low start-up currents.

However, after the border frequency is reach and the voltage calculation slope is changed the required voltage across the PMSM terminals are not met. Consequently this would mean that the PMSM enters over-excitation during that period.

Adjusting the border frequency shapes the reference voltage signal. Decreasing border frequency too much causes oscillatory behaviour to reappear, as well as enabling the breakaway torque to be achieved earlier due to the higher volts per hertz ratio.

Closed-loop scalar controller

The simulation results show that the proposed closed-loop scalar control scheme is able to start-up the PMSM successfully, regardless of the initial rotor position.

However, stability is still not guaranteed at certain speed ranges due to small system disturbances. This is eliminated by adding enough damping to the system as discussed earlier, and as shown via simulation results. If additional damping is not available or not enough, the established stabilization loop can be used to modulate the frequency of the machine, thus stabilizing the system for the whole applied frequency range.

Simulation results show that since the actual stator current is measured, the required voltage across the PMSM terminals are met all throughout the start-up procedure, which consequently results to low start-up currents.

Moreover, the controller is able to fulfil the speed demands with some overshoot and initial torque oscillations when the rate of change of the speed command is changed. A huge change in the speed command or the applied load will cause too much torque oscillations which will consequently make the motor go out of synchronization. This is discussed in section 2.5.

Scalar control schemes and long cable lengths

The simulation results show that the deviation from the required motor voltage is very low during start-up for both of the proposed open-loop scalar control scheme, and zero for the closed-loop scalar control scheme. This is due to the different voltage reference calculation algorithms used.

As the applied frequency is increased after the start-up procedure, the voltage deviation increases as well. The increase in voltage deviation is more significant in longer cables than shorter cables.

The voltage deviation that is observed during the simulations is due to the lack of transmission system voltage drop calculation accuracy. For longer cables, the higher equivalent capacitive line charging current causes a higher voltage drop across the line inductance that is in phase with the sending end voltage, which consequently increases receiving end voltage.

Assuming that the maximum allowed voltage deviation from the required motor voltage during steady state is 0.1 pu, the longest cable length that can be used with the proposed scalar control schemes is 40 km. An exception is the open-loop scalar control scheme using constant voltage boosting, which can be used for cable lengths up to 20 km, due to its inaccurate calculation assumptions as discussed earlier.

Vector controller

The simulation results show that the controller is able to start-up and fulfil the speed demands with very little overshoot, even during step changes of the reference speed. This

is due to the precise control of the rotor field.

Therefore, it can be stated that this control strategy provides high torque quality at all speed ranges. The drawbacks are increased complexity due to the current and speed regulators, and the requirement of position and speed measurement.

Position estimation using EKF

The simulation results shows that the EKF is able to estimated speed and position with very little error. The amount of estimation error changes along with speed variations.

Implementing FL in order to design the covariance matrices without trial and error, and to do online covariance matrix updating is possible, as shown by simulation results.

Additionally, simulation results show that initial rotor position is required by the EKF algorithm in order to predict position properly.

Comments on start-up procedure and time

Simulation results show that the vector control scheme offers the lowest possible start time due to its high performance. However, due to the requirement of initial rotor position of the sensorless vector controller, it can not be used during start-up, due to inaccuracies of predicting rotor position at zero speed [4, 5, 6, 7].

Based from the simulation results, the most viable start-up control schemes are either the partial and delayed open-loop scalar control scheme or the closed-loop scalar control scheme; as both control schemes offer low start-up currents and comparably low start-up times.

Transformer sizing and saturation

The start-up and full load currents obtained during the simulations can be used to correctly design the transformer to withstand the maximum flux density, as described by equation (2.82).

The voltage drop on the transformer secondary due to the start-up currents can be calculated and evaluated, along with the motor full load current to determine the transformer size.

Conclusion

This study produced two PMSM Simulink models, an accurate pump load Simulink model, and three scalar control schemes which includes transmission system components for their control algorithms. In addition, a vector control scheme using FOC and EKF for position estimation has been evaluated.

PMSM and load models

The two new PMSM Simulink models works as intended and are able to simulate during unbalanced system operations. This is an improvement to the currently available Simulink which has no damper windings and assumes that the system always is balanced.

The simulation results using the implemented pump load Simulink model shows that accurate load modelling affects the start-up procedure, as additional torque is required due to more rotational friction components.

Scalar control schemes

The simulation results show that the three proposed scalar control methods all are able to start-up the PMSM successfully, regardless of the initial rotor position. However, stability is not guaranteed at certain speed ranges due to the rise of small system disturbances.

The proposed open-loop scalar control scheme using constant voltage boosting causes inaccuracy in calculating the actual required voltage across the PMSM terminals. This causes PMSM over-excitation which leads to rise in start-up current, which in turn causes amplified electromagnetic torque oscillations. The over-excitation is intensified with the inaccuracy of the voltage drop compensation algorithm. Consequently, this start-up behaviour may cause excessive overheating of the motor during start-up which is unwanted. Additionally, the high start-up current will result to unwanted oversized transformers.

The proposed open-loop scalar control scheme using partial and delayed voltage boosting is a good compromise if closed loop control is not viable. The correct assumption that the peak stator current is not constant all throughout the frequency range leads to approximately correct calculation of the voltage across the PMSM terminals during initial start-up. This leads to little oscillations, and low start-up currents. Unwanted start-up behaviours caused by increase in load torque can easily be solved by changing the border frequency. It is

observed that the motor still enters over-excitation after the border frequency is reached. The dimensioning parameter for the transformers used in the transmission system will be the highest volts per hertz ratio which occurs before the border frequency.

The proposed closed-loop scalar controller gave the best start-up behaviour due to its precise voltage calculation. Using this control method, the motor is able to start-up with almost negligible oscillations and little start-up current. This control scheme allows the lowest possible voltage boosting while achieving the maximum possible starting torque, which will consequently affect the dimensioning of the transformer. Stability throughout the entire applied frequency range can be guaranteed through the established stabilization loop, which achieves this through frequency modulation. Moreover, the controller is able to fulfil the speed demands with little overshoot and initial torque oscillations when the rate of change of the speed command is changed. However, a large change in the speed command or the applied load will cause too much torque oscillations which will consequently make the motor go out of synchronization.

Vector control scheme and EKF

The vector controller gave the best performance during load step tests due to its precise control of the rotor field. However, due to the requirement of rotor position feedback, position estimation is required. The investigated position estimation technique, EKF is able to estimate speed and position with very little error. However, the initial rotor position is required by the EKF algorithm in order to predict states properly.

Input parameter dependencies

The study also investigated how input parameters affect the start-up sequence and the steady state behaviour of a PMSM.

The simulation results show that the torque oscillations experienced during start-up is directly affected by the breakaway torque. Additional torque oscillations can be experienced if the breakaway torque is too high due to the reduced torque build up, which consequently makes the start-up time higher.

The reference frequency ramp slope on the other hand directly affects the start-up time. The simulation results show that the start-up time decreases rapidly as the frequency ramp slope is initially increased at lower values, and flats out at the higher values. The high start-up times experienced during low reference frequency slopes are caused by unnecessary oscillations due to the reduced torque build up. Too high reference frequency slope on the other hand causes the PMSM to lose stability and thus its synchronization in certain speed ranges, for scalar control schemes.

The cable length determines the accuracy of the voltage compensation algorithms of the proposed scalar control schemes. The simulation results show that the deviation from the required motor voltage is very low during start-up for both of the proposed open-loop scalar control scheme, and zero for the closed-loop scalar control scheme. As the applied frequency is increased after the start-up procedure, the voltage deviation increases as well.

The increase in voltage deviation is more significant in longer cables than shorter cables. This is due to the higher equivalent capacitive line charging current present in longer cables, which causes a higher voltage drop across the line inductance that is in phase with the sending end voltage, which consequently increases receiving end voltage. In order to properly compensate for this increase in voltage, capacitive terms must be included in the scalar control algorithms.

Assuming that the maximum allowed voltage deviation from the required motor voltage during steady state is 0.1 pu, the longest cable length that can be used with the proposed scalar control schemes is 40 km. An exception is the open-loop scalar control scheme using constant voltage boosting, which can be used for cable lengths up to 20 km, due to its inaccurate calculation assumptions as discussed earlier.

Lastly, adding damping to the system, be it via transmission system components or motor damper windings damps small system disturbances, which ensures that the PMSM will not to lose its synchronization all throughout the speed range.

Start-up procedure and time

Due to the requirement of initial rotor position of the sensorless vector controller, it can not be used during start-up, due to inaccuracies of predicting rotor position at zero speed. Based from the simulation results, the most viable start-up control schemes are either the partial and delayed open-loop scalar control scheme or the closed-loop scalar control scheme; as both control schemes offer low start-up currents and comparably low start-up times. The vector controller can then be implemented after the start-up using the selected scalar control scheme, once the error in the estimated position is low; in order to obtain the optimal controller performance.

Recommendation for further work

Following are the tasks that can be done for further work:

- Include capacitive terms in the scalar control algorithms in order to perfectly compensate the transmission system voltage drop.
- Calculation of the required voltage boost of the transformers if the proposed scalar control schemes are used during start-up.
- Inclusion of the transmission system in the vector control scheme.
- Evaluation of flux generated in the transformers during start-up.
- Evaluation of required transformer boosting as a function of cable length using the different proposed scalar control schemes.
- Find out the sensitivity of the discussed rotor position estimation methods to saturation and voltage unbalance situations.
- Investigate convergence of the EKF at saturation and low speed.
- Review of methods to find out the initial rotor position of the PMSM.
- Corresponding laboratory setup for tests and verification of simulation analysis results.

Bibliography

- [1] S. Demmig, J. Andrews, and R.-D. Klug, "Control of subsea motors on multi-km cable lengths by variable frequency drives," in *Petroleum and Chemical Industry Conference Europe Conference Proceedings (PCIC EUROPE), 2011*, pp. 1–10, 2011.
- [2] Z. Xiwei, L. Weiguo, D. Manfeng, and L. Baohua, "A novel high power density asynchronous motor adjustable speed drive system design," in *Industrial Electronics and Applications, 2007. ICIEA 2007. 2nd IEEE Conference on*, pp. 1794–1797, 2007.
- [3] R. Gobbi, J. Sa'diah, and T. Siang, "Industrial problems in design, selection and installation of an adjustable speed drives (asd) for asynchronous motor," in *Power Engineering Conference, 2003. PECon 2003. Proceedings. National*, pp. 139–143, 2003.
- [4] B.-H. Bae, S.-K. Sul, J.-H. Kwon, and J.-S. Byeon, "Implementation of sensorless vector control for super-high-speed pmsm of turbo-compressor," *Industry Applications, IEEE Transactions on*, vol. 39, no. 3, pp. 811–818, 2003.
- [5] P. Kshirsagar, R. Burgos, J. Jang, A. Lidozzi, F. Wang, D. Boroyevich, and S.-K. Sul, "Implementation and sensorless vector-control design and tuning strategy for smpm machines in fan-type applications," *Industry Applications, IEEE Transactions on*, vol. 48, no. 6, pp. 2402–2413, 2012.
- [6] G. Zhu, A. Kaddouri, L.-A. Dessaint, and O. Akhrif, "A nonlinear state observer for the sensorless control of a permanent-magnet ac machine," *Industrial Electronics, IEEE Transactions on*, vol. 48, no. 6, pp. 1098–1108, 2001.
- [7] D. Paulus, J.-F. Stumper, and R. Kennel, "Sensorless control of synchronous machines based on direct speed and position estimation in polar stator-current coordinates," *Power Electronics, IEEE Transactions on*, vol. 28, no. 5, pp. 2503–2513, 2013.
- [8] K. Baricuatro, "Sensorless start-up of permanent magnet synchronous motor with long tie-back," 2013.
- [9] J. Pyrhonen, *Compendium in Electrical Drives, Permanent Magnet Synchronous Motor chapter*. https://noppa.lut.fi/noppa/opintojakso/bl30a1001/luennot/kaytto9_en.pdf.
- [10] B. Monsen, K. Rongve, T. Laegreid, and C. Gutscher, "Asgard subsea gas compression - technology qualification testing with high-speed vsd and very long step-out cable," in *Petroleum and Chemical Industry Technical Conference (PCIC), 2012 Record of Conference Papers Industry Applications Society 59th Annual IEEE*, pp. 1–10, 2012.

-
- [11] IEA, “Key world energy statistics 2012,” p. 30, 2012.
- [12] T. Brinner, R. McCoy, and T. Kopecky, “Induction versus permanent-magnet motors for electric submersible pump field and laboratory comparisons,” *Industry Applications, IEEE Transactions on*, vol. 50, pp. 174–181, Jan 2014.
- [13] MathWorks, *Simulink*. <http://www.mathworks.se/products/simulink/>.
- [14] MathWorks, *Simscape*. <http://www.mathworks.se/products/simscape/>.
- [15] MathWorks, *Simulink SimPowerSystems*. <http://www.mathworks.se/products/simpower/>.
- [16] N. Mohan, *Advanced electric drives : analysis, control and modeling using Simulink / Ned Mohan*. Minneapolis : MNPERE, 2001. Includes bibliographical references and index.
- [17] P. Kundur, *Power System Stability and Control*. 2006.
- [18] C. Ong, *Dynamic Simulation of Electric Machinery: Using Matlab/Simulink*. Prentice Hall PTR, 1998.
- [19] B. K. Bose, *Power electronics and variable frequency drives : technology and applications*. 1997.
- [20] F. Korkmaz, I. Topaloglu, M. Cakir, and R. Gurbuz, “Comparative performance evaluation of foc and dtc controlled pmsm drives,” in *Power Engineering, Energy and Electrical Drives (POWERENG), 2013 Fourth International Conference on*, pp. 705–708, May 2013.
- [21] S. Chapman, *Electric machinery fundamentals*. 1998.
- [22] K. Rajashekara, A. Kawamura, and K. Matsuse, *Sensorless Control of Ac Motor Drives: Speed and Position Sensorless Operation*. A selected reprint series, IEEE Press, 1996.
- [23] R. Wu and G. Slemon, “A permanent magnet motor drive without a shaft sensor,” in *Industry Applications Society Annual Meeting, 1990., Conference Record of the 1990 IEEE*, pp. 553–558 vol.1, Oct 1990.
- [24] T.-H. Liu and C.-P. Cheng, “Adaptive control for a sensorless permanent-magnet synchronous motor drive,” in *Industrial Electronics, Control, Instrumentation, and Automation, 1992. Power Electronics and Motion Control., Proceedings of the 1992 International Conference on*, pp. 413–418 vol.1, Nov 1992.
- [25] T. H. Liu and C.-P. Cheng, “Controller design for a sensorless permanent-magnet synchronous drive system,” *Electric Power Applications, IEE Proceedings B*, vol. 140, pp. 369–378, Nov 1993.
- [26] M. Naidu and B. Bose, “Rotor position estimation scheme of a permanent magnet synchronous machine for high performance variable speed drive,” in *Industry Applications Society Annual Meeting, 1992., Conference Record of the 1992 IEEE*, pp. 48–53 vol.1, Oct 1992.

-
- [27] N. Ertugrul and P. Acarnley, "A new algorithm for sensorless operation of permanent magnet motors," *Industry Applications, IEEE Transactions on*, vol. 30, pp. 126–133, Jan 1994.
- [28] N. Matsui and M. Shigyo, "Brushless dc motor control without position and speed sensors," in *Industry Applications Society Annual Meeting, 1990., Conference Record of the 1990 IEEE*, pp. 448–453 vol.1, Oct 1990.
- [29] N. Matsui, T. Takeshita, and K. Yasuda, "A new sensorless drive of brushless dc motor," in *Industrial Electronics, Control, Instrumentation, and Automation, 1992. Power Electronics and Motion Control., Proceedings of the 1992 International Conference on*, pp. 430–435 vol.1, Nov 1992.
- [30] N. Matsui, "Sensorless operation of brushless dc motor drives," in *Industrial Electronics, Control, and Instrumentation, 1993. Proceedings of the IECON '93., International Conference on*, pp. 739–744 vol.2, Nov 1993.
- [31] H. Watanabe, H. Katsushima, and T. Fujii, "An improved measuring system of rotor position angles of the sensorless direct drive servomotor," in *Industrial Electronics, Control and Instrumentation, 1991. Proceedings. IECON '91., 1991 International Conference on*, pp. 165–170 vol.1, Oct 1991.
- [32] R. Dhaouadi, N. Mohan, and L. Norum, "Design and implementation of an extended kalman filter for the state estimation of a permanent magnet synchronous motor," *Power Electronics, IEEE Transactions on*, vol. 6, pp. 491–497, Jul 1991.
- [33] A. Bado, S. Bolognani, and M. Zigliotto, "Effective estimation of speed and rotor position of a pm synchronous motor drive by a kalman filtering technique," in *Power Electronics Specialists Conference, 1992. PESC '92 Record., 23rd Annual IEEE*, pp. 951–957 vol.2, Jun 1992.
- [34] B.-J. Brunsbach, G. Henneberger, and T. Klepsch, "Position controlled permanent excited synchronous motor without mechanical sensors," in *Power Electronics and Applications, 1993., Fifth European Conference on*, pp. 38–43 vol.6, Sep 1993.
- [35] G. Zhu, A. Kaddouri, L.-A. Dessaint, and O. Akhrif, "A nonlinear state observer for the sensorless control of a permanent-magnet ac machine," *Industrial Electronics, IEEE Transactions on*, vol. 48, pp. 1098–1108, Dec 2001.
- [36] L. Jones and J. H. Lang, "A state observer for the permanent-magnet synchronous motor," *Industrial Electronics, IEEE Transactions on*, vol. 36, pp. 374–382, Aug 1989.
- [37] S. Shinnaka, "New sensorless vector control using minimum-order flux state observer in a stationary reference frame for permanent-magnet synchronous motors," *Industrial Electronics, IEEE Transactions on*, vol. 53, pp. 388–398, April 2006.
- [38] G. Zhu, L.-A. Dessaint, O. Akhrif, and A. Kaddouri, "Speed tracking control of a permanent-magnet synchronous motor with state and load torque observer," *Industrial Electronics, IEEE Transactions on*, vol. 47, pp. 346–355, Apr 2000.
-

-
- [39] J. F. Moynihan, M. Egan, and J. M. D. Murphy, "The application of state observers in current regulated pm synchronous drives," in *Industrial Electronics, Control and Instrumentation, 1994. IECON '94., 20th International Conference on*, vol. 1, pp. 20–25 vol.1, Sep 1994.
- [40] K. J. Binns, D. W. Shimmin, and K. M. Al-Aubidy, "Implicit rotor-position sensing using motor windings for a self-commutating permanent-magnet drive system," *Electric Power Applications, IEE Proceedings B*, vol. 138, pp. 28–34, Jan 1991.
- [41] A. Kulkarni and M. Ehsani, "A novel position sensor elimination technique for the interior permanent-magnet synchronous motor drive," in *Industry Applications Society Annual Meeting, 1989., Conference Record of the 1989 IEEE*, pp. 773–779 vol.1, Oct 1989.
- [42] H. Olsson, K. Åström, C. C. de Wit, M. Gäfvert, and P. Lischinsky, "Friction models and friction compensation," *European Journal of Control*, vol. 4, no. 3, pp. 176 – 195, 1998.
- [43] D. Jiles, *Introduction to Magnetism and Magnetic Materials*. CRC Press, 1998.
- [44] A. E. Fitzgerald, *Electric Machinery*. A.E. Fitzgerald, Charles Kingsley, JR., Stephen D. Umans. McGraw-Hill, 6th ed.
- [45] R. Gobbi, J. Sa'diah, and T. Siang, "Industrial problems in design, selection and installation of an adjustable speed drives (asd) for asynchronous motor," pp. 139–143, 2003.
- [46] S. Casoria, G. Sybille, and P. Brunelle, "Hysteresis modeling in the matlab/power system blockset," *Mathematics and Computers in Simulation*, vol. 63, no. 3–5, pp. 237 – 248, 2003.
- [47] R. Zaimeddine, *Private communication*. OneSubsea AS.
- [48] MathWorks, *Rotational friction discontinuity*. <http://www.mathworks.se/help/physmod/simscape/ref/rotationalfriction.html>.
- [49] P. Perera, F. Blaabjerg, J. Pedersen, and P. Thogersen, "A sensorless, stable v/f control method for permanent-magnet synchronous motor drives," *Industry Applications, IEEE Transactions on*, vol. 39, no. 3, pp. 783–791, 2003.
- [50] H. Saadat, *Power System Analysis*. WCB/McGraw-Hill, 1999.
- [51] O. A. Mahgoub and S. A. Zaid, "Simulation study of conventional control versus mtpa-based for pmsm control,"
- [52] P. D. W. V. A. De Doncker, Rik, *Advanced Electrical Drives*. 2011.
- [53] J. Umland and M. Safiuddin, "Magnitude and symmetric optimum criterion for the design of linear control systems: what is it and how does it compare with the others?," *Industry Applications, IEEE Transactions on*, vol. 26, pp. 489–497, May 1990.

-
- [54] Y. Xiao-ling and W. Hong-hua, “Intelligent sensorless control of permanent magnet synchronous motor drive,” in *Intelligent Computation Technology and Automation, 2009. ICICTA '09. Second International Conference on*, vol. 2, pp. 454–457, Oct 2009.

Simulink model

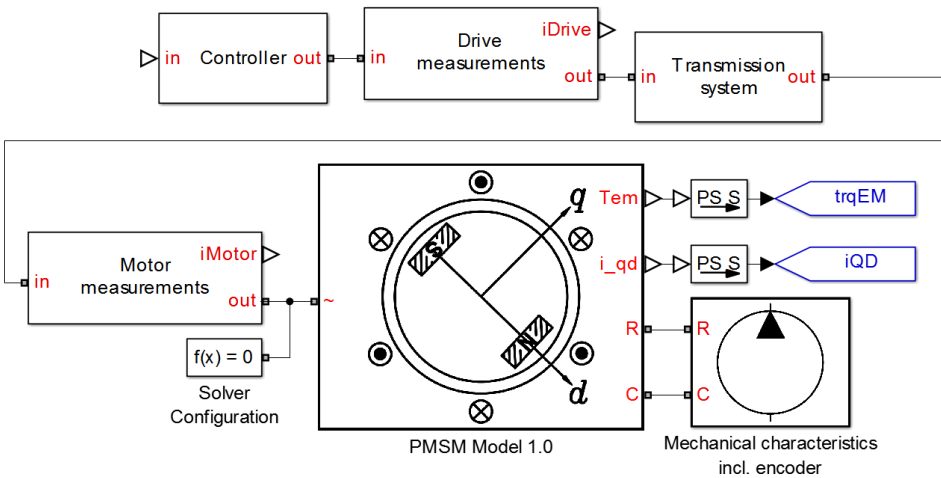


Figure A.1: Top-level Simulink model

The top-level Simulink model is shown in **Figure A.1**, consisting of three user-made subsystems as follows:

- PMSM
- Mechanical characteristics
- Transmission system
- Measurements
- Controller

These subsystems and its blocks are discussed in detail later in this appendix.

A.1 PMSM

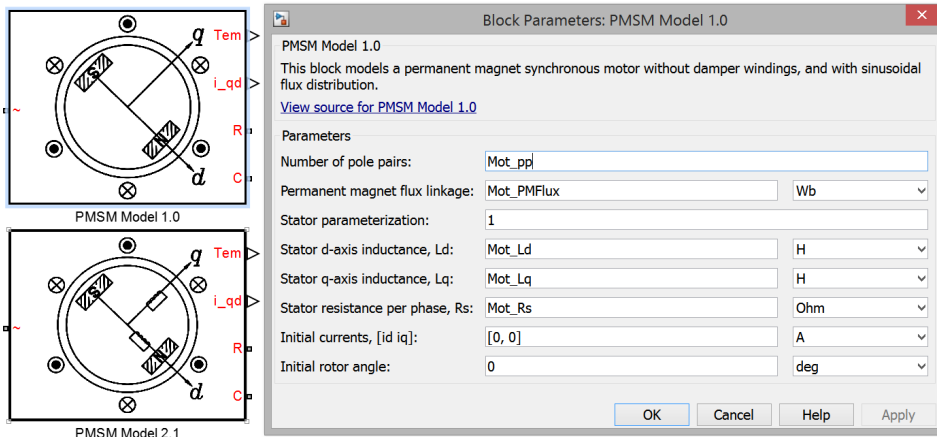


Figure A.2: PMSM Simulink models including model 1.0's mask

Two PMSM models have been developed in Simulink using Simscape language. The resulting blocks including one of the masks are shown in **Figure A.2**.

Model 1.0 implements a PMSM without damper windings while model 2.1 implements a PMSM with damper windings. These models are based on the derived equations in sections 2.4.2 and 2.4.3.

The Simscape codes for model 1.0 are as follows:

```

1 component PMSM_Model_1_0
2 % PMSM Model 1.0 : 1 : fixed
3 % This block models a permanent magnet synchronous motor
  without damper
4 % windings, and with sinusoidal flux distribution.
5
6 % Kristiansen Baricuatro
7 % 15.02.2014
8
9 parameters
10     nPolePairs = {6, '1'}; % Number of pole pairs
11     pm_flux_linkage = {0.03, 'Wb'}; % Permanent magnet
      flux linkage
12     stator_param = {1, '1'}; % Stator parameterization
13     Ld = {0.00025, 'H'}; % Stator d-axis inductance, Ld
14     Lq = {0.00019, 'H'}; % Stator q-axis inductance, Lq
15     Rs = {0.013, 'Ohm'}; % Stator resistance per phase,
      Rs

```

```

16     initial_currents = {[0 0], 'A'}; % Initial currents
17     , [id iq]
18     angular_position0 = {0, 'deg'}; % Initial rotor
19     angle
20 end
21 parameters (Hidden=true)
22     shift_3ph = { [0, -2*pi/3, 2*pi/3], 'rad' };
23     mat = { [1/2, 1/2, 1/2], '1' };
24 end
25 outputs
26     torque_out = { 0, 'N*m' }; % Tem:right
27     iqd_out = { [0 0], 'A' }; % i_qd:right
28 end
29 nodes
30     N = pe.electrical.three_phase.electrical; % ~:left
31     R = foundation.mechanical.rotational.rotational; %
32     R:right
33     C = foundation.mechanical.rotational.rotational; %
34     C:right
35 end
36 variables
37     % d-axis and q-axis currents
38     i_d = {0, 'A'};
39     i_q = {0, 'A'};
40     i_0 = {0, 'A'};
41
42     % Line currents
43     I = {[0 0 0], 'A' };
44
45     % Mechanical variables
46     torque = {0, 'N*m' };
47     angular_position = {0, 'rad' };
48 end
49
50 function setup
51     % Initial conditions
52     i_d = initial_currents(1);
53     i_q = initial_currents(2);
54     angular_position = angular_position0;
55 end
56

```

```

57     branches
58         I      : N.I    -> *;
59         torque : R.t -> C.t;
60     end
61
62     equations
63         I(1)+I(2)+I(3) == 0;
64
65         let
66             angular_velocity = R.w - C.w;
67             electrical_angle = nPolePairs*angular_position;
68
69             % Set up Park's transform
70             abc2dq = 2/3*[...
71                 cos( electrical_angle + shift_3ph );...
72                 sin( electrical_angle + shift_3ph );...
73                 mat];
74
75             % Voltages a,b,c -> d,q
76             vdq = abc2dq*N.V';
77             vq = vdq(1);
78             vd = vdq(2);
79             %v0 = vdq(3)
80
81             % Flux linkages
82             psid = i_d*Ld + pm_flux_linkage;
83             psiq = i_q*Lq;
84
85         in
86             % Electric to mechanical rotation
87             angular_velocity == angular_position.der;
88
89             % Electrical equations
90             vd == i_d*Rs + psid.der - nPolePairs*
91                 angular_velocity*psiq;
92             vq == i_q*Rs + psiq.der + nPolePairs*
93                 angular_velocity*psid;
94             [ i_q; i_d; i_0 ] == abc2dq*I';
95
96             % Mechanical torque
97             torque == -3/2*nPolePairs*(i_q*psid - i_d*psiq)
98                 ;
99             torque_out == - torque;
100            iqd_out == [i_q, i_d];
101
102     end

```

```
99     end
```

```
100
```

```
101 end
```

The Simscape codes for model 1.0 are as follows:

```
1 component PMSM_Model_2_1
2 % PMSM Model 2.1 : 1 : fixed
3 % This block models a permanent magnet synchronous motor
  with damper
4 % circuits in both q and d axes, and with sinusoidal flux
  distribution.
5
6 % Kristiansen Baricuatro
7 % 23.02.2014
8
9     parameters
10         nPolePairs = {6, '1'}; % Number of pole pairs
11         pm_flux_linkage = {0.03, 'Wb'}; % Permanent magnet
          flux linkage
12         stator_param = {1, '1'}; % Stator parameterization
13         Ld = {0.00025, 'H'}; % Stator d-axis inductance, Ld
14         Lq = {0.00019, 'H'}; % Stator q-axis inductance, Lq
15         Lls = {0.00019, 'H'}; % Stator winding leakage
          inductance, Lls
16         Rs = {0.013, 'Ohm'}; % Stator resistance per phase,
          Rs
17         Lp_kdkd = {0.00025, 'H'}; % Damper winding d-axis
          self-inductance, L'kd
18         Lp_kkqkq = {0.00019, 'H'}; % Damper winding q-axis
          self-inductance, L'kq
19         Lp_lkd = {0.00025, 'H'}; % Damper winding d-axis
          leakage inductance, L'kd
20         Lp_lkq = {0.00019, 'H'}; % Damper winding q-axis
          leakage inductance, L'kq
21         rp_kd = {0.013, 'Ohm'}; % Damper winding d-axis
          resistance, r'kd
22         rp_kq = {0.013, 'Ohm'}; % Damper winding q-axis
          resistance, r'kq
23         initial_currents = {[0 0], 'A'}; % Initial currents
          , [id iq]
24         angular_position0 = {0, 'deg'}; % Initial rotor
          angle
25     end
26
27     parameters (Hidden=true)
28         shift_3ph = { [0, -2*pi/3, 2*pi/3], 'rad' };
```

```

29     mat = { [1/2,1/2,1/2], '1' };
30 end
31
32 outputs
33     torque_out = { 0, 'N*m' }; % Tem:right
34     iqd_out = { [0 0], 'A' }; % i_qd:right
35 end
36
37 nodes
38     N = pe.electrical.three_phase.electrical; % ~:left
39     R = foundation.mechanical.rotational.rotational; %
40         R:right
41     C = foundation.mechanical.rotational.rotational; %
42         C:right
43 end
44
45 variables
46     % d-axis and q-axis currents
47     i_d = {0, 'A'};
48     i_q = {0, 'A'};
49     i_0 = {0, 'A'};
50
51     % damper windings currents
52     ip_kd = {0, 'A'};
53     ip_kq = {0, 'A'};
54
55     % Line currents
56     I = {[0 0 0], 'A' };
57
58     % Mechanical variables
59     torque = {0, 'N*m' };
60     angular_position = {0, 'rad' };
61
62     % Inductances
63     Lmd = {0, 'H'};
64     Lmq = {0, 'H'};
65 end
66
67 function setup
68     % Initial conditions
69     i_d = initial_currents(1);
70     i_q = initial_currents(2);
71     angular_position = angular_position0;
72
73     % Constants
74     Lmd = Ld - Lls;

```

```

72     Lmq = Lq - Lls;
73     end
74
75     branches
76         I      : N.I -> *;
77         torque : R.t -> C.t;
78     end
79
80     equations
81         I(1)+I(2)+I(3) == 0;
82
83     let
84         angular_velocity = R.w - C.w;
85         electrical_angle = nPolePairs*angular_position;
86
87         % Set up Park's transform
88         abc2dq = 2/3*[...
89             cos( electrical_angle + shift_3ph );...
90             sin( electrical_angle + shift_3ph );...
91             mat];
92
93         % Voltages a,b,c -> d,q
94         vdq = abc2dq*N.V';
95         vq = vdq(1);
96         vd = vdq(2);s
97         %v0 = vdq(3)
98
99         % dq Flux linkages
100        psid = i_d*Ld + Lmd*ip_kd + pm_flux_linkage;
101        psiq = i_q*Lq + Lmq*ip_kq;
102
103        % Damper winding dq flux linkages
104        psip_kq = Lmq*i_q + Lp_kqkq*ip_kq;
105        psip_kd = Lmd*i_d + Lp_kdkd*ip_kd +
106            pm_flux_linkage;
107
108    in
109        % Electric to mechanical rotation
110        angular_velocity == angular_position.der;
111
112        % Electrical equations
113        vd == i_d*Rs + psid.der - nPolePairs*
114            angular_velocity*psiq;
115        vq == i_q*Rs + psiq.der + nPolePairs*
116            angular_velocity*psid;

```

```

114         0 == rp_kd*ip_kd + psip_kd.der;
115         0 == rp_kq*ip_kq + psip_kq.der;
116         [ i_q; i_d; i_0 ] == abc2dq*I';
117
118         % Mechanical torque
119         torque == -3/2*nPolePairs*(i_q*psid - i_d*psiq)
120         ;
121         torque_out == - torque;
122         iqd_out == [ i_q, i_d ];
123     end
124 end
125 end

```

A.2 Mechanical characteristics

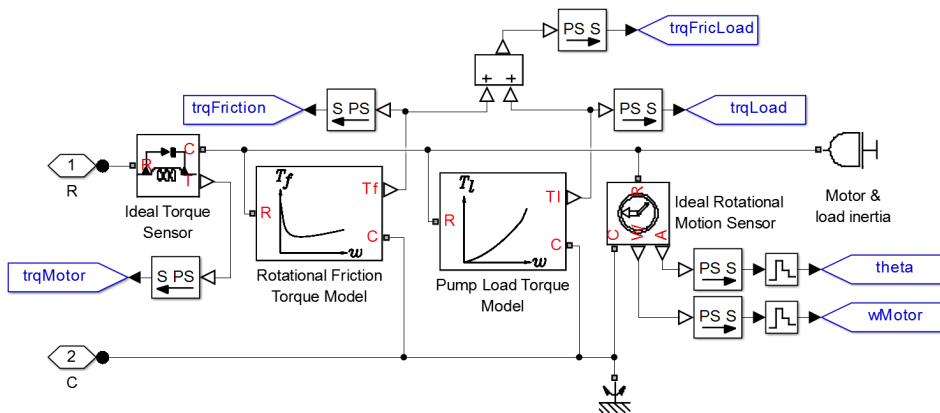


Figure A.3: Inside the mechanical characteristics block

Figure A.3 shows what is inside the mechanical characteristics block. Shown are the user-made rotational friction torque and pump load torque blocks. Also shown are the built-in Simulink sensors for measurement logging, and the built-in motor and load inertia block.

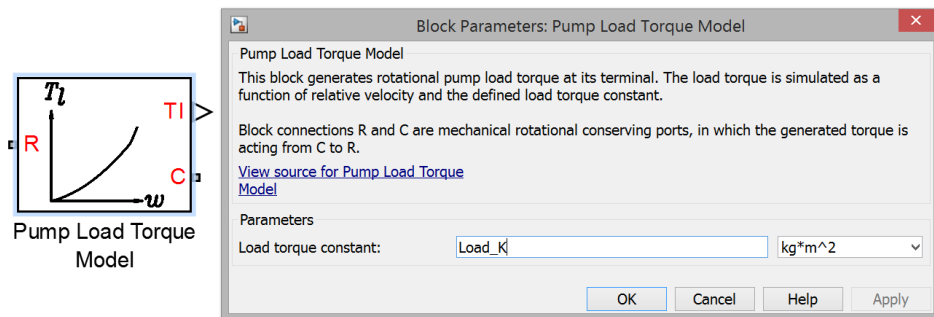


Figure A.4: Pump load torque block including its mask

Using equation (2.60), the Pump Load Torque block has been developed in Simulink using Simscape language. The resulting block including its mask is shown in **Figure A.4**. The Simscape codes for the block are as follows:

```

1 component Pump_Load_Model
2 % Pump Load Torque Model : 1 : fixed
3 % This block generates rotational pump load torque at its
4   terminal .
5 % The load torque is simulated as a function of relative
6   velocity and
7 % the defined load torque constant .
8 %
9 % Block connections R and C are mechanical rotational
10  conserving
11 % ports , in which the generated torque is acting from C to
12  R .
13
14 % Kristiansen Baricuatro
15 % 15.02.2014
16
17 parameters
18   alpha = { 25, 'kg*m^2' }; % Load torque constant
19 end
20
21 outputs
22   t_out = { 0, 'N*m' }; % Tl:right
23 end
24
25 nodes
26   R = foundation.mechanical.rotational.rotational; %
27     R:left
28   C = foundation.mechanical.rotational.rotational; %
29     C:right

```

```

24     end
25
26     variables
27         % Mechanical variables
28         torque = {0, 'N*m' };
29     end
30
31     branches
32         torque : C.t -> R.t;
33     end
34
35     equations
36         let
37             w = C.w - R.w;
38         in
39             torque == - alpha * w * w;
40             t_out == - torque;
41         end
42     end
43
44 end

```

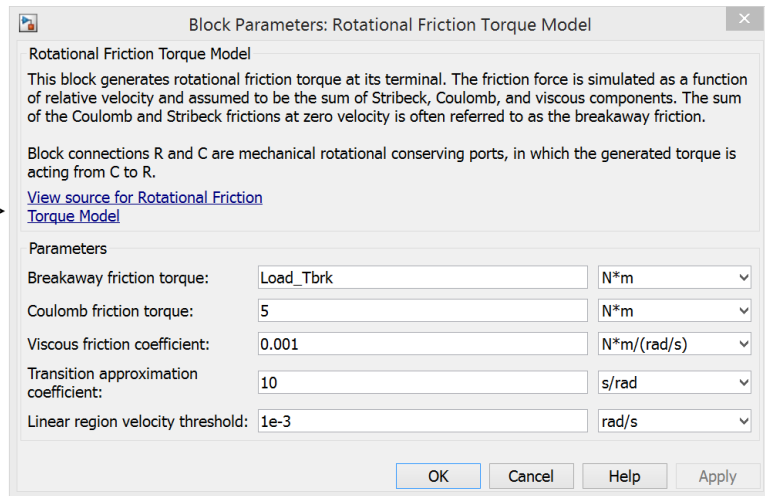
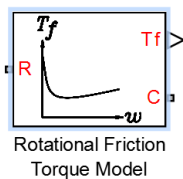


Figure A.5: Rotational friction torque block including its mask

Using equation (3.1), the Rotational Friction Torque block has been developed in Simulink using Simscape language. The resulting block including its mask is shown in **Figure A.5**. The Simscape codes for the block are as follows:

```

1 component Rotational_Friction_Torque
2 % Rotational Friction Torque Model : 1 : fixed
3 % This block generates rotational friction torque at its
  terminal.
4 % The friction force is simulated as a function of relative
  velocity and
5 % assumed to be the sum of Stribeck, Coulomb, and viscous
  components. The
6 % sum of the Coulomb and Stribeck frictions at zero
  velocity is often
7 % referred to as the breakaway friction.
8 %
9 % Block connections R and C are mechanical rotational
  conserving
10 % ports, in which the generated torque is acting from C to
  R.
11
12 % Kristiansen Baricuatro
13 % 15.02.2014
14
15     parameters
16         brkwy_trq = { 25, 'N*m' }; % Breakaway friction
          torque
17         Col_trq = { 20, 'N*m' }; % Coulomb friction torque
18         visc_coef = { 0.001, 'N*m*s/rad' }; % Viscous
          friction coefficient
19         trans_coef = { 10, 's/rad' }; % Transition
          approximation coefficient
20         vel_thr = { 1e-4, 'rad/s' }; % Linear region
          velocity threshold
21     end
22
23     parameters (Access=private)
24         brkwy_trq_th = { 24.995, 'N*m' }; % Breakaway
          torque at threshold velocity
25     end
26
27     outputs
28         t_out = { 0, 'N*m' }; % Tf:right
29     end
30
31     nodes
32         R = foundation.mechanical.rotational.rotational; %
          R:left
33         C = foundation.mechanical.rotational.rotational; %

```

```

34         C:right
35     end
36     variables
37         % Mechanical variables
38         torque = {0, 'N*m' };
39     end
40
41     function setup
42         % Parameter range checking
43         if brkwy_trq <= 0
44             pm_error('simscape:GreaterThanZero', 'Breakaway
45                 friction torque' )
46         end
47         if Col_trq <= 0
48             pm_error('simscape:GreaterThanZero', 'Coulomb
49                 friction torque' )
50         end
51         if Col_trq > brkwy_trq
52             pm_error('simscape:LessThanOrEqual', 'Coulomb
53                 friction torque', 'Breakaway friction torque'
54             )
55         end
56         if visc_coef < 0
57             pm_error('simscape:GreaterThanOrEqualToZero', '
58                 Viscous friction coefficient')
59         end
60         if trans_coef <= 0
61             pm_error('simscape:GreaterThanZero', 'Transition
62                 approximation coefficient')
63         end
64         if vel_thr <= 0
65             pm_error('simscape:GreaterThanZero', 'Linear
66                 region velocity threshold')
67         end
68
69         % Computing breakaway torque at threshold velocity
70         brkwy_trq_th = visc_coef * vel_thr + Col_trq + (
71             brkwy_trq - Col_trq) * ...
72             exp(-trans_coef * vel_thr);
73     end
74
75     branches
76         torque : C.t -> R.t;
77     end

```

```

70
71
72 equations
73     let
74         w = C.w - R.w;
75     in
76         if (abs(w) <= vel_thr)
77             % Linear region
78             torque == brkwy_trq_th * w / vel_thr;
79         else
80             torque == visc_coef * w + ...
81                 (Col_trq + (brkwy_trq - Col_trq) * exp
82                     (-trans_coef * abs(w))) * sign(w);
83         end
84     end
85 end
86
87 end

```

A.3 Transmission system

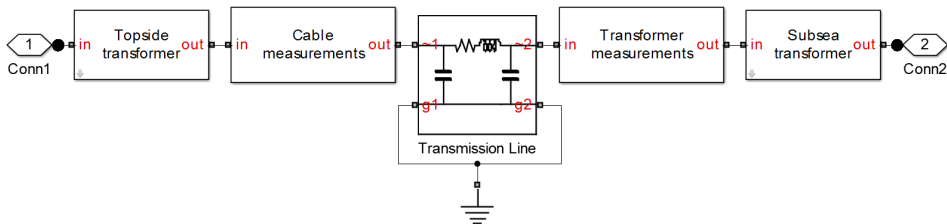


Figure A.6: Inside the transmission system block

Figure A.6 shows what is inside the transmission system block. Shown are the transformer and measurement subsystems. Also shown is the built-in Simulink SimPowerSystems "Transmission line" third generation block.

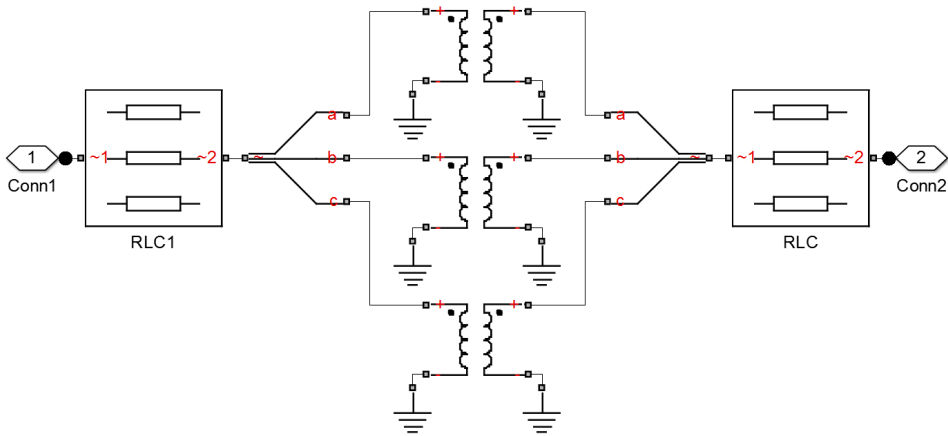


Figure A.7: Transformer subsystem

The linear model based on equations (2.62) - (2.68) can be implemented in Simulink by using the SimPowerSystem third generation blocks "Ideal Transformer" and "RLC". This is shown in **Figure A.7**.

A.4 Measurements

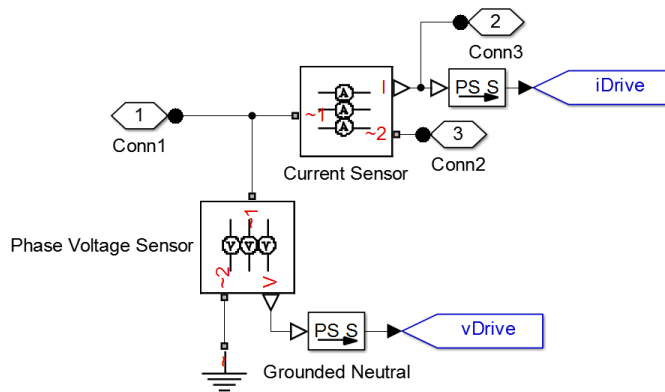


Figure A.8: Inside the measurement block

Figure A.8 shows what is inside the measurement block. These blocks are used to log current and voltage measurements using built-in Simulink sensors.

A.5 Controller

Simulink models of the controllers has been establish using equations derived in chapter 4 and chapter 5. The models are differentiated by their different control scheme and as follows:

- Open-loop scalar control
- Closed-loop scalar control
- Vector control

These models and their corresponding blocks are discussed in detail in the following sections.

A.5.1 Open-loop scalar controller

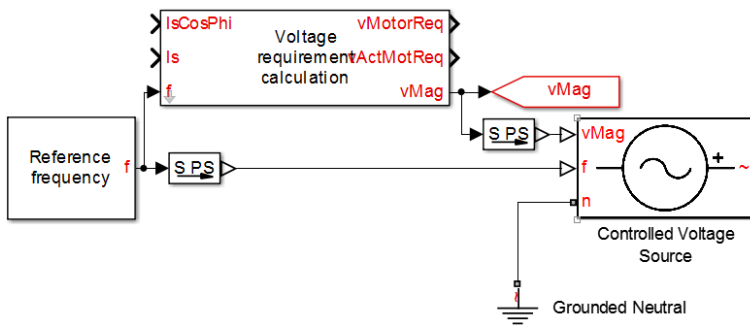


Figure A.9: Open-loop controller overview

Figure A.9 shows the top-level open-loop controller Simulink model, showing three user-made subsystems as follows:

- Reference frequency
- Voltage requirement calculation
- Controlled voltage source

These subsystems and its blocks are discussed in detail in the following sections.

Reference frequency

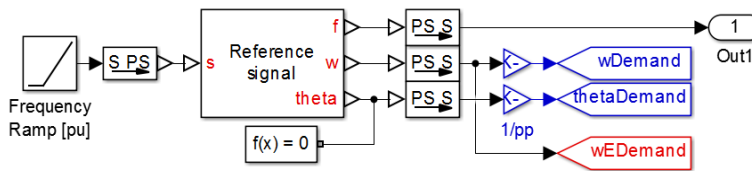


Figure A.10: Inside the reference frequency block

Figure A.10 shows the established reference frequency block.

The input signal is given by a ramp function. The slope of the frequency ramp, which determines the desired time it will take to accelerate from stand-still synchronous frequency is given by a parameter t_{acc} and is set via accompanying Matlab script.

The Simulink block "Repeating Sequence" can also be used as the input signal. This block will make it possible to control the speed demand as much as the study requires.

The reference signal block transforms the input signal to required output signals: frequency, angular speed and angular position. This block has been made using Simscape language with the following codes:

```

1 component Reference_Frequency
2 % Reference signal
3 % This block generates required output signals: frequency ,
4   angular speed
5 % and angular position based from input signal.
6 % Kristiansen Baricuatro
7 % 15.02.2014
8
9 parameters
10     fs = {100, 'Hz'}; % Synchronous frequency , fs
11 end
12
13 inputs
14     s = { 0, '1' }; % s:left
15 end
16
17 outputs
18     f = { 0, 'Hz' }; % f:right
19     w = { 0, 'rad/s' }; % w:right
20     theta = { 0, 'rad' }; % theta:right
21 end
22

```

```

23     equations
24         let
25             f_real = fs*s;
26         in
27             w == 2*pi*f_real;
28             f == f_real;
29             w == theta.der
30         end
31     end
32
33 end

```

Voltage requirement calculation

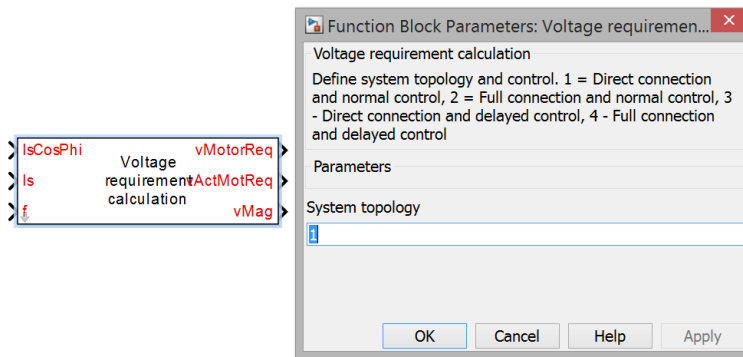


Figure A.11: Voltage requirement calculation block including its mask

The two open-loop scalar control schemes described in chapter 4 have been developed in Simulink within one block. The resulting block including its mask is shown in **Figure A.11**. Current measurement inputs are not used by the controller but are used for checking results.

Figure A.12 shows what is inside the voltage requirement calculation block.

In order to incorporate the two voltage amplitude calculation methods and the different cases discussed in the thesis, a multiport switch is used. This switch outputs the voltage amplitude calculated via function blocks through a control signal called "Top" which can be defined in the block mask.

To check results, the actual voltage requirement of the motor is calculated using equation (4.11).

All the input signals are fed through a saturation port in order to avoid discontinuities during the zero period. All the required signals and constants are combined into an array named "signals" in order to ease readability of the function blocks.

For the second calculation method, a switch is necessary due to the different voltage equations used before and after the border frequency f_b . The border frequency f_b and the constant $Fb2$ is defined via accompanying Matlab script.

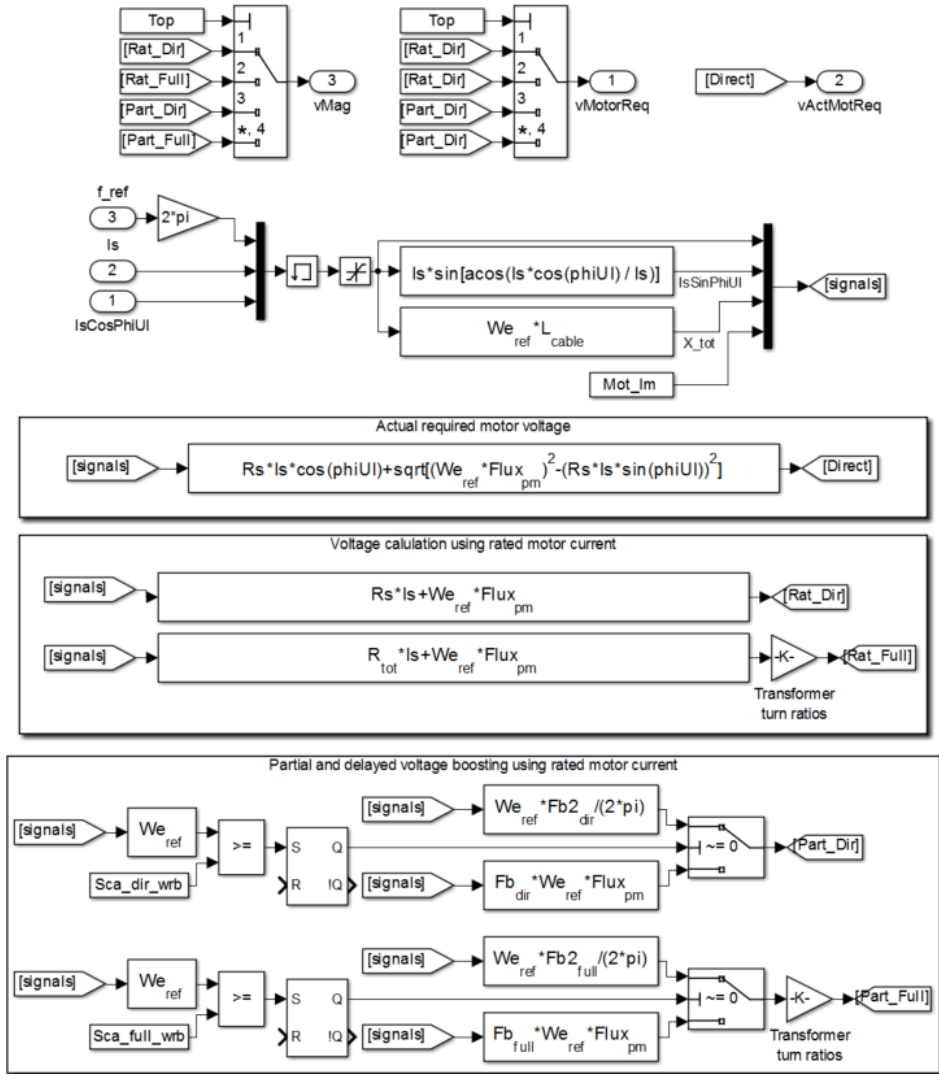


Figure A.12: Inside the voltage requirement calculation block

Controlled voltage source

Using equation (4.3), the Controlled Voltage Source block has been developed in Simulink using Simscape language, as illustrated in Figure A.9. The Simscape codes for the block

are as follows:

```
1 component controlled_voltage
2 % Controlled Voltage Source : 1 : fixed
3 % The block represents an ideal voltage source that is
4   powerful enough
5 % to maintain the specified voltage at its output
6   regardless of the
7 % current passing through it. The output voltage is  $V =$ 
8    $V_{mag}$ , where
9 %  $V_{mag}$  is the numerical value presented at the physical
10  signal port.
11
12 % Kristiansen Baricuatro
13 % 13.03.2014
14
15 inputs
16     vT = { 0, 'V' }; % vMag:left
17     f = { 0, 'Hz' }; % f:left
18 end
19
20 nodes
21     n = pe.electrical.three_phase.electrical; % n:left
22     p = pe.electrical.three_phase.electrical; % ~:right
23 end
24
25 variables
26     V = { [ 0 0 0 ], 'V' };
27     I = {[0 0 0], 'A' };
28     Theta = {0, 'rad' };
29 end
30
31 branches
32     I : p.I -> n.I;
33 end
34
35 equations
36     let
37         w = 2*pi*f;
38     in
39         w == Theta.der;
40
41         V == p.V - n.V;
42         V(1) == vT*cos(Theta);
43         V(2) == vT*cos(Theta-2*pi/3);
44         V(3) == vT*cos(Theta+2*pi/3);
```

41 end
 42 end
 43
 44 end

A.5.2 Closed-loop scalar controller

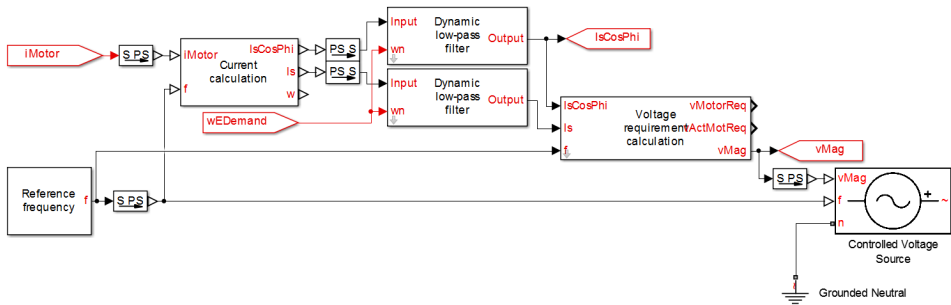


Figure A.13: Closed-loop controller overview

Figure A.13 shows the top-level closed-loop controller Simulink model, showing five user-made subsystems as follows:

- Reference frequency
- Voltage requirement calculation
- Controlled voltage source
- Current calculation
- Dynamic low-pass filter

The reference frequency and controlled voltage source subsystems are the same as the ones used on the open-loop controller. The new subsystems and its blocks are discussed in detail in the following sections.

Voltage requirement calculation

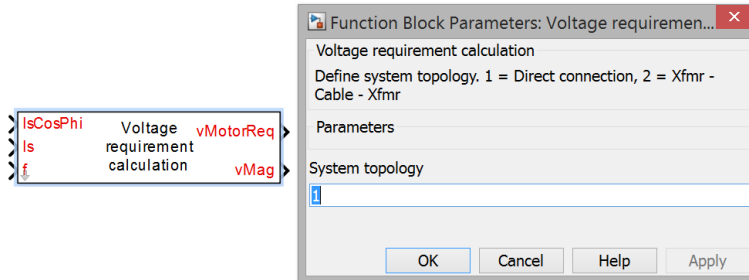


Figure A.14: Voltage requirement calculation block including its mask

The closed-loop scalar control scheme described in chapter 4 have been developed in Simulink within one block. The resulting block including its mask is shown in **Figure A.14**.

Figure A.15 shows what is inside the voltage requirement calculation block.

In order to incorporate the different cases discussed in the thesis, a multiport switch is used. This switch outputs the voltage amplitude calculated via function blocks through a control signal called "Top" which can be defined in the block mask.

All the input signals are fed through a saturation port in order to avoid discontinuities during the zero period. All the required signals and constants are combined into an array named "signals" in order to ease readability of the function blocks.

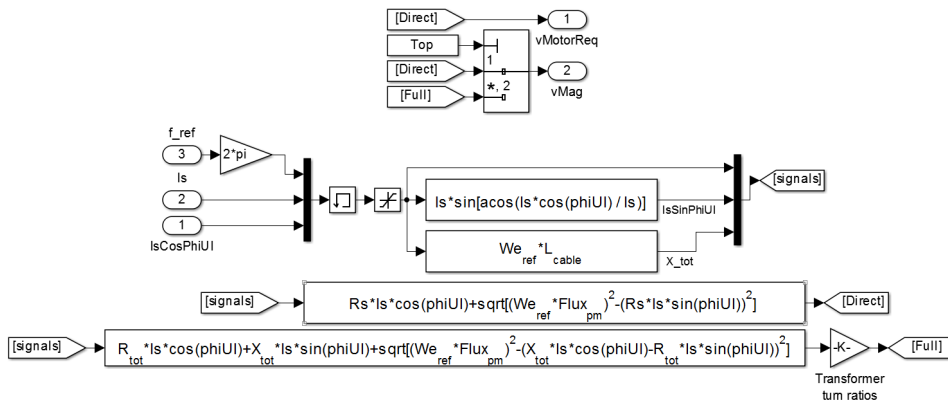


Figure A.15: Inside the voltage requirement calculation block

Current calculation

Using equations (4.12) and (4.13), the Current calculation block has been developed in Simulink using Simscape language, as illustrated in **Figure A.9**. The Simscape codes for the block are as follows:

```
1 component Current_Calculation
2 % Current Calculation
3 % This block calculates the current vector Is and the term
4   Is*cos(phi)
5 % based from phase current input.
6
7 % Kristiansen Baricuatro
8 % 13.04.2014
9
10 inputs
11     iMotor = { [0 0 0], 'A' }; % iMotor:left
12     f = { 0, 'Hz' }; % f:left
13 end
14
15 outputs
16     IsCosPhi = { 0, 'A' }; % IsCosPhi:right
17     Is = { 0, 'A' }; % Is:right
18     w_out = { 0, 'rad/s' }; % w:right
19 end
20
21 variables
22     Theta = {0, 'rad'};
23 end
24
25 equations
26     let
27         w = 2*pi*f;
28         I_alpha = (1/3)*( 2*iMotor(1) - iMotor(2) -
29             iMotor(3) );
30         I_beta = (1/sqrt(3)) * ( iMotor(2) - iMotor(3)
31             );
32     in
33         w == Theta.der;
34         IsCosPhi == (2/3)*( iMotor(1)*cos(Theta) +
35             iMotor(2)*cos(Theta - 2*pi/3) + iMotor(3)*
36             cos(Theta + 2*pi/3) );
37         w_out == w;
38         Is == sqrt( I_alpha^2 + I_beta^2 );
39 end
40 end
```

37

38 **end**

Dynamic low pass filter

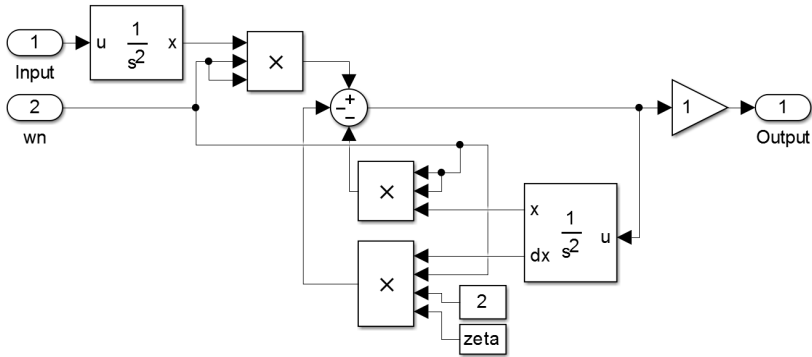


Figure A.16: Inside the Dynamic low pass filter block

Figure A.16 shows the established dynamic low pass filter block which uses equation (4.22).

A.5.3 Closed-loop scalar controller with stabilization loop

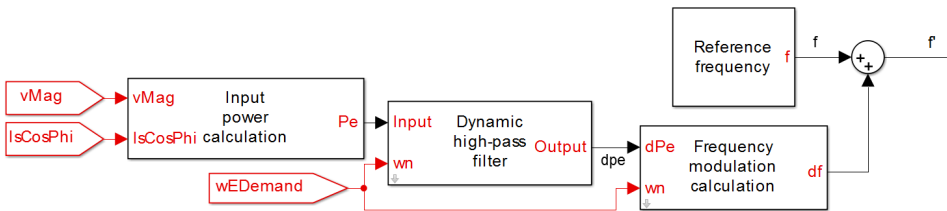


Figure A.17: Overview of the stabilization loop

The stabilization loop for the closed-loop scalar control scheme described in section 4.6 have been developed in Simulink. The resulting overview of the loop is illustrated in **Figure A.17**, showing three user-made subsystems as follows:

- Input power calculation
- Dynamic high-pass filter
- Frequency modulation calculation

These subsystems are discussed in detail in the following sections.

Input power calculation

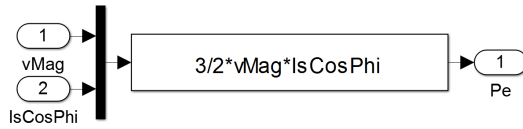


Figure A.18: Inside the Input power calculation block

Figure A.18 shows what is inside the input power calculation block. The input signals are taken from previously made blocks.

Dynamic high pass filter

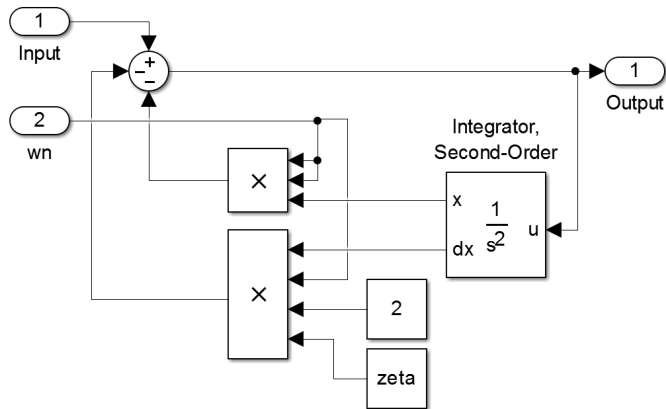


Figure A.19: Inside the Dynamic high pass filter block

Figure A.19 shows the established dynamic high pass filter block which uses equation (4.26).

Frequency modulation calculation

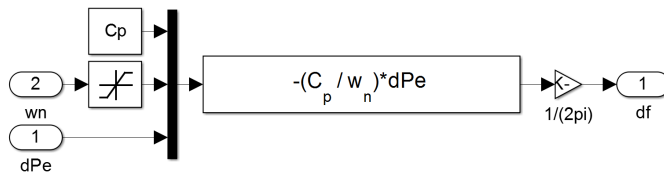


Figure A.20: Inside the Frequency modulation calculation block

Figure A.20 shows the established frequency modulation calculation block which uses equation (4.23). A saturation block is added in order to avoid discontinuities during the zero interval.

A.5.4 Vector controller

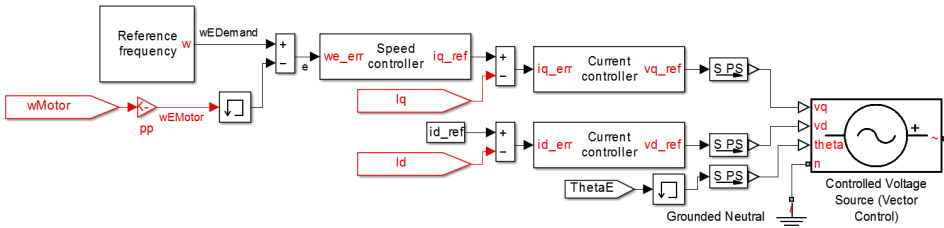


Figure A.21: Vector controller overview

Figure A.21 shows the top-level vector controller Simulink model, showing four user-made subsystems as follows:

- Reference frequency
- Speed controller
- Current controller
- Controlled voltage source

The reference frequency subsystem is the same as the ones used on the scalar controller. The new subsystems and its blocks are discussed in detail in the following sections.

Speed controller

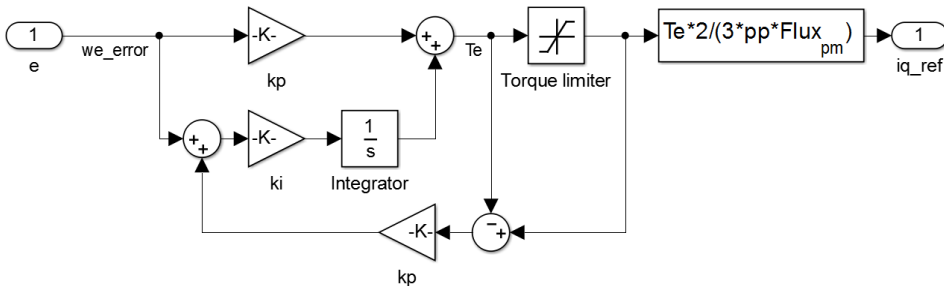


Figure A.22: Inside the Speed controller block

Figure A.22 shows the established dynamic high pass filter block described in section 5.2.2. A torque limiter has been added through a saturation block, which limits the reference torque to the maximum allowable torque of the motor.

Current controller

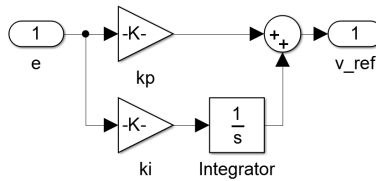


Figure A.23: Inside the Current controller block

Figure A.23 shows the established dynamic high pass filter block described in section 5.2.1.

Controlled voltage source

Using equation (5.33), the Controlled Voltage Source block has been developed in Simulink using Simscape language, as illustrated in **Figure A.21**. The Simscape codes for the block are as follows:

```
1 component controlled_voltage_vec
2 % Controlled Voltage Source (Vector Control) : 1 : fixed
3 % The block represents an ideal voltage source that is
4   powerful enough
5 % to maintain the specified voltage at its output
6   regardless of the
7 % current passing through it. The output voltage is  $V =$ 
8    $V_{mag}$ , where
9 %  $V_{mag}$  is the numerical value presented at the physical
10  signal port.
11
12 % Kristiansen Baricuatro
13 % 13.03.2014
14
15 inputs
16     vq = { 0, 'V' }; % vq:left
17     vd = { 0, 'V' }; % vd:left
18     Theta = { 0, 'rad' }; % theta:left
19 end
20
21 nodes
22     n = pe.electrical.three_phase.electrical; % n:left
23     p = pe.electrical.three_phase.electrical; % ~:right
24 end
25
26 variables
27     V = { [ 0 0 0 ], 'V' };
28     I = {[0 0 0], 'A' };
```

```

25 end
26
27 branches
28     I : p.I -> n.I;
29 end
30
31 equations
32     V == p.V - n.V;
33     V(1) == vq*cos(Theta)+vd*sin(Theta);
34     V(2) == vq*cos(Theta-2*pi/3)+vd*sin(Theta-2*pi/3);
35     V(3) == vq*cos(Theta+2*pi/3)+vd*sin(Theta+2*pi/3);
36 end
37
38 end

```

A.5.5 Vector controller with EKF

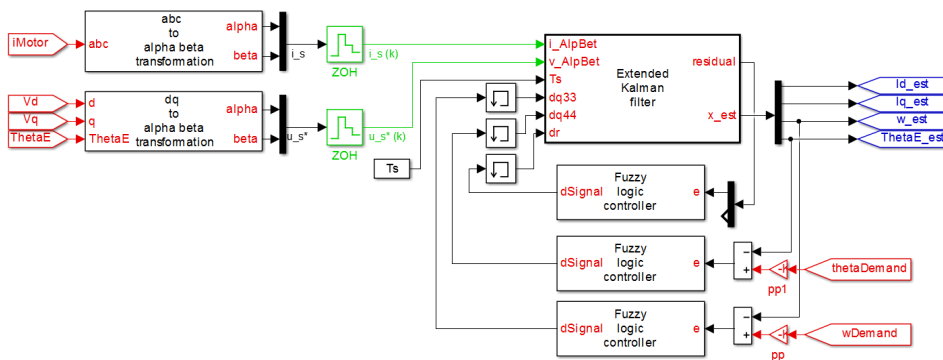


Figure A.24: Overview of the position estimator used on the vector controller

The EKF along with Fuzzy logic control used for position estimation of the vector controller described in section 5.4 have been developed in Simulink. The resulting overview of the position estimator is illustrated in **Figure A.24**, showing three user-made subsystems as follows:

- abc to $\alpha\beta$ transformation
- dq to $\alpha\beta$ transformation
- Extended Kalman filter
- Fuzzy logic controller

These subsystems are discussed in detail in the following sections.

abc to $\alpha\beta$ transformation

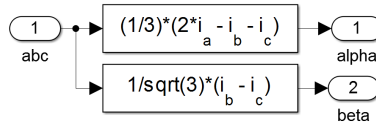


Figure A.25: Inside the abc to $\alpha\beta$ transformation block

Figure A.25 shows the established abc to $\alpha\beta$ transformation block.

dq to $\alpha\beta$ transformation

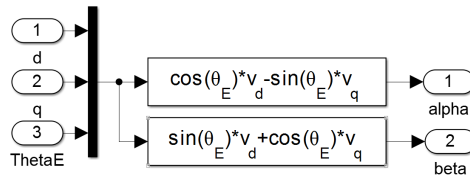


Figure A.26: Inside the dq to $\alpha\beta$ transformation block

Figure A.26 shows the established dq to $\alpha\beta$ transformation block.

Extended Kalman filter

The EKF algorithm described in section 5.4.1 has been developed as a Matlab function block, as illustrated in Figure A.24. The Matlab codes for the block are as follows:

```

1 function [residual , xhatOut] = EXTKALMAN(curr_AlpNet ,
2     volt_AlpNet , deltat , dq3 , dq4 , dr)
3 % Extended Kalman Filter
4 %
5 % This program is executed as a MATLAB function block.
6 %
7 % Kristiansen Baricuatro
8 % 23.05.2014
9 %
10 % Motor Parameters
11 Rs = 53e-3;           %Stator resistance
12 Ld = 1.12e-3;        %d-axis inductance
13 Lq = 1.16e-3;        %q-axis inductance
14 Flux_pm = 0.418;    %Permanent magnet flux [Vs]
15 % Initialization
16 persistent P;

```

```

17 persistent xhat;
18 persistent q3;
19 persistent q4;
20 persistent r;
21 if isempty(P)
22     xhat = [0; 0; 0; 0]; % id, iq, wr, thetar
23     P = diag([1 1 100 10]);
24     q3 = 0;
25     q4 = 0;
26     r = 0;
27 end
28
29 % Covariance matrices
30
31 Q = diag([0.5 0.5 q3 q4]);
32 R = diag([r r]);
33
34 % Prediction (time update)
35
36 A1 = 1-deltat*Rs/Ld;
37 A2 = xhat(3)*deltat*Lq/Ld;
38 A5 = -xhat(3)*deltat*Ld/Lq;
39 A6 = 1-deltat*Rs/Lq;
40 A7 = -deltat*Flux_pm/Lq;
41
42 Ad = [A1 A2 0 0; % G(k+1)
43       A5 A6 A7 0;
44       0 0 1 0;
45       0 0 deltat 1];
46
47 B1 = deltat*cos(xhat(4))/Ld;
48 B2 = deltat*sin(xhat(4))/Ld;
49 B3 = -deltat*sin(xhat(4))/Lq;
50 B4 = deltat*cos(xhat(4))/Lq;
51
52 Bd = [B1 B2;
53       B3 B4;
54       0 0;
55       0 0];
56
57 C = [cos(xhat(4)) -sin(xhat(4)) 0 0; % G(k+1)
58      sin(xhat(4))  cos(xhat(4)) 0 0];
59
60 xhat = Ad*xhat+Bd*volt_AlphaBet;
61 yhat = C*xhat;

```

```

62
63 Ud = volt_AlphaBet(1)*cos(xhat(4))+volt_AlphaBet(2)*sin(xhat(4)
    );
64 Uq = -volt_AlphaBet(1)*sin(xhat(4))+volt_AlphaBet(2)*cos(xhat
    (4));

65
66 F1 = 1-deltat*Rs/Ld;
67 F2 = xhat(3)*deltat*Lq/Ld;
68 F3 = deltat*Lq/Ld*xhat(2);
69 F4 = deltat*Uq/Ld;
70 F5 = -xhat(3)*deltat*Ld/Lq;
71 F6 = 1-deltat*Rs/Lq;
72 F7 = -deltat/Lq*(Ld*xhat(1)+Flux_pm);
73 F8 = deltat*Ud/Lq;

74
75 Phi = [F1 F2 F3 F4; % G(k+1)
76         F5 F6 F7 F8;
77         0 0 1 0;
78         0 0 deltat 1];
79
80 P = Phi*P*Phi' + Q;
81
82 % Compute EKF gain
83
84 M = [ cos(xhat(4)) -sin(xhat(4)) -xhat(1)*sin(xhat(4)) -
      xhat(2)*cos(xhat(4));
85       sin(xhat(4)) cos(xhat(4)) xhat(1)*cos(xhat(4)) -xhat(2)
      *sin(xhat(4)) ];
86
87 W = P*M'*inv(M*P*M'+ R);
88
89 % Innovation (measurement update)
90
91 residual = curr_AlphaBet - yhat;
92
93 xhat = xhat + W*residual;
94
95 P = (eye(4)-W*M)*P*(eye(4)-W*M)' + W*R*W';
96
97 % Output
98
99 xhatOut = xhat;
100
101 % Covariance matrix update
102

```

```

103 q3 = q3 + dq3;
104 q4 = q4 + dq4;
105 r = r + dr;
106
107 q3o = q3;
108 q4o = q4;
109 ro = r;

```

Fuzzy logic controller

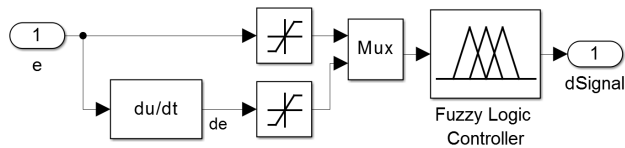


Figure A.27: Inside the Fuzzy logic controller block

Figure A.26 shows the established Fuzzy logic controller block, as described in section 5.4.2. In order to establish the Fuzzy logic rules, the Simulink block called "Fuzzy Logic Controller" has been used.

Matlab simulation script

The Matlab script used to initialize parameters to be used for the simulation are as follows:

```

1  % -----
2  % PMSM
3  % -----
4  % Input data
5  Mot_Rs = 0.165; % Stator winding resistance
6  Mot_Lm1 = 13e-3; % Average single phase magnetizing
   inductance
7  Mot_Lm2 = 0; % Varying magnetizing inductance due to
   saliency
8  Mot_Lls = 6.1e-3; % Leakage inductance
9  Mot_Vll = 7200; % Line voltage
10 Mot_p = 2; % Number of poles
11 Mot_J = 5.7; % Inertia 0.0026
12 Mot_Is = 237; % Rated current
13 Mot_fn = 85; % Synchronous frequency [Hz]
14 Mot_Pn = 2100e3; % Rated power [kW]
15 % -----
16 % Parameter calculations
17 Mot_Lmd = 3/2*(Mot_Lm1+Mot_Lm2); % d-axis magnetizing
   inductance
18 Mot_Lmq = 3/2*(Mot_Lm1-Mot_Lm2); % q-axis magnetizing
   inductance
19 Mot_Ld = Mot_Lls+Mot_Lmd; % d-axis inductance
20 Mot_Lq = Mot_Lls+Mot_Lmq; % q-axis inductance
21 Mot_Vph = Mot_Vll/sqrt(3); % Phase voltage
22 Mot_Vm = Mot_Vph*sqrt(2); % Rated voltage amplitude
23 Mot_Im = Mot_Is * sqrt(2); % Rated current amplitude
24 Mot_pp = Mot_p/2; % Pole pair
25 Mot_nn = 120*Mot_fn/Mot_p; % Synchronous speed
26 Mot_wm = Mot_nn*2*pi/60; % Rated mechanical speed
27 Mot_wr = Mot_pp*Mot_wm; % Rated electrical speed

```

```

28 Mot_PMFlux = (Mot_Vm-Mot_Rs*Mot_Im)/Mot_wr; % Permanent
    magnet flux [Vs]
29 Mot_Tn = Mot_Pn/Mot_wm; % Rated torque
30 Mot_H = Mot_wm*Mot_J/(2*Mot_Tn); % Inertia constant
31
32 % -----
33 % Load
34 % -----
35 % Input data
36 Load_Tbrk = 0.2*Mot_Tn; % Breakaway friction torque
37 Load_ThetaE_start = 0; % Starting position , electrical
38 % -----
39 % Parameter calculations
40 Load_ThetaM_start = Load_ThetaE_start/Mot_pp; % Starting
    position , mech.
41 Load_K = Mot_Tn/(Mot_wm^2); % Load torque constant
42
43 % -----
44 % Transformers
45 % -----
46 % Topside transformer input data
47 T1_n=5.3/24.4; % Turns ratio
48 T1_L1r=4.098107155497063e-04; % Primary winding inductance
    real value
49 T1_L2r=0.008685827967592; % Secondary winding inductance
    real value
50 T1_R1r=0.013764100000000; % Primary winding resistance base
    value
51 T1_R2r=0.291726400000000; % Secondary winding resistance
    base value
52 % Subsea transformer input data
53 T2_n=22/6.9; % Turns ratio
54 T2_L1r=0.010250719211562; % Primary winding inductance real
    value
55 T2_L2r=0.001008340375336; % Secondary winding inductance
    real value
56 T2_R1r=0.242000000000000; % Primary winding resistance base
    value
57 T2_R2r=0.023805000000000; % Secondary winding resistance
    base value
58
59 % -----
60 % Line
61 % -----
62 % Input data

```

```

63 L_r = 0.21; % Resistance [ohm/km]
64 L_l = 0.776; % Inductance [mH/km]
65 L_c = 0.14; % Capacitance [microF/km]
66 L_len = 21.4; % Length [km]
67 % -----
68 % Parameter calculations
69 L_R = L_r*L_len; % Equivalent resistance
70 L_L = L_l*1e-3*L_len; % Equivalent Inductance
71
72 % -----
73 % System parameters and simulation
74 % -----
75 % System parameters
76 Sys_Rtot = Mot_Rs+T2_R2r+(T2_R1r+L_R+T1_R2r)/(T2_n^2)+
    T1_R1r/ ...
77 ((T1_n^2)*(T2_n^2)); % Total equivalent system
    resistance
78 Sys_Ltot = T2_L2r+(T2_L1r+L_L+T1_L2r)/(T2_n^2)+T1_L1r/ ...
79 ((T1_n^2)*(T2_n^2)); % Total equivalent system
    inductance
80 % -----
81 % Frequency ramp and simulation time
82 t_acc = 0.01;% Frequency ramp slope [pu/sec]
83 t_sim = 1/t_acc;
84
85 % -----
86 % Scalar control – Partial and delayed voltage boosting
87 % -----
88 % Input data
89 Sca_Kb = 2; % Back emf to voltage drop ratio
90 % Direct connection parameters
91 Sca_dir_wrb = Sca_Kb*Mot_Rs*Mot_Im/Mot_PMFlux;
92 Sca_dir_fb = Sca_dir_wrb/(2*pi);
93 Sca_dir_Fb = (Mot_Im*Mot_Rs+Sca_dir_wrb*Mot_PMFlux)/(
    Sca_dir_wrb*Mot_PMFlux);
94 Sca_dir_Vmb = Sca_dir_wrb*Sca_dir_Fb*Mot_PMFlux;
95 Sca_dir_Fb2 = (Mot_Im*Mot_Rs+2*pi*Mot_fn*Mot_PMFlux-
    Sca_dir_Vmb)/(Mot_fn-Sca_dir_fb);
96 % Full connection
97 Sca_full_wrb = Sca_Kb*Sys_Rtot*Mot_Im/Mot_PMFlux;
98 Sca_full_fb = Sca_full_wrb/(2*pi);
99 Sca_full_Fb = (Mot_Im*Sys_Rtot+Sca_full_wrb*Mot_PMFlux)/(
    Sca_full_wrb*Mot_PMFlux);
100 Sca_full_Vmb = Sca_full_wrb*Sca_full_Fb*Mot_PMFlux;

```

¹⁰¹
$$\text{Sca_full_Fb2} = (\text{Mot_Im} * \text{Sys_Rtot} + 2 * \text{pi} * \text{Mot_fn} * \text{Mot_PMFlux} - \text{Sca_full_Vmb}) / (\text{Mot_fn} - \text{Sca_full_fb});$$

Attached files

Following are the attached files:

- **Simscape Library** - Contains the user-made Simscape library, which is required to be loaded in order to use the simulation models.
- **Parameters.m** - The Matlab script used to initialize parameters to be used for the simulation.
- **Scalar control schemes** - Contains the simulation files used to test the scalar control schemes. The files are differentiated by the modelled control scheme and the study case.
 - ClosedLoop_NoStabilizer_Base.slx
 - ClosedLoop_NoStabilizer_Test.slx
 - ClosedLoop_Stabilizer_Base.slx
 - ClosedLoop_Stabilizer_Test.slx
 - OpenLoop_Base.slx
 - OpenLoop_Test.slx
- **Vector control scheme** - Contains the simulation files and the fuzzy logic rules used to test the vector control scheme and the EKF. The files are differentiated by the rotor position feedback used by the controller.
 - With_EKF.slx
 - With_EKF_and_FL.slx
 - Without_EKF.slx
 - q3.fis
 - r3.fis